RANS versus LES models

for investigations of the urban climate

Dissertation zur Erlangung des Doktorgrades

an der Fakultät für Mathematik, Informatik und Naturwissenschaften

Fachbereich Geowissenschaften der Universität Hamburg

vorgelegt von

Björn Hendrik Fock

Hamburg

2014

Tag der Disputation: 2015-01-23

Folgende Gutachter empfehlen die Annahme der Dissertation:

Prof. Dr. K. Heinke Schlünzen

Prof. Dr. Bernd Leitl

Academic preface

As this thesis continues work started in Fock (2007), parts of the contents need to overlap. Even though this is pleasant from the scientific point of view, this causes some extra burden in fulfilling good academic practice. To distinguish between achievements of this thesis and the precursor work more references to Fock (2007) are given than necessary from pure scientific requirements. Nevertheless, writing a self-explanatory, alone standing thesis requires some repetitions, especially regarding the theoretical background. Thus, parts on the explanation of the LES technique and parts of the model description may have some similarities with Fock (2007). A model setup, already used in Fock (2007), is used as input for further model experiments here. However, all simulations of idealized free convective boundary layers in Chapter 3 are done with newer and improved model versions.

Chapter 3 – 5 are designed to allow later publication in a scientific journal. Thus some minor repetition may occur in between these and the other chapters. A second consequence is that the literature review and the presentation of model theory is not restricted to the overview given in Chapter 2. Even though the structuring of this text already accounts for later publications, these will likely differ from the following text.

Parts of the technical data handling for the analysis of water temperatures shown in Appendix C have been done by supervising a student assistant (J. Niesel). The preparation of topographic data has been done in cooperation with P. Kirschner, who performed the GIS related work. M. Salim and D.D. Flagg provided the translation (German to English) of the surface class descriptions provided as reference in Appendix D.2. The scientific interpretation of the land use data, i.e. the mapping to physical surface classes, has been shared with the M-SYS community at an early stage. Thus refined interpretations can be found elsewhere.

During working on this thesis co-supervision of the thesis of Ansorge (2009), Philipp (2013) and Schultze (2013) has been performed, who investigated or expanded some of the test cases presented here. Knowledge, data and algorithm has been provided to them to optimize their education. Hence, some overlapping material might be found in their works.

In addition to references to the peer reviewed literature, citations to grey literature have been included wherever this seemed to increase the information content of this thesis. Readers using these additional references should be aware of the different quality control of the cited works. Readers of an electronic version of this text will note that citations equipped with a DOI are directly linked to the related internet addresses, while other citations are linked to their entries in the reference section.

Abstract

This work contributes to the capabilities of turbulence permitting simulations for investigations of the urban climate, by extending and testing the mesoscale model METRAS for large eddy simulations. Model experiments focus on convective boundary layers above homogeneous and heterogeneous surfaces. The heterogeneous surfaces represent an urban area. The performed simulations are used to test METRAS-LES and to investigate topographic impacts on convective boundary layers above the inner-city and harbor area of Hamburg.

A new time integration scheme for the dissipation term in the TKE-equation is presented. A method to control simulations by prescribed heat fluxes is newly implemented into the model. Model intercomparisons between METRAS-LES and the three models METRAS-RANS, METRAS-PCL and PALM contribute to the model testing and demonstrate the difference between RANS and LES solutions. Analyzed sensitivity studies cover the influence of vertical grid stretching, numerical methods and details of the subgrid scale model. Metrics used to discuss model results include spectra, percentile differences and characteristic heights derived from domain averaged variance and covariance profiles. New surface class mappings have been defined for ATKIS and CORINE data, which are used for the simulations above heterogeneous areas. An additional analysis of annual and diurnal cycles of measured water temperatures is provided.

The model experiments show, that free convective boundary layers can be reasonable simulated with METRAS-LES. An effective model resolution of $6 - 8 \Delta x$ could be found for the model results. Grid stretching is acceptable, as long as the area of interest remains well resolved. The stability dependent formulation of the length scale in the used SGS model seems to be of minor importance, compared to other influencing parameters. The TKE parameterization in the surface layer, which is only suitable for flux matching in METRAS-RANS, can be used in METRAS-LES to tune the diffusivity of the model. Simulations with METRAS-LES do not only work for prescribed heat fluxes, but also with the surface energy balance. This allows to study diurnal cycles of convective boundary layers above heterogenic urban surfaces. Simulations of convective boundary layers above Hamburg show a clear response to the water bodies of Elbe and Alster. Experiments with modified topography are used to investigate the influence of orography and surface heterogeneity. The sensitivities on modified topography are relative small for most experiments. The largest impacts, which are even visible by reduced domain averages of 10 m wind speeds and temperatures, are found for redistributing the water areas of Elbe and Alster, randomly within the complete model domain.

Zusammenfassung

Diese Arbeit trägt zu den Möglichkeiten der turbulenzauflösenden Simulation für Stadtklimauntersuchungen bei, indem das mesoskalige Modell METRAS für LES erweitert und getestet wird. Modellversuche wurden für frei konvektive Grenzschichten über homogenen und heterogenen Oberflächen vorgenommen. Die heterogenen Oberflächen stellen ein städtisches Gebiet dar. Die durchgeführten Simulationen dienen dem Modelltest und der Analyse von topographischen Einflüssen auf konvektive Grenzschichten über der Innenstadt und dem Hafen von Hamburg.

Es wird ein neues Zeitintegrationsverfahren für den Dissipationsterm in der TKE-Gleichung vorgestellt. Eine Möglichkeit zum Vorschreiben von Wärmeflüssen wurde implementiert. Vergleiche zwischen Simulationen mit METRAS-LES und mit den drei Modellen METRAS-RANS, METRAS-PCL und PALM wurden durchgeführt, um METRAS-LES zu testen und den Unterschied zwischen RANS- und LES-Ergebnissen aufzuzeigen. In Sensitivitätsstudien wird der Einfluss der Streckung des Vertikalgitters sowie verschiedener numerischer Verfahren und der Details des Subskalenmodells untersucht. Modellergebnisse werden mit Hilfe von Spektren, Perzentildifferenzen und aus gebietsgemittelten Varianz- und Kovarianzprofilen abgeleitete charakteristische Höhen diskutiert. Neue Oberflächenzuordnungen werden für CORINE und ATKIS Daten definiert, welche für die Simulationen über heterogenen Oberflächen verwendet werden. Zusätzlich werden aus gemessenen Wassertemperaturen Jahres- und Tagesgänge analysiert.

Die Modellsimulationen zeigen, dass freie konvektive Grenzschichten sinnvoll mit METRAS-LES simuliert werden können. Es wurden effektive Modellauflösungen von 6 – 8 Δx festgestellt. Vertikale Gitterstreckung liefert akzeptable Ergebnisse, sofern das eigentliche Untersuchungsgebiet hinreichend aufgelöst bleibt. Der Einfluss der stabilitätsabhängigen Formulierung der Längenskala im Subskalenmodell ist im Vergleich zu anderen Einflussfaktoren von untergeordneter Bedeutung. Die TKE-Parametrisierung in der Prandtl-Schicht, welche nur in METRAS-RANS zur Erzwingung von stetigen Flüssen genutzt werden kann, bietet in METRAS-LES Möglichkeit, die Modelldiffusivität einzustellen. Simulationen mit METRAS-LES sind nicht nur mit vorgeschriebenen Wärmeflüssen, sondern auch unter Verwendung der Bodenenergiebilanz möglich. Dadurch können Tagesgänge von konvektiven Grenzschichten über heterogenen Stadtgebieten simuliert werden. Simulationen konvektiver Grenzschichten über Hamburg zeigen eine deutliche Beeinflussung durch die Gewässer Elbe und Alster. Es wurden Experimente mit modifizierter Topographie durchgeführt, um den Einfluss der Orographie und der Oberflächenheterogenität zu untersuchen. In den meisten Experimenten ist der Einfluss der modifizierten Topographie relativ klein. Die größten Einflüsse zeigen sich in Experimenten, welche eine Umverteilung der Wasserflächen vornehmen. Hier werden in gebietsgemittelte Modellergebnisse Reduktionen der Windgeschwindigkeit und Temperatur in 10 m Höhe festgestellt.

Contents

1 Introduction

Urban areas are known to influence the regional and local climate (e.g. Landsberg 1981; Arnfield 2003). Currently 50 % of the world population lives in urban areas (UNFPA 2011, p. 121). Therefore health and living comfort of a large number of people is influenced by urban climate. Considering climatological influences of cities in urban planning can be useful for optimizing local climatological conditions and to mitigate impacts of global warming (Stadt Stuttgart 2010; Berlin Senatsverwaltung für Stadtentwicklung 2011; Schlünzen et al. 2014). Even though progress has been made in the last decades, many challenges remain open in observing, modeling and conceptual understanding of the urban climate as well as in suitable action strategies, to deploy the already available knowledge (Grimmond et al. 2010). One of the main methods to gain inside into the urban climate system is numerical modeling of the atmosphere above urban areas. The use of numerical models allows to investigate urban climate scenarios based on the laws of physics.

The key drivers for the urban climate are – besides the emission of heat and chemical components – the man-made urban surface, and its interaction with the atmosphere. Characteristic surface heterogeneities in urban areas typically have length scales in the order of 1 to 100 m (Section 2.3.2). Therefore grid sizes far below the kilometer scale may be needed to resolve the characteristic atmospheric features triggered by a specific urban area. This demands on resolution raises the question, whether turbulence should be treated as a (partly) resolved or as a (complete) subgrid scale (SGS) process, i.e. if the Reynolds averaged Navier Stokes (RANS) approach is sufficient or if switching to large eddy simulation (LES) might be a more appropriate modeling approach (Section 2.3.1) to investigate the urban atmosphere. In this thesis some steps towards LES based investigation of the urban climate are presented. Conceptual differences and similarities in RANS and LES approaches are discussed in order to provide some judgment on their individual strengths and weaknesses for urban climate modeling.

Regardless whether LES or RANS should be applied, one can roughly classify the models potentially suitable for urban climate investigations at turbulence resolving/permitting scales into three different categories:

- Obstacle resolving microscale models (MiM)[1]

- Conventional atmospheric LES models (CLESM)

- High-resolution mesoscale models (MeM)[1]

---

[1] Naming / abbreviation is adopted from Schlünzen et al. (2011).

The terminus "microscale model" (MiM) is used synonymously for obstacle resolving microscale-γ models here. These models can simulate the flow within the urban obstacle layer and are most often used in an engineering, environmental protection or hazard protection context. Both, RANS and LES methods are used. MiMs can either be designed from a meteorological perspective (e.g. Eichhorn 1989; Schlünzen et al. 2003; Gross 2012) or they can be generic computational fluid dynamics (CFD) codes applied for atmospheric simulations (e.g. Kristóf et al. 2009; Franke et al. 2012). Coupling of MeMs and MiMs – both in LES and in RANS mode – is one of the current challenges recently discussed in the literature (Yamada and Koike 2011; Schlünzen et al. 2011).

Conventional LES models (CLESM) – like those described by Sullivan et al. (1998), Chlond (1998) or Raasch and Schröter (2001) – have been developed to perform controlled numerical experiments in boundary layer and cloud physics research, e.g. to derive parameterizations for turbulent exchange processes. Often CLESMs are used in an idealized setup, with cyclic horizontal boundary conditions, prescribed surface heat fluxes and flat terrain. Some CLESMs have been extended for obstacle resolving simulation (Letzel 2007), while others approach the opposite direction and include features more prominent in mesoscale models, like solving the surface energy balance (Heus et al. 2010).

Mesoscale models are most prominently known for their use in regional modeling for numerical weather prediction and for studies of pollution transport or the regional climate. Operational forecasts with mesoscale models nowadays reach resolutions down to 1 km and below (Golding et al. 2014; Mailhot et al. 2012; Seity et al. 2010). Strictly speaking the term "mesoscale" modeling becomes inaccurate at this grid resolutions as at this scales sub-mesoscale modeling starts, here in the microscale α (Orlanski 1975; Schlünzen et al. 2011). Further grid refinement will bring these models into scales, where large eddy simulation becomes applicable. To allow multi-scale and multi-approach simulations, some mesoscale models have been extended or co-designed for LES applications (Pielke et al. 1992; Cuxart et al. 2000; Golaz et al. 2005; Chow et al. 2006; Moeng et al. 2007). Such models might be helpful for the generation of inlet turbulence for smaller scale LES performed with CFD codes (Hattori et al. 2011). It can be expected that this type of model is the best candidate to provide the missing model bridge to nest from high-resolution mesoscale (RANS) models, over coarse resolution LES to obstacle resolving LES.

This thesis approaches the direction into LES type investigations of the urban climate with the last discussed model type: a mesoscale model heading to smaller scales and switching to the LES approach at the same time. By this model choice it is possible to highlight the additional consequences, which LES implies for urban modeling. Often urban climate modeling is done with mesoscale models treating all turbulence at sub-grid scales, even though the needed resolution of the problem may suggest running models in a partly turbulence resolving LES mode. Thus one aim of this work is to initiate a more conceptual discussion about what modelling approaches should be used in urban climate modeling.

On the one hand this thesis intents to present developments and tests for extending a MeM into the LES regime, on the other hand model applications, data preparation and analysis of simulations aim to contribute to the understanding of the atmosphere above the city of Hamburg. For this city, Schlünzen et al. (2010) derived an annual average urban heat island of 1.1 K from measurement data. Bechtel and Schmidt (2011) characterized the pattern of this heat island with the help of floristic observations. Measurements of soil moisture are performed by Wiesner (2013) to understand the fluxes between the atmosphere and the surface. Lengfeld (2012) investigated the representativity of the climate reference station in Hamburg-Fuhlsbüttel by comparison with measurements of a sensor network. Brümmer et al. (2012) provide diurnal and annual cycles based on long term mast measurements at the eastern outskirts of Hamburg, which include influences of the inner-city and harbor area for westerly winds. Additional background information about the current regional climate can be found in Rosenhagen et al. (2011). Regional climate projections are discussed by Rechid et al. (2014). Hertwig (2013) used wind tunnel data to validate high resolved implicit LES for the inner-city of Hamburg. These simulations have been performed for neutral stratification with the model LES model FAST3D-CT. Funk et al. (2012) present an urban climate assessment, on behalf of the city authorities, using the model FITNAH in RANS mode.

In order to contribute to the above outlined general research topics, this thesis aims to provide answers to the following questions:

- Which model developments and tests are needed to extent the RANS mesoscale model METRAS (Schlünzen et al. 2012a) for LES of convective boundary layers above idealized and realistic surfaces?

- Which model sensitivities can be found and how does the LES model compare to other models, including its RANS version?

- What surface data can be used for the simulation of the diurnal cycle of a convective boundary layer and how important are the details of these data?

- What are the topographic influences on the atmosphere above Hamburg in convective situations?

- What generalizations of the results are possible for LES of convective boundary layers over surfaces with different heterogeneities and for atmospheric modelling performed for urban climate questions?

The used model is introduced in Chapter 2 by providing a general model overview followed by some additional discussion on the concept of large eddy simulation and a review of urban climate applications for Hamburg with that model. Chapter 3 presents necessary adjustments of the model for LES applications and an extended testing of model sensitivity for simulations of convective boundary layers. Chapter 4 provides LES applications to study convective boundary layers over the inner part of the city Hamburg. These applications show in what extend using LES can be relevant for

assessments of the urban climate. Modified simulations of the Hamburg case with varied topographic maps are analyzed in Chapter 5. Chapter 6 provides a concluding discussion, which concentrates the more detailed conclusions given in Chapters 3 to 5. Additional remarks about subgrid modelling, computing technology and data relevant for the urban climate of Hamburg are attached in Appendix A – F.

2   The model METRAS – RANS and LES

This chapter introduces the Multiscale Model System M-SYS (Schlünzen et al. 2012a), consisting of the models METRAS, MITRAS, MECTM, MICTEM and MESIM. M-SYS is extended towards large eddy simulation of convective boundary layers above urban like surfaces heterogeneities in this thesis. Section 2.1 provides an introduction into the model system by reviewing components and application areas of M-SYS. The underlying mathematical, physical and numerical model is shortly described in Section 2.2. Background on large eddy simulation is given in Section 2.3, followed by some motivation for using LES in the context of urban modeling.

2.1   Model overview

2.1.1   Components and deployment areas

The basis of the model system M-SYS is the non-hydrostatic mesoscale model METRAS originally developed by Schlünzen (1988). The model system includes active chemistry transport (Müller et al. 2000; Trukenmüller et al. 2004), the possibility to resolve obstacles in the micro-γ-scale (Schlünzen et al. 2003; Salim et al. 2014), a sea ice model (Birnbaum 1998; Dierer et al. 2005; Gierisch 2014) and a wind turbine module (Linde 2011; Linde et al. 2014). A simplified atmospheric model (Schlünzen and Bigalke 2010) is available for external users and mainly deployed to environmental consulting (e.g. Bigalke et al. 2008).

Model applications include customized weather forecasting for professional sailing teams (Schlünzen et al. 2008) in a region with strong coastal circulations (Fock and Schlünzen 2012), investigations of Arctic albedo changes due to aircraft and ship emissions (Spensberger 2010), ship routing in ice covered waters (Fock 2014, Jochmann et al. 2014), pollen dispersion studies with the aim to provide a tool for risk assessment for transgenic plants (Schueler and Schlünzen 2006; Buschbom et al. 2012) and simulations of ozone chemistry over the North Sea (Meyer and Schlünzen 2011). The one-dimensional submodel, mostly used for initialization purposes, has been applied to check parameterizations applied for dispersion modeling according the German air pollution regulation TA Luft (Boysen 2011). Apart from these more practical applications the model is also used for methodological investigations like model intercomparisons for robustness checks of model results (Chechin et al. 2013), tests of parameterizations to consider subgrid scale land use (Schlünzen and Katzfey 2003) and tests of properties intrinsic to numerical methods (Schroeder et al. 2006; Schroeder and Schlünzen 2009; Schoetter 2010).

2.1.2   Urban applications

Some efforts went into urbanization of the model for investigations of the urban climate: Thompson (2008) added an urban parameterization based on Martilli et al.

(2002) to investigate urban climate of London (Grawe et al. 2013). Petrik et al. (2014) included the emissions of anthropogenic heat into the model. Hoffmann (2012) deployed the model to investigate the impact of climate change on the urban heat island of Hamburg. Schoetter et al. (2013) used a METRAS-RANS setup for Hamburg with a grid resolution of 250 m to investigate the perceived temperature as target variable for climate adaptation measures. Schoetter (2013) used the model to study local climate adaptation measure in terms of perceived temperature and heavy precipitation for the same region. GIS based analysis of METRAS simulations were performed by Teichert (2013) to investigate the influences of urban surfaces in Hamburg. Flagg et al. (2014a) investigated the future urban climate of Hamburg under the assumption that the increase of the global averaged 2 m temperature can be kept below 2 K until the year 2100. All of these urban applications applied the model in the common Reynolds averaged mode.

2.2   Model description

2.2.1   Model dynamics

The model equations of METRAS are derived from Navier-Stokes equation neglecting molecular diffusion and using the anelastic and the Boussinesq approximations. Hence, the time derivative in the continuity equation is neglected and spatial deviations from a reference density are only considered in the buoyancy term of the third equation of motion.

To couple the equation of motion and the mass continuity equation a projection method is used: Each time step the wind field is first integrated into a preliminary state, which is not necessary free of divergence and thus violates the continuity equation. To fulfill the continuity equation, in a second part of an integration step a divergence free wind field is iterated by solving an elliptic equation, which adjust the wind and the pressure field to relate the continuity and the momentum equation (Schlünzen 1988, p. 15 – 16). The integration of temperature and humidity equation follows with the help of the already updated wind field. The time step is finished with cloud physics and diagnostic calculation of density and the final pressure. More details about the process sequence within the model are explained in Schröder (2007a, p. 14 –17) and Schlünzen (1988, p. 26).

The spatial discretization uses a staggered Arakawa C grid (Arakawa 1972, p. 35; Mesinger and Arakawa 1976, p. 45), which allows to calculate the divergence field needed for the elliptic pressure equation with high numerical accuracy directly on the scalar grid (Schlünzen 1988, p. 23). A main advantage of using a staggered grid is the strong coupling between the pressure and the velocity field, which may help to avoid numerical oscillations (e.g. Breuer 2002, p. 155).

The equations are transformed to a terrain following coordinate system (Section 4.1.4) and solved in flux form. Grid stretching is routinely used in the vertical direction but also available in the horizontal directions.

The model variables are decomposed in a constant background state and a deviation part. Prognostic equations are only solved for the deviation parts, while the background parts are constant or diagnostic. The background pressure is assumed to be hydrostatic and geostrophic. Prognostic variables are the wind components u, v, w, and the deviations of potential temperature, absolute humidity, cloud water and rain water from their large-scale reference state. The hydrostatic and non-hydrostatic parts of the pressure deviation are diagnostic variables as well as density and real temperature.

Based on the above stated physical laws and assumptions it is possible to derive the model equations presented in Section 3.1.1. More details about their derivation can be found in Schlünzen et al. (2012a) and Fock (2007).

2.2.2   Model parameterizations

In order to perform physical meaningful simulations with such a model, some subgrid scale processes have to be included as well. These processes are often called "model physics" in atmospheric modeling and deal with processes like turbulent transport, radiation, cloud formation and rain. This section provides a short overview on the parameterizations currently applied in METRAS. A more comprehensive synopsis of available parameterizations is given in Schlünzen et al. (2012a,b).

Different turbulence closures are implemented in the model for Reynolds averaged simulation of mesoscale atmospheric flows. A first implementation of a turbulence closure suitable for LES has been included in METRAS by Fock (2007) and is described in Section 3.1.2, together with an improved numerical treatment of parts of this closure.

The surface layer is represented by the lowest atmospheric model layer, which is by default set to a vertical thickness of 10 m. Monin Obukhov similarity theory (e.g. Krauss 2008, p. 87 – 89; Wyngaard 2010, p. 217 – 225) is employed here. Subgrid scale surface cover variability can be either handled by calculating turbulent surface fluxes from averaged surface parameters or by flux averaging applying the blending height concept (Claussen 1991; von Salzen et al. 1996; Schlünzen and Katzfey 2003; Bohnenstengel 2012). More details on surface layer parameterizations are following in the discussion of the newly implemented option to drive the model by prescribing heat fluxes (Sections 3.1.4), in the presentation of a sensitivity experiment in Section 4.3.2 and in a proof related to the idea of flux matching provided in Appendix B.

Parameterization of cloud microphysics use the Kessler scheme (e.g. Kessler 1995) and include transport equations for cloud water, rain water and water vapor. Transformations between these moisture reservoirs are described by thermodynamic

laws and experimental findings. More details are provided in Schlünzen et al. (2012a, p. 28 – 31), Hoffmann (2009, p. 52 – 56) and Schoetter (2013, p. 63 – 66).

The radiation scheme uses a two-stream approximation to model the long and short wave radiation fluxes for simulations, which employ the optional usable cloud physics described above. This radiation scheme developed by Bakan (1994) has been recently reviewed by Uphoff (2015). Simulations without cloud microphysics (e.g. of dry atmospheres) apply empirical heating and cooling rates in the atmosphere but still allow solving the radiation balance at the surface, depending on the selected options for setting the boundary conditions. The parameterization of radiation includes the influence of geographical position, date, time and possible rotations of the model domain against north. Shading effects caused by orography are taken into account.

2.3 Model concept and aim

2.3.1 Philosophical difference between LES and RANS

Conceptually one can distinguish three main different approaches for the simulation of turbulent flows: Simulations that resolve the full turbulent spectra are called direct numerical simulation (DNS). The opposite, i.e. treating turbulence completely as a sub grid scale process, is known as RANS. An intermediate method between RANS and DNS is LES, where the larger scale turbulent eddies shall be simulated at resolved scales while only small scales are left over for subgrid scale parameterizations. The separation of modelling approaches, by the degree to which the turbulent spectra is resolved, is illustrated schematically in Figure 2-1 and Figure 2-2.
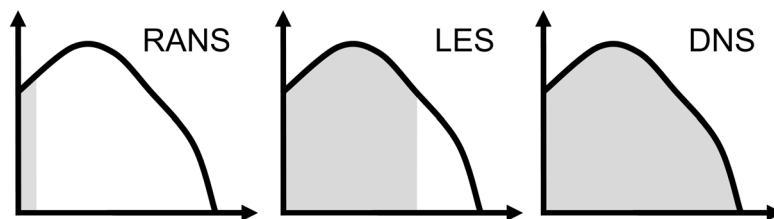
Figure 2-1: Conceptual drawing of simulated (gray) and modeled (white) turbulence spectra for the three main simulation techniques Reynolds averaged Navier-Stokes simulation, large eddy simulation and direct numerical simulation.
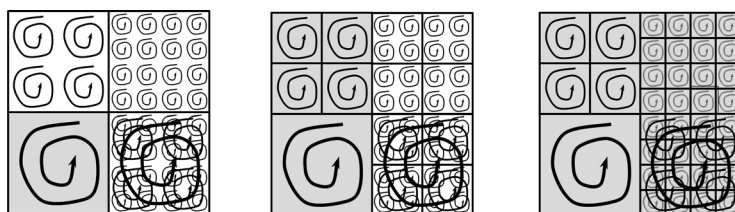

Figure 2-2: Conceptual drawing of simulated (gray) vs. modeled (white) eddies for the simulation techniques RANS, LES and DNS (left to right). Each drawn grid cell represents a number of grid cells needed for discretely resolving one eddy.

To increase the fraction of resolved turbulence, finer model resolutions are needed. This limits the feasible domain sizes due to computational costs. Both RANS and LES can be seen as trick to make simulations of larger parts of the atmosphere possible with available computer resources. The mathematic technique is a filtering operation, which is employed to the governing equations.

To achieve scale separation and derive the LES equations the prognostic variables are decomposed in a resolved and an unresolved part. For that some sort of filtering is applied to the equations, which removes the unresolved part. To describe the filtering of the equations, basically two different approaches exist:

- The "filtering approach", introduced by Leonard (1974), uses "explicit filtering" (Fröhlich 2006, p. 108 – 127) of the (approximated) Navier Stokes equations prior their discretization. The discretization is than applied to the filtered equations and aims to represent the filtered fields completely. This spatial filtering does not fulfill the Reynolds averaging axioms. Therefore formal differences in the resulting SGS stress terms arise.

- The "volume-balance approach", introduced by Schumann (1975), combines "implicit filtering" (Fröhlich 2006, p. 127 – 129) with the discretization of the equations. The filtering done with this approach is basically the average over the volume of a grid box, which is very similar to the filtering for RANS models, which does the same but additionally includes time averaging (Pielke 2013, p. 42ff.). Besides the meaning of the averaging operator there is no formal difference in the resulting SGS fluxes terms arising from RANS and implicit LES filtering. The missing time averaging and smaller filtering length scales, i.e. smaller grid box volumes, allow the implicitly filtered equations to include parts of the turbulence spectra at the resolved scales.

Independent of the followed filtering approach, the filtered equations have (nearly) the same principle structure regardless whether an LES filter or Reynolds averaging is applied. The differences are in the scale (and structure for the filtering approach) of the subgrid scale exchange terms and in the physical meaning of the simulated flow field. While in RANS the filtered flow describes an ensemble average, for LES this is only a spatial average, which allows some resolved turbulence. For practical simulations this means that different parameterizations for subgrid scale exchanges are needed. Even though the idea of filtering is central for the concept of LES, it should be noted that it is agreed in literature (e.g. Chlond 1988, p. 22 – 23) that the actual properties of the filtering operation can be determined only a posteriori, i.e. after simulations have been performed. Grid volume averaged (implicitly filtered) model equations for METRAS-LES are given in Section 3.1.1. The same grid volume averaging has been used for spatial filtering of the equations of METRAS-RANS (Schlünzen et al. 2012a, p. 7), but the additional applied time filtering to reach an ensemble average in METRAS-RANS is diminished in METRAS-LES to allow simulating turbulent fluctuations. The principle idea is to reduce the time filter of the model, so that the grid box filtered fields are valid instantaneously, i.e. all time changes, which could occur in a

"grid box averaged" atmosphere, should be directly resolved by the LES model. This should be achieved by a SGS model (Section 3.1.2) different from the RANS turbulence closure and an adequate model resolution. Further discussion of the filtering process can be found in Heinze (2013, p. 17), Chlond (1998, p. 18 – 23), Letzel (2007, p. 8 – 10) and Fock (2007, p. 27 – 31).

The theoretical concept of LES builds, as briefly explained above, on the idea of simulating large parts of the turbulent spectra on resolved scales. Thus the choice of the "right" LES closure to model the subgrid scale part of atmospheric turbulence might be of minor importance in a well resolved LES model (Raasch 2010). Some LES models do not use an explicit subgrid scale model at all, but handle subgrid scale diffusion by numerical diffusion alone (Boris 1992). Nevertheless most models include some SGS closure. As for RANS there is quite a large variety of possible SGS closures for LES: The simplest widely used closure is probably the Smagorinsky (1963) model, which assumes local equilibrium of dissipation and energy production and thus only depends on the local shear. More detailed SGS models try to consider more details of the flow structure by including additional transport equations for sub grid scale turbulent kinetic energy (TKE) (Lilly 1966; Deardorff 1980) and its dissipation. Other methods apply test filter to adjust model constants dynamically to the simulated flow fields (Germano et al. 1991; Porté-Agel et al. 2000). Further details about the theoretical background of LES can be found in a more extensive literature review provided by Hertwig (2013).

2.3.2   Aim and potential use of the LES version of METRAS

Up to now all urban model application with the Multiscale Model System M-SYS applied Reynolds averaging (Section 2.1.2). The question if LES should be applied to urban climate problems arises naturally from the comparison of the length scales found in surface heterogeneities of urban areas and grid resolutions commonly applied in CLESM (Chapter 1).

As an example maps (classified in 10 surface classes, Section 5.1) of the inner part of the city of Hamburg are provided with various raster resolutions in Figure 2-3. It is obvious from the maps that a 250 m grid raster (Figure 2-3 (a)) is rather insufficient to resolve the characteristic spatial features of this urban surface. Grid sizes of 100 m or below (Figure 2-3 (b) – (d)) are needed to in order to reproduce the main morphologic features on the map of this city. Hence, urban climate models, for cities like Hamburg, need grid resolutions in the order of a few decameters to resolve occurring surface types (e.g. parking areas, parks, etc.) at grid scale. With such a model it is still not possible to resolve individual obstacles (e.g. buildings) but at least the map scale used in urban development plans can be reached, which seems to be an obvious requirement for a model, which shall be usable for local climate studies in the context of urban planning.

As at this scale LES can be performed, one may wish to use that to overcome possible errors, which may arise from the use of RANS turbulence closures, which may not be

valid for this scale. Furthermore, extending the modeling approach conceptually towards LES is needed for problems, which require information about the fluctuations of the atmospheric variables in addition to their mean values. This is most probably the case for exceedance of extreme values, which can be filtered out in Reynolds averaged models.

(a)   (b)   (c)   (d)
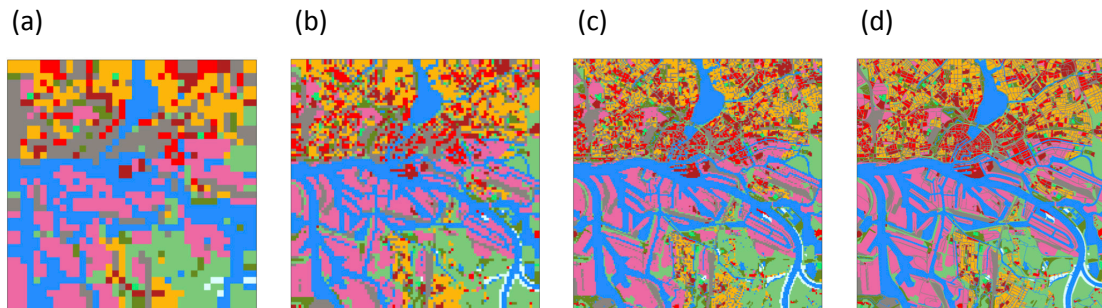

Figure 2-3: Main surface classes in the inner city of Hamburg classified in 10 classes (Section 5.1). The raster resolution increases from 250 m (a) via 100 m (b) and 50 m (c) to 12.5 m (d). A legend and a map scale are provided in Figure 5-1.

3 Validation and sensitivity of LES model results

This chapter investigates how the <u>me</u>soscale <u>tr</u>ansport and <u>s</u>tream <u>m</u>odel METRAS (Schlünzen 1988) can be used as LES model for idealized simulation of convective boundary layers using prescribed heat fluxes. The simulated case describes the development of a convective boundary layer, using a test case also used by Fock (2007). Needed additions and corrections to a preliminary version of METRAS-LES (Fock 2007) are presented, followed by model validation and sensitivity studies.

A general overview on the model equations is given in Section 3.1.1. The implemented subgrid scale model is described in Section 3.1.2. A fully implicit method for the time discretization of the dissipation used by the subgrid scale model is explained in Section 3.1.3. To allow model intercomparison of idealized simulations the calculation of the surface boundary values is completely revised in the model, which is described in Section 3.1.4. Section 3.2 provides a basic model validation experiment, a model intercomparison with the LES model PALM and an investigation of the effective model resolution. Sensitivities of the model results on the SGS model, on the used advection scheme and on the vertical grid are analyzed in Section 3.3. Additionally, characteristic heights used for the interpretation of the model results in Chapter 4 are introduced here.

3.1 METRAS-LES

3.1.1 Model equations

With the model assumptions shortly reviewed in Section 2.1 the following prognostic model equations can be derived (Schlünzen et al. 2012a):

$$
\begin{aligned}
\frac{\partial \overline{u}}{\partial t} = & -\frac{1}{\rho_0 \alpha^*}\frac{\partial}{\partial \dot{x}^1}\left(\overline{u}\,\frac{\partial \dot{x}^1}{\partial x}\rho_0 \alpha^* \overline{u}\right) - \frac{1}{\rho_0 \alpha^*}\frac{\partial}{\partial \dot{x}^2}\left(\overline{v}\,\frac{\partial \dot{x}^2}{\partial y}\rho_0 \alpha^* \overline{u}\right) \\
& -\frac{1}{\rho_0 \alpha^*}\frac{\partial}{\partial \dot{x}^3}\left(\left(\overline{u}\,\frac{\partial \dot{x}^3}{\partial x}+\overline{v}\,\frac{\partial \dot{x}^3}{\partial y}+\overline{w}\,\frac{\partial \dot{x}^3}{\partial z}\right)\rho_o \alpha^* \overline{u}\right) \\
& -\frac{1}{\rho_0}\frac{\partial \dot{x}^1}{\partial x}\left(\frac{\partial p_1}{\partial \dot{x}^1}+\frac{\partial p_2}{\partial \dot{x}^1}\right) - \frac{1}{\rho_0}\frac{\partial \dot{x}^3}{\partial x}\frac{\partial p_2}{\partial \dot{x}^3} + g\,\frac{\tilde{\rho}}{\rho_0}\frac{\partial \dot{x}^3}{\partial x}\frac{\partial z}{\partial \dot{x}^3} \\
& +2\Omega\sin(\varphi)\left(\overline{v}-V_g\right)-2\Omega\cos(\varphi)\overline{w}-F_1
\end{aligned}
\tag{3.1}
$$

$$
\begin{aligned}
\frac{\partial \overline{v}}{\partial t} = & -\frac{1}{\rho_0 \alpha^*}\frac{\partial}{\partial \dot{x}^1}\left(\overline{u}\,\frac{\partial \dot{x}^1}{\partial x}\rho_0 a^* \overline{v}\right) - \frac{1}{\rho_0 \alpha^*}\frac{\partial}{\partial \dot{x}^2}\left(\overline{v}\,\frac{\partial \dot{x}^2}{\partial y}\rho_0 \alpha^* \overline{v}\right) \\
& -\frac{1}{\rho_0 \alpha^*}\frac{\partial}{\partial \dot{x}^3}\left(\left(\overline{u}\,\frac{\partial \dot{x}^3}{\partial x}+\overline{v}\,\frac{\partial \dot{x}^3}{\partial y}+\overline{w}\,\frac{\partial \dot{x}^3}{\partial z}\right)\rho_o \alpha^* \overline{v}\right) \\
& -\frac{1}{\rho_0}\frac{\partial \dot{x}^2}{\partial y}\left(\frac{\partial p_1}{\partial \dot{x}^2}+\frac{\partial p_2}{\partial \dot{x}^2}\right) - \frac{1}{\rho_0}\frac{\partial \dot{x}^3}{\partial y}\frac{\partial p_2}{\partial \dot{x}^3} + g\,\frac{\tilde{\rho}}{\rho_0}\frac{\partial \dot{x}^3}{\partial y}\frac{\partial z}{\partial \dot{x}^3} \\
& -2\Omega\sin(\varphi)\left(\overline{u}-U_g\right)-F_2
\end{aligned}
\tag{3.2}
$$

$$\frac{\partial \overline{w}}{\partial t} = -\frac{1}{\rho_0 \alpha^*} \frac{\partial}{\partial \dot{x}^1}\left(\overline{u}\frac{\partial \dot{x}^1}{\partial x}\rho_0 \alpha^* \overline{w}\right) - \frac{1}{\rho_0 \alpha^*}\frac{\partial}{\partial \dot{x}^2}\left(\overline{v}\frac{\partial \dot{x}^2}{\partial y}\rho_0 \alpha^* \overline{w}\right)$$

$$-\frac{1}{\rho_0 \alpha^*}\frac{\partial}{\partial \dot{x}^3}\left(\left(\overline{u}\frac{\partial \dot{x}^3}{\partial x} + \overline{v}\frac{\partial \dot{x}^3}{\partial y} + \overline{w}\frac{\partial \dot{x}^3}{\partial z}\right)\rho_o \alpha^* \overline{w}\right) \tag{3.3}$$

$$-\frac{1}{\rho_0}\frac{\partial \dot{x}^3}{\partial z}\frac{\partial p_2}{\partial \dot{x}^3} - 2\Omega\cos(\varphi)\overline{u} - F_3$$

$$\frac{\partial \overline{\chi}}{\partial t} = -\frac{1}{\rho_0 \alpha^*}\frac{\partial}{\partial \dot{x}^1}\left(\overline{u}\frac{\partial \dot{x}^1}{\partial x}\rho_0 \alpha^* \overline{\chi}\right) - \frac{1}{\rho_0 \alpha^*}\frac{\partial}{\partial \dot{x}^2}\left(\overline{v}\frac{\partial \dot{x}^2}{\partial y}\rho_0 \alpha^* \overline{\chi}\right)$$

$$-\frac{1}{\rho_0 \alpha^*}\frac{\partial}{\partial \dot{x}^3}\left(\left(\overline{u}\frac{\partial \dot{x}^3}{\partial x} + \overline{v}\frac{\partial \dot{x}^3}{\partial y} + \overline{w}\frac{\partial \dot{x}^3}{\partial z}\right)\rho_0 \alpha^* \overline{\chi}\right) - F_\chi + Q_\chi \tag{3.4}$$

The model equations are given here in the used terrain following ($\dot{x}^1, \dot{y}^2, \dot{z}^3$) coordinates (Section 4.1.4) after been transferred from the Cartesian system (x, y, z). The background density ρ_0 and the grid transformation constant α^* are not time dependent. Therefore they have been moved out of the time derivative and brought on the right hand side of Equation (3.1) – (3.4), in agreement with the model implementation. The overbars symbolize a spatial LES filter. $\overline{\chi}$ serves as generic substitute for scalar variables like potential temperature $\overline{\theta}$, specific humidity $\overline{q}_v$, cloud water $\overline{q}_c$, rain water $\overline{q}_r$ and the subgrid scale turbulent kinetic energy $\overline{e}$. Q_χ represents sources and sinks. Further symbols are explained in the list of symbols on page 116ff. Terms needed for rotation of the model domain are not used in this theses and left out here for simplicity. They are described in Spensberger (2010).

The main difference between METRAS-LES and METRAS-RANS is in the divergences of the SGS fluxes F_1, F_2, F_3 and F_χ. These flux divergences occur in the equations due to filtering (Section 2.3.1) of the equations and the non-linearity of the advection term. They can formally be written as

$$F_1 = \frac{1}{\rho_0 \alpha^*}\frac{\partial}{\partial \dot{x}^1}\left(\rho_o \alpha^*\left(\overline{uu} - \overline{u}\,\overline{u}\right)\frac{\partial \dot{x}^1}{\partial x}\right) + \frac{1}{\rho_0 \alpha^*}\frac{\partial}{\partial \dot{x}^2}\left(\rho_o \alpha^*\left(\overline{uv} - \overline{u}\,\overline{v}\right)\frac{\partial \dot{x}^2}{\partial y}\right)$$

$$+\frac{1}{\rho_0 \alpha^*}\frac{\partial}{\partial \dot{x}^3}\left(\rho_0 \alpha^*\left(\left(\overline{uu} - \overline{u}\,\overline{u}\right)\frac{\partial \dot{x}^3}{\partial x} + \left(\overline{uv} - \overline{u}\,\overline{v}\right)\frac{\partial \dot{x}^3}{\partial y} + \left(\overline{uw} - \overline{u}\,\overline{w}\right)\frac{\partial \dot{x}^3}{\partial z}\right)\right) \tag{3.5}$$

$$F_2 = \frac{1}{\rho_0 \alpha^*}\frac{\partial}{\partial \dot{x}^1}\left(\rho_o \alpha^*\left(\overline{uv} - \overline{u}\,\overline{v}\right)\frac{\partial \dot{x}^1}{\partial x}\right) + \frac{1}{\rho_0 \alpha^*}\frac{\partial}{\partial \dot{x}^2}\left(\rho_o \alpha^*\left(\overline{vv} - \overline{v}\,\overline{v}\right)\frac{\partial \dot{x}^2}{\partial y}\right)$$

$$+\frac{1}{\rho_0 \alpha^*}\frac{\partial}{\partial \dot{x}^3}\left(\rho_0 \alpha^*\left(\left(\overline{uv} - \overline{u}\,\overline{v}\right)\frac{\partial \dot{x}^3}{\partial x} + \left(\overline{vv} - \overline{v}\,\overline{v}\right)\frac{\partial \dot{x}^3}{\partial y} + \left(\overline{vw} - \overline{v}\,\overline{w}\right)\frac{\partial \dot{x}^3}{\partial z}\right)\right) \tag{3.6}$$

$$F_3 = \frac{1}{\rho_0 \alpha^*}\frac{\partial}{\partial \dot{x}^1}\left(\rho_o \alpha^*\left(\overline{uw} - \overline{u}\,\overline{w}\right)\frac{\partial \dot{x}^1}{\partial x}\right) + \frac{1}{\rho_0 \alpha^*}\frac{\partial}{\partial \dot{x}^2}\left(\rho_o \alpha^*\left(\overline{vw} - \overline{v}\,\overline{w}\right)\frac{\partial \dot{x}^2}{\partial y}\right)$$

$$+\frac{1}{\rho_0 \alpha^*}\frac{\partial}{\partial \dot{x}^3}\left(\rho_0 \alpha^*\left(\left(\overline{uw} - \overline{u}\,\overline{w}\right)\frac{\partial \dot{x}^3}{\partial x} + \left(\overline{vw} - \overline{v}\,\overline{w}\right)\frac{\partial \dot{x}^3}{\partial y} + \left(\overline{ww} - \overline{w}\,\overline{w}\right)\frac{\partial \dot{x}^3}{\partial z}\right)\right) \tag{3.7}$$

$$F_\chi = \frac{1}{\rho_0 \alpha^*} \frac{\partial}{\partial \dot{x}^1} \left(\rho_o \alpha^* \left(\overline{u\chi} - \overline{u}\,\overline{\chi} \right) \frac{\partial \dot{x}^1}{\partial x} \right) + \frac{1}{\rho_0 \alpha^*} \frac{\partial}{\partial \dot{x}^2} \left(\rho_o \alpha^* \left(\overline{v\chi} - \overline{v}\,\overline{\chi} \right) \frac{\partial \dot{x}^2}{\partial y} \right)$$

$$+ \frac{1}{\rho_0 \alpha^*} \frac{\partial}{\partial \dot{x}^3} \left(\rho_o \alpha^* \left(\left(\overline{u\chi} - \overline{u}\,\overline{\chi} \right) \frac{\partial \dot{x}^3}{\partial x} + \left(\overline{v\chi} - \overline{v}\,\overline{\chi} \right) \frac{\partial \dot{x}^3}{\partial y} + \left(\overline{w\chi} - \overline{w}\,\overline{\chi} \right) \frac{\partial \dot{x}^3}{\partial z} \right) \right) \quad (3.8)$$

The terms $\overline{uu}$, $\overline{uv}$, $\overline{uw}$, $\overline{uv}$, $\overline{vv}$, $\overline{vw}$, $\overline{ww}$, $\overline{u\chi}$, $\overline{v\chi}$ and $\overline{w\chi}$ are unknown and need to be expressed by a parameterization. The SGS turbulence parameterization used in METRAS_LES to express Equation (3.5) – (3.8) is provided in Section 3.1.2.

Some diagnostic equations like the elliptic equation for the pressure deviation p_2, the hydrostatic equation for the pressure deviation p_1, the equation of state and parameterizations for non-turbulent subgrid scale processes complete the model. These details can be found in Schlünzen et al. (2012).

3.1.2 Parameterization of subgrid scale turbulence

Different filtering is applied in METRAS-LES compared to METRAS-RANS (Section 2.3.1). The parameterization used to describe for SGS fluxes in METRAS-LES needs to account for less SGS exchange than the turbulence model used in METRAS-RANS. The divergences of the subgrid scale fluxes F_χ, F_1, F_2 and F_3 have a similar form as in METRAS-RANS (Schlünzen 1988, p. 17 – 18, 21 – 22 and 110).

They are expressed by a gradient approach and are formulated as:

$$F_\chi = -\frac{1}{\rho_0 \alpha^*} \frac{\partial}{\partial \dot{x}^1} \left(\rho_o \alpha^* K_{\chi,hor} \left(\frac{\partial \overline{\chi}}{\partial \dot{x}^1} \frac{\partial \dot{x}^1}{\partial x} + \frac{\partial \overline{\chi}}{\partial \dot{x}^3} \frac{\partial \dot{x}^3}{\partial x} \right) \frac{\partial \dot{x}^1}{\partial x} \right)$$

$$-\frac{1}{\rho_0 \alpha^*} \frac{\partial}{\partial \dot{x}^2} \left(\rho_o \alpha^* K_{\chi,hor} \left(\frac{\partial \overline{\chi}}{\partial \dot{x}^2} \frac{\partial \dot{x}^2}{\partial y} + \frac{\partial \overline{\chi}}{\partial \dot{x}^3} \frac{\partial \dot{x}^3}{\partial y} \right) \frac{\partial \dot{x}^2}{\partial y} \right)$$

$$-\frac{1}{\rho_0 \alpha^*} \frac{\partial}{\partial \dot{x}^3} \left(\rho_o \alpha^* K_{\chi,ver} \left(\frac{\partial \overline{\chi}}{\partial \dot{x}^1} \frac{\partial \dot{x}^1}{\partial x} + \frac{\partial \overline{\chi}}{\partial \dot{x}^3} \frac{\partial \dot{x}^3}{\partial x} \right) \frac{\partial \dot{x}^3}{\partial x} \right) \quad (3.9)$$

$$-\frac{1}{\rho_0 \alpha^*} \frac{\partial}{\partial \dot{x}^3} \left(\rho_o \alpha^* K_{\chi,ver} \left(\frac{\partial \overline{\chi}}{\partial \dot{x}^2} \frac{\partial \dot{x}^2}{\partial y} + \frac{\partial \overline{\chi}}{\partial \dot{x}^3} \frac{\partial \dot{x}^3}{\partial y} \right) \frac{\partial \dot{x}^3}{\partial y} \right)$$

$$-\frac{1}{\rho_0 \alpha^*} \frac{\partial}{\partial \dot{x}^3} \left(\rho_o \alpha^* K_{\chi,ver} \left(\frac{\partial \overline{\chi}}{\partial \dot{x}^3} \frac{\partial \dot{x}^3}{\partial z} \right) \frac{\partial \dot{x}^3}{\partial z} \right)$$

$$
\begin{aligned}
F_1 = &-\frac{1}{\rho_0 \alpha^*}\frac{\partial}{\partial \dot{x}^1}\left(\rho_o \alpha^* 2K_{hor}\left(\frac{\partial \dot{x}^1}{\partial x}\frac{\partial \overline{u}}{\partial \dot{x}^1}+\frac{\partial \dot{x}^3}{\partial x}\frac{\partial \overline{u}}{\partial \dot{x}^3}\right)\frac{\partial \dot{x}^1}{\partial x}\right)\\
&-\frac{1}{\rho_0 \alpha^*}\frac{\partial}{\partial \dot{x}^2}\left(\rho_o \alpha^* K_{hor}\left(\frac{\partial \dot{x}^2}{\partial y}\frac{\partial \overline{u}}{\partial \dot{x}^2}+\frac{\partial \dot{x}^3}{\partial y}\frac{\partial \overline{u}}{\partial \dot{x}^3}+\frac{\partial \dot{x}^1}{\partial x}\frac{\partial \overline{v}}{\partial \dot{x}^1}+\frac{\partial \dot{x}^3}{\partial x}\frac{\partial \overline{v}}{\partial \dot{x}^3}\right)\frac{\partial \dot{x}^2}{\partial y}\right)\\
&-\frac{1}{\rho_0 \alpha^*}\frac{\partial}{\partial \dot{x}^3}\left(\rho_0 \alpha^* 2K_{hor}\left(\frac{\partial \dot{x}^1}{\partial x}\frac{\partial \overline{u}}{\partial \dot{x}^1}+\frac{\partial \dot{x}^3}{\partial x}\frac{\partial \overline{u}}{\partial \dot{x}^3}\right)\frac{\partial \dot{x}^3}{\partial x}\right)\\
&-\frac{1}{\rho_0 \alpha^*}\frac{\partial}{\partial \dot{x}^3}\left(\rho_0 \alpha^* K_{hor}\left(\frac{\partial \dot{x}^2}{\partial y}\frac{\partial \overline{u}}{\partial \dot{x}^2}+\frac{\partial \dot{x}^3}{\partial y}\frac{\partial \overline{u}}{\partial \dot{x}^3}+\frac{\partial \dot{x}^1}{\partial x}\frac{\partial \overline{v}}{\partial \dot{x}^1}+\frac{\partial \dot{x}^3}{\partial x}\frac{\partial \overline{v}}{\partial \dot{x}^3}\right)\frac{\partial \dot{x}^3}{\partial y}\right)\\
&-\frac{1}{\rho_0 \alpha^*}\frac{\partial}{\partial \dot{x}^3}\left(\rho_0 \alpha^* K_{ver}\left(\frac{\partial \dot{x}^3}{\partial z}\frac{\partial \overline{u}}{\partial \dot{x}^3}+\frac{\partial \dot{x}^1}{\partial x}\frac{\partial \overline{w}}{\partial \dot{x}^1}+\frac{\partial \dot{x}^3}{\partial x}\frac{\partial \overline{w}}{\partial \dot{x}^3}\right)\frac{\partial \dot{x}^3}{\partial z}\right)
\end{aligned}
\tag{3.10}
$$

$$
\begin{aligned}
F_2 = &-\frac{1}{\rho_0 \alpha^*}\frac{\partial}{\partial \dot{x}^1}\left(\rho_o \alpha^* K_{hor}\left(\frac{\partial \dot{x}^2}{\partial y}\frac{\partial \overline{u}}{\partial \dot{x}^2}+\frac{\partial \dot{x}^3}{\partial y}\frac{\partial \overline{u}}{\partial \dot{x}^3}+\frac{\partial \dot{x}^1}{\partial x}\frac{\partial \overline{v}}{\partial \dot{x}^1}+\frac{\partial \dot{x}^3}{\partial x}\frac{\partial \overline{v}}{\partial \dot{x}^3}\right)\frac{\partial \dot{x}^1}{\partial x}\right)\\
&-\frac{1}{\rho_0 \alpha^*}\frac{\partial}{\partial \dot{x}^2}\left(\rho_o \alpha^* 2K_{hor}\left(\frac{\partial \dot{x}^2}{\partial y}\frac{\partial \overline{v}}{\partial \dot{x}^2}+\frac{\partial \dot{x}^3}{\partial y}\frac{\partial \overline{v}}{\partial \dot{x}^3}\right)\frac{\partial \dot{x}^2}{\partial y}\right)\\
&-\frac{1}{\rho_0 \alpha^*}\frac{\partial}{\partial \dot{x}^3}\left(\rho_0 \alpha^* K_{hor}\left(\frac{\partial \dot{x}^2}{\partial y}\frac{\partial \overline{u}}{\partial \dot{x}^2}+\frac{\partial \dot{x}^3}{\partial y}\frac{\partial \overline{u}}{\partial \dot{x}^3}+\frac{\partial \dot{x}^1}{\partial x}\frac{\partial \overline{v}}{\partial \dot{x}^1}+\frac{\partial \dot{x}^3}{\partial x}\frac{\partial \overline{v}}{\partial \dot{x}^3}\right)\frac{\partial \dot{x}^3}{\partial x}\right)\\
&-\frac{1}{\rho_0 \alpha^*}\frac{\partial}{\partial \dot{x}^3}\left(\rho_0 \alpha^* 2K_{hor}\left(\frac{\partial \dot{x}^2}{\partial y}\frac{\partial \overline{v}}{\partial \dot{x}^2}+\frac{\partial \dot{x}^3}{\partial y}\frac{\partial \overline{v}}{\partial \dot{x}^3}\right)\frac{\partial \dot{x}^3}{\partial y}\right)\\
&-\frac{1}{\rho_0 \alpha^*}\frac{\partial}{\partial \dot{x}^3}\left(\rho_0 \alpha^* K_{ver}\left(\frac{\partial \dot{x}^3}{\partial z}\frac{\partial \overline{v}}{\partial \dot{x}^3}+\frac{\partial \dot{x}^2}{\partial y}\frac{\partial \overline{w}}{\partial \dot{x}^2}+\frac{\partial \dot{x}^3}{\partial y}\frac{\partial \overline{w}}{\partial \dot{x}^3}\right)\frac{\partial \dot{x}^3}{\partial z}\right)
\end{aligned}
\tag{3.11}
$$

$$
\begin{aligned}
F_3 = &-\frac{1}{\rho_0 \alpha^*}\frac{\partial}{\partial \dot{x}^1}\left(\rho_o \alpha^* K_{ver}\left(\frac{\partial \dot{x}^3}{\partial z}\frac{\partial \overline{u}}{\partial \dot{x}^3}+\frac{\partial \dot{x}^1}{\partial x}\frac{\partial \overline{w}}{\partial \dot{x}^1}+\frac{\partial \dot{x}^3}{\partial x}\frac{\partial \overline{w}}{\partial \dot{x}^3}\right)\frac{\partial \dot{x}^1}{\partial x}\right)\\
&-\frac{1}{\rho_0 \alpha^*}\frac{\partial}{\partial \dot{x}^2}\left(\rho_o \alpha^* K_{ver}\left(\frac{\partial \dot{x}^3}{\partial z}\frac{\partial \overline{v}}{\partial \dot{x}^3}+\frac{\partial \dot{x}^2}{\partial y}\frac{\partial \overline{w}}{\partial \dot{x}^2}+\frac{\partial \dot{x}^3}{\partial y}\frac{\partial \overline{w}}{\partial \dot{x}^3}\right)\frac{\partial \dot{x}^2}{\partial y}\right)\\
&-\frac{1}{\rho_0 \alpha^*}\frac{\partial}{\partial \dot{x}^3}\left(\rho_0 \alpha^* K_{ver}\left(\frac{\partial \dot{x}^3}{\partial z}\frac{\partial \overline{u}}{\partial \dot{x}^3}+\frac{\partial \dot{x}^1}{\partial x}\frac{\partial \overline{w}}{\partial \dot{x}^1}+\frac{\partial \dot{x}^3}{\partial x}\frac{\partial \overline{w}}{\partial \dot{x}^3}\right)\frac{\partial \dot{x}^3}{\partial x}\right)\\
&-\frac{1}{\rho_0 \alpha^*}\frac{\partial}{\partial \dot{x}^3}\left(\rho_0 \alpha^* K_{ver}\left(\frac{\partial \dot{x}^3}{\partial z}\frac{\partial \overline{v}}{\partial \dot{x}^3}+\frac{\partial \dot{x}^2}{\partial y}\frac{\partial \overline{w}}{\partial \dot{x}^2}+\frac{\partial \dot{x}^3}{\partial y}\frac{\partial \overline{w}}{\partial \dot{x}^3}\right)\frac{\partial \dot{x}^3}{\partial y}\right)\\
&-\frac{1}{\rho_0 \alpha^*}\frac{\partial}{\partial \dot{x}^3}\left(\rho_0 \alpha^* 2K_{ver}\left(\frac{\partial \dot{x}^3}{\partial y}\frac{\partial \overline{w}}{\partial \dot{x}^3}\right)\frac{\partial \dot{x}^3}{\partial z}\right)
\end{aligned}
\tag{3.12}
$$

To provide a full reference horizontal and vertical diffusion is distinguished in Equation (3.9) – (3.12) and in the following. However, the same diffusion coefficients are used in METRAS-LES for horizontal and vertical diffusion, i.e. isotropic SGS turbulence is assumed. K_{vert} and K_{hor} ($K_{\chi,vert}$ and $K_{\chi,hor}$) are separately treated in the discretization, because the implementation of the diffusion operator is shared between METRAS-LES and METRAS-RANS. Currently the distinction in horizontal and vertical diffusion is only used in METRAS-RANS. For anisotropic grids it might be useful to

reconsider this distinction also in METRAS-LES. Nevertheless, simulations performed with METRAS-LES so far have shown neither evidence that this would be needed nor that this would be harmful.

METRAS was originally developed for Reynolds averaged mesoscale model applications. The implemented closure from Deardorff (1980) is a SGS model often used in atmospheric LES codes. Based on a literature review (Fock 2007, p. 32 – 36) some coefficients used in the implemented SGS model vary slightly from the values suggested by Deardorff (1980). The SGS model is based on a prognostic equation for SGS turbulent kinetic energy and applies a characteristic grid size as mixing length. The implementation in METRAS-LES has been done based on an existing closure for METRAS-RANS, which also applies an equation for the (total) turbulent kinetic energy (Schmittner 1996, p. 15–21/62–70 ; Fock 2007, p. 26–27). The exchange coefficients in the LES closure are defined as

$$K = K_{ver} = K_{hor} = c_k l \cdot \overline{e}^{1/2} \tag{3.13}$$

$$K_\chi = K_{\chi,ver} = K_{\chi,hor} = \left(1 + \frac{2l}{\Delta}\right) \cdot K \tag{3.14}$$

The proportionality constant c_k in Equation (3.13) is assumed as $c_k = 0.1$. The characteristic length scale of the grid filter Δ is calculated from

$$\Delta = (\Delta x \cdot \Delta y \cdot \Delta x)^{1/3} \tag{3.15}$$

The length scale for the largest unresolved atmospheric turbulent motion l depends on the grid length scale Δ and includes an additional stability correction, which reduces the exchange coefficients for stable stratifications:

$$l = \min\left(\Delta, \frac{0.76 \cdot \overline{e}^{1/2}}{N_{BV}}\right) \qquad \text{if} \quad N_{BV}^2 > 0 \qquad \text{(stable)} \tag{3.16}$$

$$l = \Delta \qquad \text{if} \quad N_{BV}^2 \leq 0 \qquad \text{(unstable)} \tag{3.17}$$

The used stability measure in Equations (3.16) – (3.17) is the square of the Brunt-Väisälä frequency N_{BV} (e.g. Stull 2000, p. 135 – 136; Roedel 2000, p. 81 – 83) defined as

$$N_{BV}^2 = \frac{g}{\overline{\theta}_v} \cdot \frac{\partial \dot{x}^3}{\partial z} \frac{\partial \overline{\theta}_v}{\partial \dot{x}^3} \quad \cdot \tag{3.18}$$

$\overline{\theta}_v = \overline{\theta} \cdot (1 + (R_v/R - 1) \cdot \overline{q})$ is the virtual potential temperature. For the subgrid scale turbulent kinetic energy $\overline{e}$ the transport equation (3.4) is solved using the following source and sink term:

$$Q_{\overline{e}} = \text{MECH}(\overline{u}, \overline{v}, \overline{w}) + \text{BOU}(\overline{\theta}) + \text{BOU}(\overline{q}) + \text{DISS}(\overline{e}) \tag{3.19}$$

The pressure correlation terms are neglected in the TKE equation. The advection and diffusion are treated as the other scalar variables. Mechanical production of $\overline{e}$ is calculated by

$$
\begin{aligned}
\mathrm{MECH}(\overline{u},\overline{v},\overline{w}) = {} &+2K_{hor}\left(\frac{\partial \dot{x}^1}{\partial x}\frac{\partial \overline{u}}{\partial \dot{x}^1} + \frac{\partial \dot{x}^3}{\partial x}\frac{\partial \overline{u}}{\partial \dot{x}^3}\right)^2 \\
&+ K_{hor}\left(\frac{\partial \dot{x}^2}{\partial y}\frac{\partial \overline{u}}{\partial \dot{x}^2} + \frac{\partial \dot{x}^1}{\partial x}\frac{\partial \overline{v}}{\partial \dot{x}^1} + \frac{\partial \dot{x}^3}{\partial y}\frac{\partial \overline{u}}{\partial \dot{x}^3} + \frac{\partial \dot{x}^3}{\partial x}\frac{\partial \overline{v}}{\partial \dot{x}^3}\right)^2 \\
&+ K_{ver}\left(\frac{\partial \dot{x}^3}{\partial z}\frac{\partial \overline{u}}{\partial \dot{x}^3} + \frac{\partial \dot{x}^1}{\partial x}\frac{\partial \overline{w}}{\partial \dot{x}^1} + \frac{\partial \dot{x}^3}{\partial x}\frac{\partial \overline{w}}{\partial \dot{x}^3}\right)^2 \\
&+ K_{ver}\left(\frac{\partial \dot{x}^3}{\partial z}\frac{\partial \overline{v}}{\partial \dot{x}^3} + \frac{\partial \dot{x}^2}{\partial y}\frac{\partial \overline{w}}{\partial \dot{x}^2} + \frac{\partial \dot{x}^3}{\partial y}\frac{\partial \overline{w}}{\partial \dot{x}^3}\right)^2 \\
&+ 2K_{hor}\left(\frac{\partial \dot{x}^2}{\partial y}\frac{\partial \overline{v}}{\partial \dot{x}^2} + \frac{\partial \dot{x}^3}{\partial y}\frac{\partial \overline{v}}{\partial \dot{x}^2}\right)^2 \\
&+ 2K_{ver}\left(\frac{\partial \dot{x}^3}{\partial z}\frac{\partial \overline{w}}{\partial \dot{x}^3}\right)^2
\end{aligned}
\tag{3.20}
$$

Buoyancy can act as source or sink term for $\overline{e}$ and is calculated based on gradients of potential temperature

$$
\mathrm{BOU}(\overline{\theta}) = -\frac{g}{\theta_0}K_{\chi,vert}\left(\frac{\partial \dot{x}^3}{\partial z}\frac{\partial \overline{\theta}}{\partial \dot{x}^3}\right)
\tag{3.21}
$$

and on gradients of specific humidity

$$
\mathrm{BOU}(\overline{q}) = -g\cdot\left(\frac{R_v}{R}-1\right)\cdot K_{\chi,vert}\left(\frac{\partial \dot{x}^3}{\partial z}\frac{\partial \overline{q}}{\partial \dot{x}^3}\right)
\tag{3.22}
$$

The dissipation term depends on the dissipation rate ε and is parameterized as

$$
\mathrm{DISS}(\overline{e}) = -\varepsilon = -c_\varepsilon \frac{\overline{e}^{3/2}}{l}
\tag{3.23}
$$

In Equation (3.23) c_ε is assumed as

$$
c_\varepsilon = 0.19 + 0.74 l / \Delta
\tag{3.24}
$$

3.1.3   Time splitting for the dissipation term

The use of Equation (3.23) in Equation (3.19) results in a dissipation term in Equation (3.4) that is implicit in the subgrid scale turbulent kinetic energy $\overline{e}$. The equation for the turbulent kinetic energy $\overline{e}$ is explicitly integrated forward in time in the RANS version of the model. This approach has shown problems in the LES version of the SGS TKE equation, as the dissipation term tends to be too large, so that it produces negative values for the SGS TKE. Hence, a numerical method for integration of this

equation is presented here, which prohibits unphysical negative values of $\overline{e}$, which otherwise occur due to too strong dissipation.

The principal idea of the method is to split the prognostic equation for the subgrid scale turbulent kinetic energy in two parts:

$$\frac{\partial \overline{e}}{\partial t} = \sum (\text{all procecces excepted dissipation}) - \varepsilon \tag{3.25}$$

In the first part all processes excluding the dissipation are integrated within a time step Δt. This calculation provides a preliminary value for the turbulent kinetic energy $\hat{\overline{e}}^{n+1}$ ($\hat{}$ denotes a preliminary value)[2]. This value is then used in a second part of the time step integration in the dissipation term:

$$\frac{\partial \hat{\overline{e}}^{n+1}}{\partial t} = -f(\hat{\overline{e}}^{n+1}) \tag{3.26}$$

The assumed functional dependency of the dissipation from the SGS turbulent kinetic energy is expressed as $\varepsilon = f(\hat{\overline{e}}^{n+1})$. For the SGS model described in Section 3.1.2 an analytical solution for $\hat{\overline{e}}^{n+1}$ was derived from Equation (3.26) and implemented in the numerical model. This approach should be applicable to any turbulent kinetic energy based closures, as long as the function f allows an analytical solution of Equation (3.26). Appendix A.2 shows how this method is ported to the obstacle resolving microscale (RANS) model MITRAS, which applies a dissipation parameterization ε different from the one used in METRAS-LES.

To apply this solution method to the LES closure, Equation (3.23) is used as dissipation function f in Equation (3.26), which gives

$$\frac{\partial \hat{\overline{e}}^{n+1}}{\partial t} = -\frac{c_\varepsilon \cdot \left(\hat{\overline{e}}^{n+1}\right)^{3/2}}{l} \quad . \tag{3.27}$$

The length scale l (Equation (3.16) – (3.17)), and therefore also $c_\varepsilon(l)$ (Equation (3.24)), can depend on the subgrid scale turbulent kinetic energy due to the formulation of the length scale l as a function of the atmospheric stability. Hence, an additional dependency on $\hat{\overline{e}}^{n+1}$ is included in c_ε and l on the right hand side of Equation (3.27). Therefore a case distinction, with two different solutions is required.

Grid length scale:

>   For unstable stratification the dependency simplifies due to $l = \Delta$ and $c_\varepsilon = 0.93 = const$. In this case the analytic solution of Equation (3.27) is given by

---

[2] Notation has been chosen in consistency with Schröder (2007a).

$$e^{n+1} = \hat{\bar{e}}^{n+1} \frac{1}{1 + \dfrac{c_\varepsilon \Delta t \sqrt{\hat{\bar{e}}^{n+1}}}{l} + \dfrac{c_\varepsilon^2 \Delta t^2 \hat{\bar{e}}^{n+1}}{4l^2}} \tag{3.28}$$

The derivation of Equation (3.28) is provided in Appendix A.1.1.

Atmospheric length scale:

If the Deardorff correction term $l = 0.76 \cdot e^{1/2} / N_{BV}$ applies for stable stratification, additional dependencies of $\hat{\bar{e}}^{n+1}$ are following in Equation (3.27) caused by $l = f(\hat{\bar{e}}^{n+1})$ and $c_\varepsilon = f(\hat{\bar{e}}^{n+1})$. Thus the analytical solution is more complicated:

$$\bar{e}^{n+1} = \frac{N_{BV}^2}{16} \cdot \left(\exp\left(\ln \frac{\frac{N_{BV}}{4} + \frac{0.74}{\Delta}\sqrt{\hat{\bar{e}}^{n+1}}}{\sqrt{\hat{\bar{e}}^{n+1}}} + \Delta t \frac{N_{BV}}{8} \right) - \frac{0.74}{\Delta} \right)^{-2} \tag{3.29}$$

The derivation of (3.29) is provided in Appendix A.1.2.

Please note that the case distinction in Equation (3.16) – (3.17) is not strictly according to atmospheric stability because $l = \Delta$ is possible for both stable and unstable conditions. Equation (3.28) also applies not only for unstable conditions, but also for stable conditions, if $\Delta \leq 0.76 \cdot \bar{e}^{1/2}/N_{BV}$. Hence, the length scales have been named "grid" and "atmospheric" above rather than "unstable" and "stable".

This new implicit method for the time integration of dissipation term in the TKE equation solves the numerical problems with negative $\bar{e}$ due to too much dissipation within one time step if solved forward in time.

3.1.4   Prescribing of surface heat flux

Most CLESMs prescribe fixed heat fluxes at the surface. The model METRAS calculates these fluxes based on Monin Obukhov scaling (Monin and Obukhov 1954), previously either from prescribed surfaces temperatures or from surface temperatures resulting from the solution of the surface energy balance equation. Hence the values for the heat fluxes used for the lower boundary condition of the prognostic equation for potential temperature has been calculated internally and could not be set by the model user explicitly.

To allow direct model intercomparisons with CLESMs, an erroneous, only partially successful, method for prescribing heat fluxes at the surface in METRAS-LES has been tried by Fock (2007, p. 44 – 45). This allowed some first simulations of free convective boundary layers (CBL) with METRAS-LES, but showed problems with a strong decoupling of the temperature at the interface between the first two atmospheric model levels. Inconsistencies in the first model level lead to severe instabilities, which prohibited extending the simulation time of these partly successful simulations. Thus for further work with METRAS-LES a more reliable method was needed.

The corrected method, described below, solves this problem and allows continuing surface heating over longer periods. Thus it consolidates the abilities of METRAS-LES to use prescribed heat fluxes for simulations of CBL and is a prerequisite for new validation (Section 3.2) and sensitivity (Section 3.3) experiments. The corrected method has also been included in the model version provided for the work of Phillipp (2013).

The new implementation allows prescribing heat fluxes individually for each grid cell. Additionally a possible time dependence of the prescribed heat flux has been implemented. The heat flux can either be prescribed as kinematic heat flux ($H / \rho c_p$ [K m s^{-1}]) or as dynamic heat flux (H [W m^{-2}]).

Internally the desired heat flux is not prescribed directly, to allow an undisruptive implementation close to the standard surface layer scheme. Hence, the iterative calculation of surface layer scaling variables u_* and θ_* is modified. The heat flux applied to the lower atmospheric grid cell is calculated from the scaling variables as:

$$\frac{H}{\rho c_p} = -u_* \theta_* \tag{3.30}$$

Initially (at each time step), θ_* is adjusted according to Equation (3.30) to force the desired heat flux using the friction velocity u_* of the previous time step. In case the option to prescribe the dynamic heat flux is selected, the desired flux is transformed to a kinematic flux by normalization according (3.30).

In the following iteration the Obukhov length[3] is calculated according

$$L = \frac{\theta u_*^2}{g\kappa \left(\theta_* + \left(\frac{R_v}{R} - 1 \right) \theta q_* \right)} \tag{3.31}$$

The physical constants κ, R and R_v are given in the list of symbols on page 116ff. The calculation of the scaling parameter q_* for the humidity flux is described in Schlünzen et al. (2012a, p. 20). The friction velocity is calculated according

$$u_* = \kappa \frac{u_p}{\ln(z_p / z_0) - \psi(z_p / L)} \tag{3.32}$$

To consider thermal stability the same stability functions ψ and ψ_χ are used in Equations (3.32), (3.38) and (3.39) as in the RANS version of the model METRAS:

For unstable/neutral stratification, i.e. for z/L ≤ 0:

---

[3] According AMS (2000) this length scale should not be called "Monin-Obukhov length", as often done, because it can be found first in the work of Obukhov.

$$\psi = 2\ln\left((1+\phi^{-1})/2\right) + 2\ln\left((1+\phi^{-2})/2\right) - 2\arctan\left(\phi^{-2}\right) + \frac{\pi}{2} \qquad (3.33)$$

$$\psi_\chi = 2\ln\left(\frac{1+\phi_\chi}{2}\right) \qquad (3.34)$$

For stable stratification, i.e. for $z/L > 0$:

$$\psi = \psi_\chi = -5\frac{z}{L} \qquad (3.35)$$

The used ϕ-functions are taken according to Dyer (1974) as

$$\phi = \phi_\chi^{1/2} = \left(1 - 16\cdot\frac{z}{L}\right)^{-1/4} \qquad \text{if } \frac{z}{L} \le 0 \qquad (3.36)$$

$$\phi = \phi_\chi = 1 + 5\frac{z}{L} \qquad \text{if } \frac{z}{L} > 0 \qquad (3.37)$$

The actual prescribing of the flux employs the calculation of an auxiliary temperature at the surface

$$\theta_{SFC} = \theta_p - \theta_* \frac{\ln(z_p/z_0) - \psi_\chi(z_p/L)}{\kappa} \qquad (3.38)$$

which accounts for the initially prescribed θ_*. Hence, θ_{SFC} is the potential temperature at the surface, which produces the desired flux by recalculating θ_* for the next iteration by

$$\theta_* = \kappa \frac{\theta_{SFC} - \theta_p}{\ln(z_p/z_0) - \psi_\chi(z/L)} \qquad (3.39)$$

In the second iteration L, u_*, θ_{SFC} and θ_* are recalculated according Equations (3.31) – (3.39). Thus the adjusted scaling temperature and the auxiliary surface temperature are used to add the possibility to prescribe heat fluxes to the surface flux scheme of METRAS.

3.2 Model validation

A test case describing the development of a convective boundary layer originally designed by Fedorovich and Conzemius (2002) is used in the following. The same setup has also been used in Fock (2007) and for simulations analyzed by Ansorge (2009). This allows to discuss the new results together with older findings.

The basic model setup is described in Section 3.2.1 followed by a short introduction into the physical processes, which are simulated in this model test. An

intercomparison with another LES model is presented in Section 3.2.3. Variations of the test setup are used for sensitivity studies, following in Section 3.3.

3.2.1   Specification of reference simulation

The simulated atmosphere is initially at rest, horizontal homogeneous and of stable thermal stratification. The initial potential temperature gradient is set to a constant lapse rate $\partial\theta/\partial z = 0.003\,\mathrm{K\,m^{-1}}$. The initial potential temperature specified at the surface is 295.15 K. A hydrostatic balanced pressure and density profile is set using a surface pressure of 1013.15 hPa. A complete dry atmosphere is assumed to simplify the interpretation of the experiment. The latitude is chosen as $\varphi = 40°\,\mathrm{N}$, which determines the used Coriolis parameters. The roughness length z_0 is set to 0.01 m. The model grid consists of $128 \times 128 \times 104$ cells, with a uniform grid spacing of $\Delta x = \Delta y = \Delta z = 20$ m. Hence, the total model domain spans 2560 m in the horizontal and 2080 m in the vertical direction.

The atmosphere is heated by a constant kinematic heat flux of $0.1\,\mathrm{K\,ms^{-1}}$ prescribed at the surface with the method described in Section 3.1.4. This iterative procedure produces a heat flux interacting with the flow pattern. Hence, it is not exactly at the prescribed value at each grid cell. Nevertheless the area averaged flux is much more precise than 1 % compared to the prescribed value for the most part of the integration period (Figure 3-1). Only during the initialization, i.e. at the onset time of convection, the prescribed kinematic heat flux is overestimated up to 10 % for a short time period. Averaged over 3 hours of integration time the resulting flux is 2 ‰ above the intended value, hence the newly implemented control for the supply of surface heat fluxes is sufficiently precise.
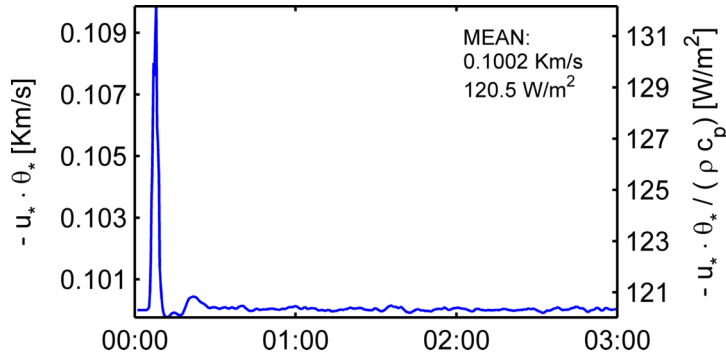

Figure 3-1: Area averaged surface heat flux with prescribed target value of $0.1\,\mathrm{K\,m\,s^{-1}}$.

The calculated scaling temperature θ_* is perturbed by white noise at all grid cells during the first time step. The amplitude of the imposed random fluctuation is uniformly distributed between ± 10 % of the unperturbed value of θ_*. This disturbance is sufficient to initialize convection without imposing further perturbations.

3.2.2   Physical description of reference simulation

The above specified model setup results in the simulation of a developing free convective boundary layer (CBL). To provide some first insight into the physics of the simulated situation, vertical cross sections of potential temperature deviation are given in Figure 3-2 for selected time slices. Potential temperature deviations rather than potential temperatures are shown; because including the stable stratified background field θ_0 would somehow obscure the visible physical processes due to the increase of θ_0 with height. Corresponding snapshots of horizontal cross sections of potential temperature deviations are shown in Figure 3-3.

The heat supply at the lower surface results in a warming of the lower model levels, which is more or less spatially homogeneous during the first five minutes (Figure 3-2 (a), Figure 3-3 (a)). A convective flow system has not been established after 5 min but started clearly before 10 min of surface heating as it is visible from Figure 3-2 (a) and (b). This goes together with the maximum in the surface layer heat flux, which peaks after 8 min of heat supply (Figure 3-1) indicating an abrupt onset of convection. Figure 3-2 (c) – (f) show regions with negative temperature deviations at the top of the heated boundary layer, which is due to entrainment of colder air from above. In the horizontal cross sections (Figure 3-3) cellular structures are visible, which extend in diameter horizontally with growing CBL depth. After 10 min (Figure 3-3 (b)) lower potential temperatures are observed in the inner part of the convective cells than in the more homogeneous temperature field after 5 min (Figure 3-3 (a)). These lower temperatures are caused by sinking of cooler air in the inner parts of the cells. The supplied heat is transported upward by rising motion connected with the cell walls.
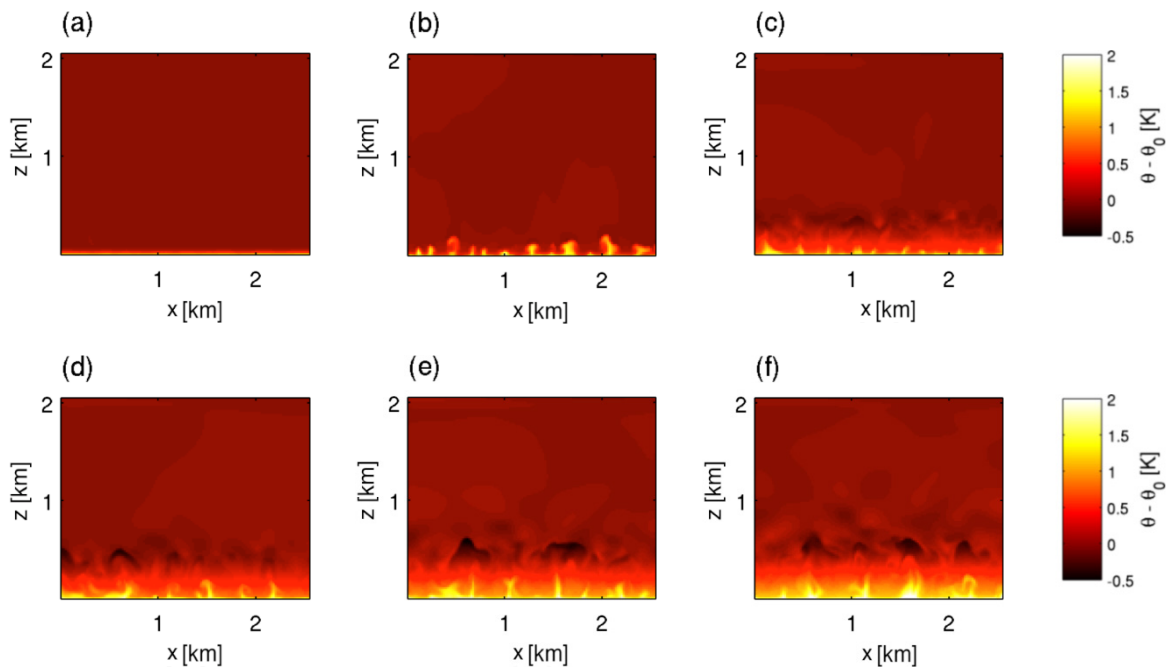

Figure 3-2: Vertical cross sections of potential temperature deviation in the middle part of the domain (1100 m from the southern border) after (a) 5 min, (b) 10 min, (c) 20 min, (d) 30 min, (e) 40 min and (f) 50 min integration time.
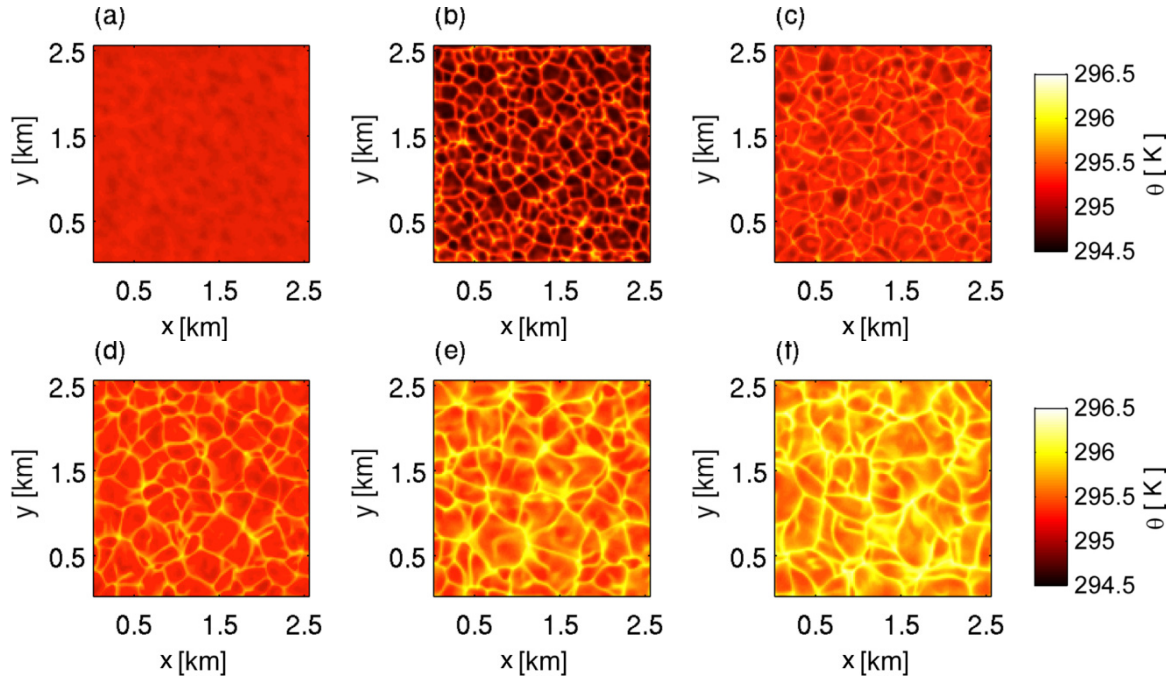
Figure 3-3: Horizontal cross sections of potential temperature at 10 m height after (a) 5 min,(b) 10 min,(c) 20 min,(d) 30 min,(e) 40 min and (f) 50 min integration time.

In contrast to the simulations from Fock (2007) the temperatures in the lowest atmospheric model level are consistent with the temperatures above due to the improved prescription of the heat flux at the surface (Section 3.1.4), which also improves the numerical stability of the model and enables longer simulations. Model fields above the first model level show similar results than the simulations from Fock (2007). Thus the above given introduction to the simulated case can be completed by considering cross sections of the vertical wind speed provided by Fock (2007, p. 46 – 47). Further details of the underlying physics are discussed below in combination with validation and sensitivity studies. A lexical review on convective boundary layers can be found in LeMone (2003).

3.2.3   Model intercomparison between METRAS-LES and PALM

A comparison of profiles from METRAS-LES and the results from Fedorovich and Conzemius (2002), who used a modified model from Wyngaard and Brost (1984), are provided in Fock (2007, p. 47 – 49): The resulting vertical profiles of horizontal averaged potential temperatures, resolved vertical heat fluxes and second order moments of potential temperature and vertical wind speed are quite promising in terms that the principle features of free CBLs can be simulated reliably with METRAS-LES. The profiles indicated a slightly higher numerical diffusivity found in METRAS-LES compared to the model used by Fedorovich and Conzemius (2002). But in general the differences are in an acceptable range similar to differences seen in other model intercomparisons between different LES models (e.g. Fedorovich et al. 2004).

To widen the range of models, applied for indirect model validation of METRAS-LES, the model PALM (Raasch and Schröter, 2001; Raasch and Etling, 1991) has been used to perform a second model intercomparison experiment. The model PALM is an interesting choice for a second benchmark model for METRAS-LES as there is already a model intercomparison study between METRAS-RANS and PALM: Lüpkes et al. (2008) compared results of a coarse resolution ($\Delta x = 200$ m) 2-dimensional version of METRAS applying a customized RANS closure for simulating convection above leads in Arctic sea ice with results of a 3-dimensional large eddy simulation carried out with PALM on a much finer grid ($\Delta x = 10$ m). The simulations discussed below add a model intercomparison at the same grid resolutions and using the same SGS closure.

The simulation of the developing CBL described in Section 3.2.1 is once carried out with METRAS-LES (CBL_M, —)[4] and once with PALM (CBL_P , —). The simulation with PALM is set up similar to the simulation with METRAS-LES so that both CBL_M and CBL_P fulfill the test case defined above. Nevertheless, different model features are kept as well: CBL_P applies a stochastical parameterization which adds random fluctuations on the horizontal velocity components if the resolved TKE is below a certain threshold value. CBL_M only adds some random fluctuations on the prescribed heat flux in the first time step to initialize the development of convection (Section 3.2.1). Even though the model set-ups have been done with care, some model parameters have been set slightly different. This is a common issue in model intercomparison experiments, which is hardly avoidable and reflects – in a certain amount – the different physical and numerical approximations typically applied by the individual models. An overview of known different features and settings for both models is given in Table 3-1.

---

[4] To ease reading short names for individual simulations are followed by the color used in plots to mark these simulations. All simulation names are also listed on page 109.

Table 3-1: : Known difference between the simulations CBL_M and CBL_P. Common settings are specified according the case definition in Section 3.2.1.

	METRAS-LES (CBL_M, —)	PALM (CBL_P, —)
Numeric momentum advection	2nd order ENO, (Harten et al. 1987; Schroeder et al. 2006)	Piacsek and Williams (1970)
Numeric scalar advection	Flux correction method	Piacsek and Williams (1970)
Solution Poisson equation for dynamic pressure	Bi-CGSTAB (e.g. Saad 2003, p. 244–247)	Solved in spectral space (Schumann and Sweet 1988 ; Siano 1997, p. 11) with Thomas algorithm, using FFT for transformation to/from spectral space
Time stepping	2nd order Adams-Bashforth scheme for momentum equation, Euler forward for scalar variables, with special treatment of dissipation in SGS-TKE (Section 3.1.3)	Runge-Kutta 3rd order (Williamson 1980)
Lateral boundary conditions	Open lateral boundaries (Schlünzen et al. 2012a, p. 54ff.)	Cyclic lateral boundaries
Grid cells	128 x 128 x 104	128 x 128 x 106
SGS TKE	Lower value for Prandtl layer parameterization, (Section 4.3.2), neglecting of pressure correlation terms	Reduction of mixing length near the surface, modelling pressure transport term with gradient approach (e.g. Heinze 2013, p. 20)
Stochastic perturbations	Initial perturbation (white noise) of surface heat flux during first time step	Random disturbance of horizontal wind components every 150 s with an amplitude of 0.25 m s^{-1} for model levels between 50 m and 670 m. Disturbance continued as long as a maximum limit for the model domain disturbance energy is lower than 0.01 m^2 s^{-2}
Earth's angular speed of rotation Ω, Coriolis parameter	$\Omega = 0.72922 \times 10^{-4}$ rad s^{-1} $f = -0.973 \times 10^{-4}$ s^{-1} $f^* = 1.09 \times 10^{-4}$ s^{-1}	$\Omega = 0.729 \times 10^{-4}$ rad s^{-1} $f = -0.94 \times 10^{-4}$ s^{-1} $f^* = 1.12 \times 10^{-4}$ s^{-1}
Model (version)	METRAS-LES (r559)	PALM (Release 3.7a, r552)
Computer	IBM Power6 (DKRZ)	Cray XT4 (BCCS)

Instantaneous snapshots of cross sections of vertical wind speeds are presented in Figure 3-4 and Figure 3-5, taken after one hour of continuous surface heating. The one-hour heat supply at the surface releases 433.8×10^3 J m^{-2} to the model atmosphere, as the heating rate is approximately 120.5 W m^{-2} (Figure 3-1).
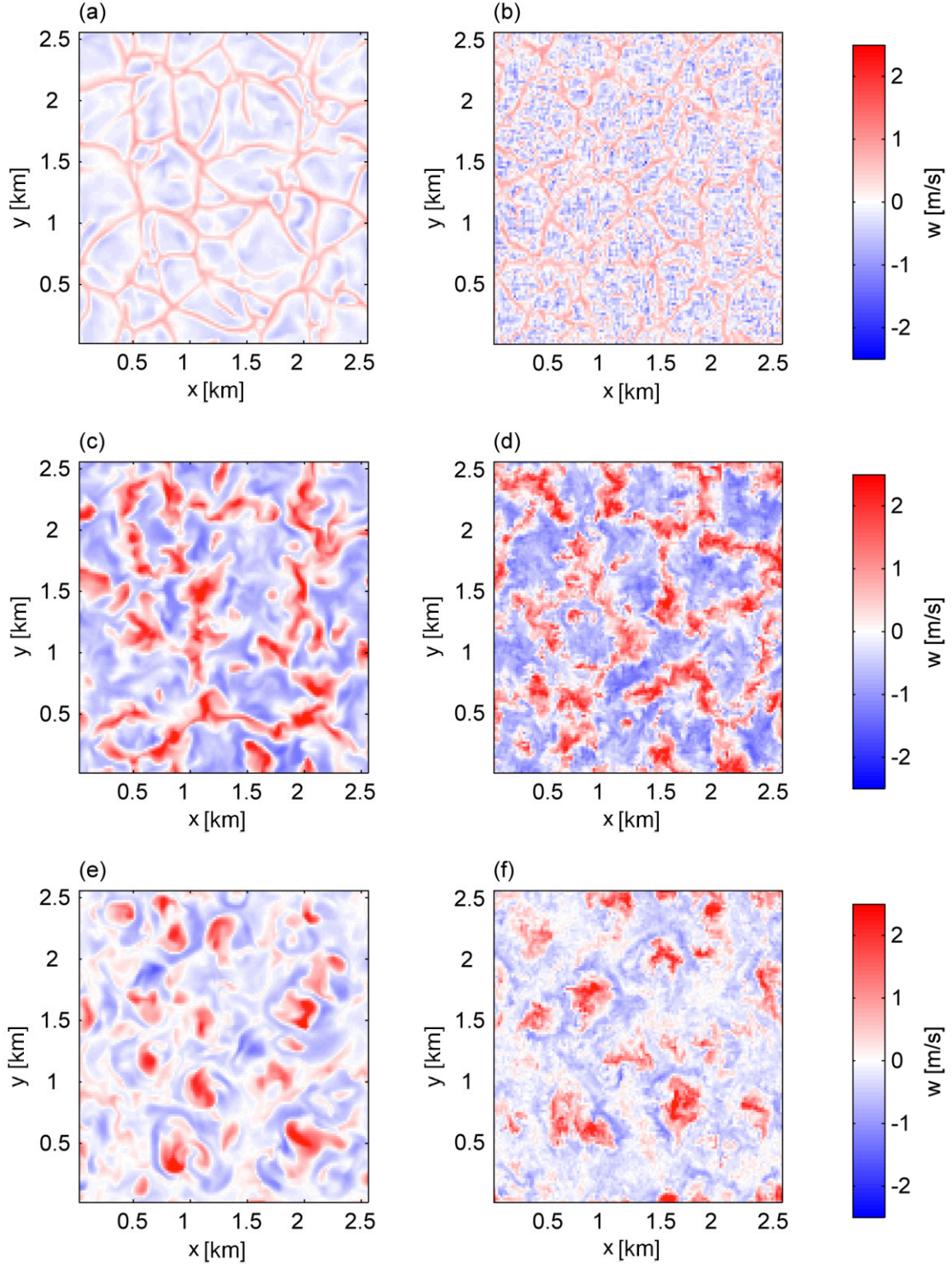

Figure 3-4: Instantaneous horizontal cross sections of vertical wind speed for the model experiments CBL_M (left) and CBL_P (right) after 01:10 h integration at 20 m (a) – (b) and 100 m (c) – (d) and 500 m (e) – (f) above the surface.
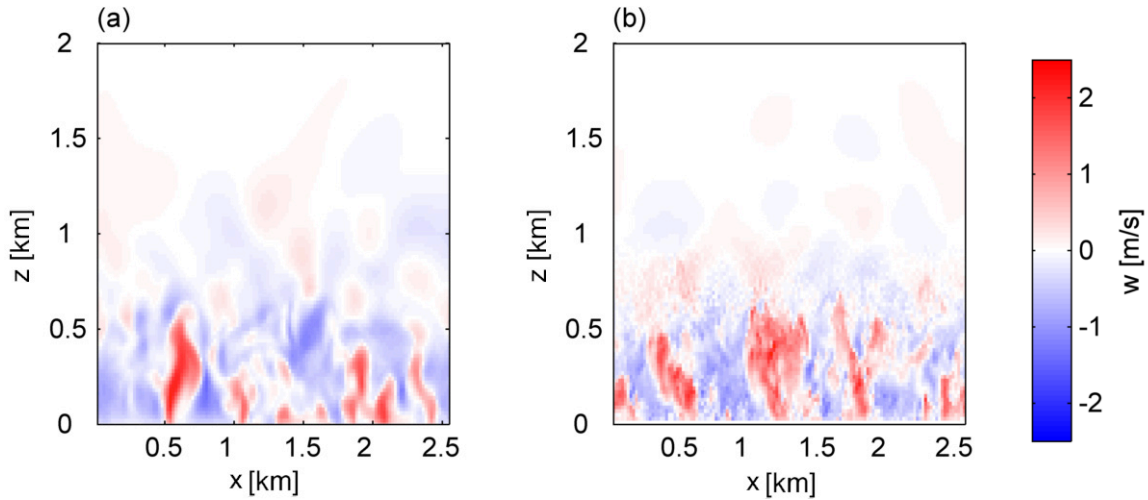
Figure 3-5: Instantaneous vertical cross sections at of vertical wind speed at y = 1200 m after 01:00 h for the model experiments CBL_M (a) and CBL_P (b).

The exact individual locations of the observed convective plumes are different for CBL_M and CBL_P due to the random nature of simulated process. Therefore the two model results can only be compared in terms of their structural and statistical behavior. The larger scale structures occurring in the vertical wind fields look similar for both models.

The magnitudes of the vertical winds are similar for both models at different heights (Figure 3-4). Hexagonal cells with similar diameters are observed at altitudes 20 m above the surface (Figure 3-4 (a) – (b)). Distinguishable up- and downdrafts can be seen from cross sections (Figure 3-5) in the lowest 500 – 700 m. The minimum (maximum) of vertical wind speed in the complete model domain is -1.6 m s^{-1} (3.3 m s^{-1}) for CLB_M and -2.1 ms^{-1} (3.9 m s^{-1}) for CBL_P. The vertical cross sections of vertical wind speed (Figure 3-5 (a)) suggest that boundary layer height might be similar in both models.

The main difference between the two simulations seems to be in the smaller scale structures. It is obvious from the comparison of cross sections (Figure 3-4 and Figure 3-5) that the simulation CBL_P shows finer grained structures than the simulation CBL_M. There are several possible reasons for this finding:

▪ Numerical diffusion due to different applied numerical schemes (Table 3-1) might be different for the two models. This can hardly be investigated in a model intercomparison, because many model differences influence the results. Instead, a comparison of the different numerical schemes available in METRAS-LES is following in Section 3.3.2.

▪ Use of horizontal open boundary conditions may also contribute to less small scale features in CBL_M. Ansorge (2009) found by spectral analysis of METRAS-LES results of the same CBL case (but another realization with some slightly different model settings) that the small scale variance in the boundary normal

wind component is reduced and claims that this may hint to some additional diffusivity introduced by the lateral boundary conditions. The cyclic boundary conditions applied in PALM should not impact the small scale fluctuations.

- The stochastical forcing applied in PALM seems to be the most striking reason for the observed differences as this explicitly adds energy to the small scales based on a priori assumptions.

Spectral analysis is performed for the vertical wind speed w, to investigate the found differences in the small scales in more detail. This will be used to answer the question, if these differences are a serious constrain or not and will additionally provide a measure on the effective model resolution.

The spectral analysis builds on one-dimensional Fourier spectra taken along grid lines in one horizontal model dimension in a certain height. All spectral coefficients are taken along one dimension and thereafter averaged along the other horizontal dimension. As 128 x 128 grid cells have been used for the horizontal grid, each averaged spectra consists of averaged spectral coefficients of 128 one-dimensional spectra. This averaging reduces noise from the spectra. The limited domain and the Nyquist frequency (e.g. Weisstein 2014) limit the directly resolvable waves numbers to 64, which represent spatial scales from $128/2 \cdot \Delta x = 1280$ m to $2\Delta x = 40$ m. The spectral analysis used here is explained and tested in Fock (2007) and Fock (2008) for time series. The analysis routine has been extended for spatial spectra and included in a generic collection of MATLAB tools (Fock 2012, source: fsa.m). It uses the fast Fourier transformation available in MATLAB (MathWorks 2011) to compute the spectral energy density S (e.g. Stull 1988, p. 303 – 318). The original data are used for spectral analysis without detrending or windowing, i.e. a simple rectangular window is applied.

To account for the different spectral energy in the simulations CBL_M and CBL_P the spectral energy density has been normalized with the variance of the vertical wind speed $\sigma_w^2(z)$ taken in the same horizontal plane as the spectra (Figure 3-6).
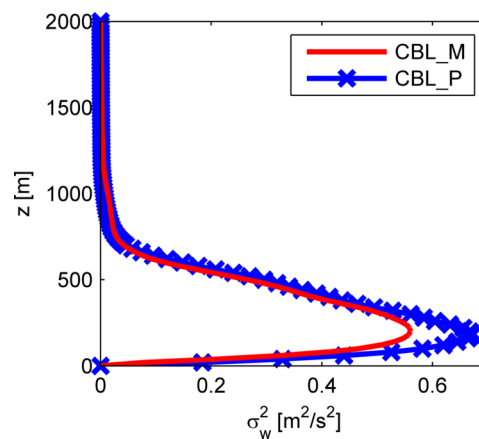

Figure 3-6: Variance of the vertical wind speed for the model experiments CBL_M and CBL_P.

The normalized spectral energy of CBL_M drops below those of CBL_P for wavelengths smaller a certain wavelength k_{eff} (Figure 3-7). These wavelengths have been estimated for each spectrum in Figure 3-7 by visual inspection. The values of k_{eff} are summarized in Table 3-2 and converted into length scales with the units meter and number of grid cells, using the grid length of $\Delta x = \Delta y = \Delta z = 20$ m.

Table 3-2: Effective cutoff wavelength of METRAS-LES without an additional stochastic parameterization (CBL_M) at different heights derived by comparison (Figure 3-7) with PALM including stochastically a forcing (CBL_P).

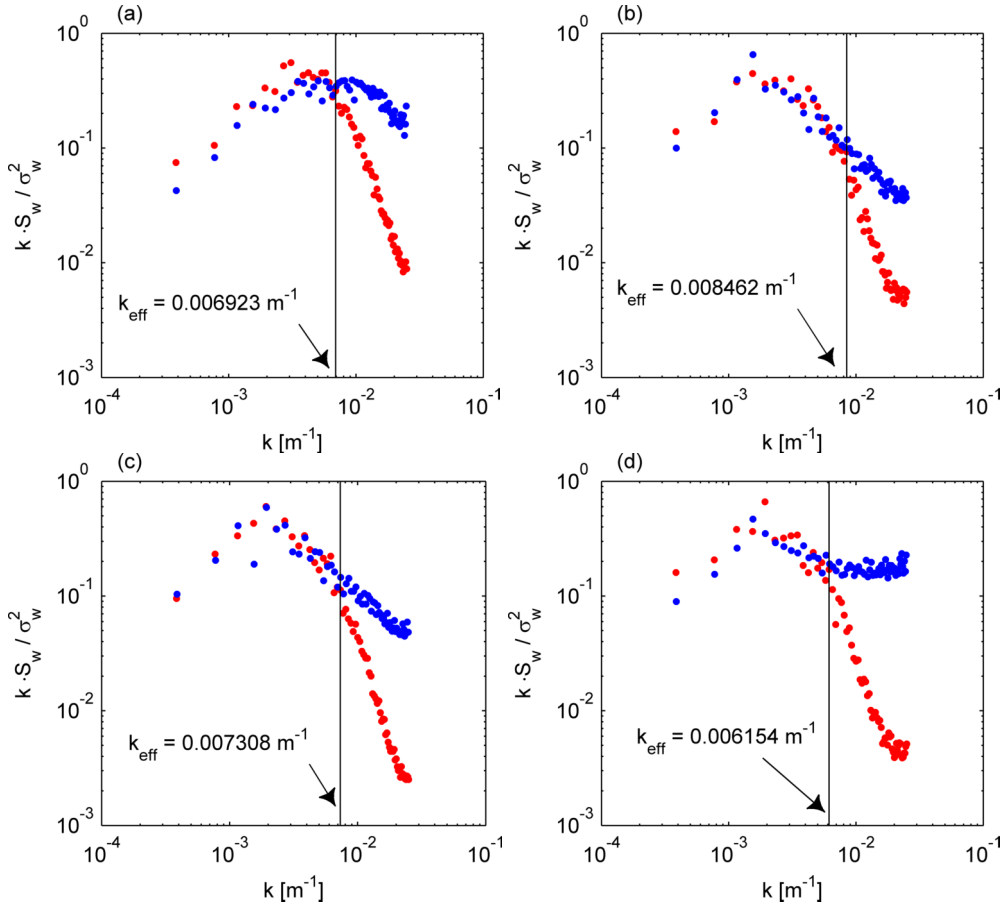| z [m]	k_{eff} [m^{-1}]	k_{eff}^{-1} [m]	$k_{eff}^{-1}/\Delta x$
20	6.923×10^{-3}	144	7.2
200	8.462×10^{-3}	118	5.9
500	7.308×10^{-3}	137	6.8
700	6.154×10^{-3}	162	8.1

Figure 3-7: Horizontal averaged one-dimensional spectra of vertical wind speed at 20 m (a), 200 m (b), 500 m (c) and 700 m (d) above the ground for the model experiments CBL_M (red) and CBL_P (blue). σ_w^2 used for normalization is shown in Figure 3-6.

The spectral differences between PALM and METRAS-LES become only evident at scales smaller than $6 - 8\ \Delta x$. With the assumption that the wavelength associated with the drop of the METRAS-LES spectra below the PALM spectra provide some measure

of the effective model resolution, the effective model resolution of METRAS-LES can therefore be quantified to 6 – 8 grid cells. The effectively resolvable scales are in the order of 150 m for a 20 m grid resolution. The effective model resolutions discussed above fall into the normal range for atmospheric models (Quante 2010; Petrik 2012, p. 51 – 82). The derivation of effective model resolutions by comparison of spectra is also discussed by Skamarock (2004).

In principle it is possible to mitigate the decline of model spectra by imposing some fine-tuned stochastical fluctuations to the model fields to fill in some energy into the higher wave numbers as done in the CBL_P. Such an additional modeling approach explains why the PALM spectra follow the $k \sim$ -5/3 decay proposed by Kolmogorov (1941) better. This approach somehow helps to reduce the problem that resolved spectra are always damped due to the discretization. But this approach is not without problems, as it requires more a priori knowledge about the situation to be simulated. For example in simulation CBL_P this stochastic forcing is applied between 50 m and 670 m, hence an assumption about boundary layer depth is made. Therefore this approach affects the ratio of model deliverables versus model inputs. Additional it is not guaranteed that such a stochastical parameterization always results in the desired effect. For example Figure 3-7 (d) shows an unphysical increase of spectral energy at small scales which is most likely due to the imposing of fluctuations above the CBL depth.

The analysis presented above and the preliminary results from Fock (2007) show that convective boundary layers can be reasonable well simulated with METRAS-LES, even though compared to other LES models a little less details are resolvable at small scales.

3.3 Model sensitivity

Before moving to the intended model applications – convective boundary layers above heterogeneous urban areas (Chapter 4 and 5) – three questions are answered by conducting model sensitivity studies:

- Is the model sensitive to the stability depended case distinction in the Deardorff SGS model?

- Which numeric methods available in METRAS are suited best for LES purposes?

- What are the influences of grid spacing and extension in the vertical direction?

The aim of these model studies is two folded: They are intended to find out an optimized setup of METRAS-LES for the following more applied simulations, but they also investigate details of the widely used Deardorff SGS model and hence might be of general interest for the atmospheric LES community.

The sensitivity studies are performed as variations against the setup introduced in Section 3.2.1. The role of the SGS model is investigated in Section 3.3.1. Influences of

numerical schemes are discussed in Section 3.3.2. Investigations of the sensitivity of the vertical grid spacing and extension are shown in Section 3.3.3.

3.3.1   Sensitivity on subgrid scale model

METRAS-LES is tested for sensitivity on the details of the SGS model. Therefore the simulations have been repeated with a simplified subgrid scale model, in which Equation (3.16) is simplified to $l = \Delta$ regardless of the stability (CBL_D, —). The reference simulation includes the N_{BV} term in the length scale l (CBL_DN, ×). Minor differences of CBL_DN to the reference simulation of the other experiments might exist due to model development activities.

The analysis of this experiment is based on time averages of horizontally averaged profiles. First horizontally averaging (denoted by $< \cdot >$) has been performed over the complete model domain. The secondary time averaging is necessary because the instantaneous horizontal averaged profiles fluctuate in time due to the stochastic nature of the simulated flow. The time averaging is realized over a period of 15 min based on instantaneous model output performed every minute. The averaging interval has been chosen as compromise between the requirements of averaging a sufficient amount of profiles and the opposed need of using a short interval due to the unsteady nature of the simulated situation.

Figure 3-8 shows 15 min time averages of horizontally averaged profiles of the potential temperature θ and corresponding profiles of the Richardson number

$$Ri = \frac{g}{\theta}\left(\frac{\partial\theta}{\partial z} + \frac{0.61}{1+0.61\cdot q}\cdot\theta\frac{\partial q}{\partial z}\right)\cdot\left(\left(\frac{\partial u}{\partial z}\right)^2 + \left(\frac{\partial v}{\partial z}\right)^2\right)^{-1} \tag{3.40}$$

for the simulations CBL_DN and CBL_D. *Ri* has been calculated from three dimensional model output by a generic post processing tool developed by Fock (2012, source: memi_post.m) and is bounded to the interval [-5 , 0.1999]. The same limiting interval for the Richardson number has traditionally been used by METRAS-RANS for the calculation of exchange coefficients (Schlünzen et al. 1996a, p. 26), but these limits have been recalibrated for METRAS-RANS recently (Hoffmann 2012, p. 62; Schlünzen et al. 2012a, p. 24).

The shapes of the potential temperature profiles (Figure 3-8 (a)) are very similar for both simulations: A super adiabatic layer near the surface is topped with a well-mixed neutral stratified layer above, which lays under a stable layer which follow the initial temperature profile. The Richardson number increases correspondingly fastest with height near the surface and reaches positive values above the entrainment zone (Figure 3-8 (b)).

Even though both Richardson number and potential temperature profiles look very similar for both cases small difference exist in the results of the simulations CBL_D and

CBL_DN: Using the sign change of the Richardson number as a measure for the boundary layer height

$$z_i(Ri): z_i \to z \text{ with } \langle Ri(z) \rangle = 0 \qquad (3.41)$$

gives a 5.6 % higher boundary layer height in the modified simulation CBL_D (Table 3-3, Figure 3-8). Hence, the boundary layer height is slightly larger for the case CBL_D.
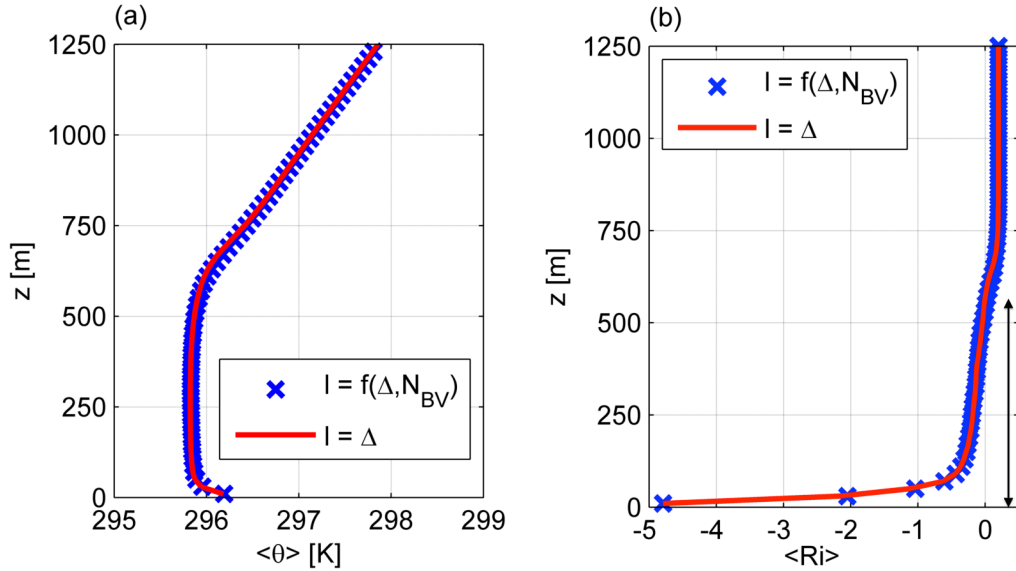

Figure 3-8: Horizontal averaged profiles in the developed convective boundary layer averaged over 15 min (01:15 - 01:29) of the potential temperature (a) and Richardson number (b) for the model experiments CBL_DN (marked in blue) and CBL_D (red). The characteristic height $z_i(Ri)$ is drawn by an up down arrow (b).

Table 3-3: Null of Richardson number (Figure 3-8), position and value of (relative) maxima of the variance of vertical wind and potential temperature (Figure 3-9), position and value of minimum of the resolved heat flux (Figure 3-10) for a 15 min average (01:15 to 01:29) from the results of simulations CBL_D and CBL_DN.

	CBL_D ▬	CBL_DN ✕
$z_i(Ri)$	568 m	538 m
$z_{\max(\sigma_\theta^2)}$	690 m	670 m
$\sigma_\theta^2(z_{\max(\sigma_\theta^2)})$	0.0224 K²	0.0198 K²
$z_{\max(\sigma_w^2)}$	200 m	200 m
$\sigma_w^2(z_{\max(\sigma_w^2)})$	0.789 m² s⁻²	0.763 m² s⁻²
$z_i(HF)$	640 m	640 m
$HF(z = 640 m)$	-10.1 W/m²	-11.2 W/m²

The simulations CBL_D and CBL_DN are also very similar (Figure 3-9) in variance profiles of vertical wind speed $\sigma_w^2(z)$ and of potential temperature $\sigma_\theta^2(z)$. Similar to

the profiles of the first moments, these second order moments have been calculated from horizontal layers over the entire model domain. They also apply the same 15 min time averaging. The results of CBL_D has a slightly larger (13.3 %) maximum of σ_θ^2 (Figure 3-9 (b), Table 3-3) than those of CBL_DN in the entrainment zone. The maximum is also located at a 3 % higher altitude. The maximum of σ_w^2 shows higher values for CBL_D (3.4 %) as well, but this maximum is located at the same height for both simulations (Figure 3-9 (a), Table 3-3). The finding that both z_i and $\max(\sigma_w^2)$ are lager in CBL_D than in CBL_DN is somehow consistent with mixed layer similarity theory, because according Arya (1995) it can be assumed that σ_w is proportional to the convective velocity scale $w_* = (z_i \cdot g / T_0 \cdot (\overline{w'\theta'})_0)^{1/3}$, introduced by Deardorff (1972). At the upper part of the boundary layer slightly higher values for σ_w^2 are observed for the case CBL_D (Figure 3-9 (a)). All these findings also suggest that the boundary layer for the case CBL_D shows a slightly more intense growth rate.
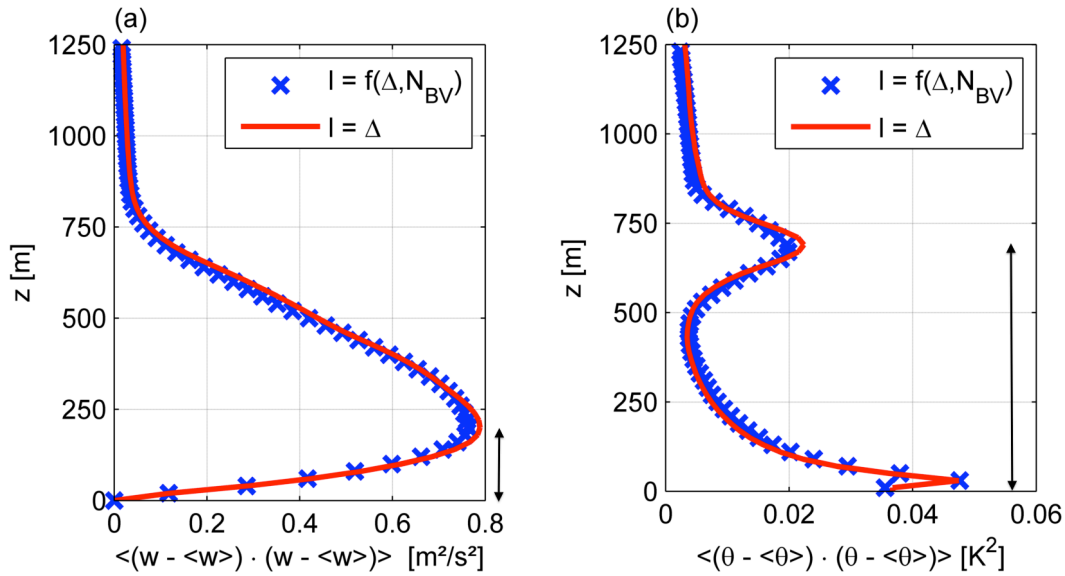

Figure 3-9: Variance of vertical wind speed (a) and potential temperature (b) for the model experiments CBL_DN (blue) and CBL_D (red). The variances are calculated individually for each model level averaged over 15 min (01:15 – 01:29). Up down arrows visualize the characteristic heights $z_{\max(\sigma_w^2)}$ (a) and $z_{\max(\sigma_\theta^2)}$ (b).

The covariance of the vertical wind speed and the potential temperature is the resolved vertical heat flux in kinematic units. The resolved heat flux is transformed to caloric units by multiplication by the density ρ and the specific heat capacity of dry air c_p at constant pressure.

$$HF(z) = c_p \cdot \langle \rho \rangle \cdot \left\langle \left(\theta(z) - \langle \theta(z) \rangle \right) \cdot \left(w(z) - \langle w(z) \rangle \right) \right\rangle \tag{3.42}$$

The resulting averaged flux profiles (Figure 3-10 (a)) are also quite similar for CBL_DN and CBL_D. The minimum of the resolved heat flux (3.42) could serve as an alternative measure to define the boundary layer height

$$z_i(HF): z_i \to z \text{ with} \min(HF(z)) \tag{3.43}$$

which results in the same z_i(HF) = 640 m for both simulations. The minimum values of HF($z = z_i$) themselves differ (Table 3-3).

Overall, the comparison of CBL_N and CBL_D shows that sensitivity on the details of the subgrid scale model is quite small. One main reason for the similar results is the dominance of the resolved vertical heat flux over the subgrid scale heat flux (Figure 3-10). This finding is desirable for a LES model as the concept of large eddy simulation implies that its outcome should not depend very much on the subgrid scale exchange, as most of the fluxes should be resolved by the simulation (Raasch 2010, personal communication). But on the other hand it also means that the stability term kept in widely used Deardorff (1980) closure might be a historic relict of simulation on coarse grids which might be unnecessary for large eddy simulation with higher resolution (Fedorovich 2010, personal communication). Thus the case distinction in the time split approach for the integration of the dissipation term (Section 3.1.3, Appendix A) might be avoidable complexity.

The low impact of the subgrid scale model can also be caused by numerical diffusion, e.g. if the numerical exceeds the physical diffusion. An investigation on the influence of different numerical methods is provided in Section 3.3.2.
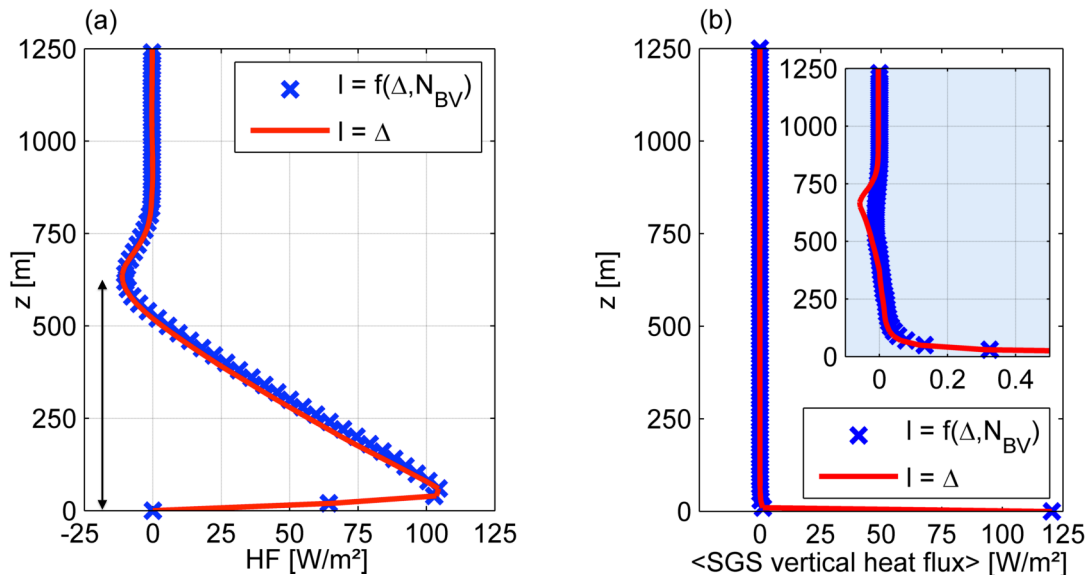

Figure 3-10: Resolved (a) and parameterized (b) vertical heat flux with length scale l = Δ (CBL_D, marked in red) and l = f(Δ,N_{BV}) (CBL_DN, blue). The parameterized vertical heat flux (b) is plotted twice to allow two different scales on the abscissa. Both drawings in (b) have the same physical units (e.g. [Wm^{-2}] on the x and [m] on the y-axis). The characteristic height z_i(HF) is drawn by an up down arrow (a).

3.3.2   Sensitivity on applied numerical methods

Different numerical schemes are available in METRAS. In this work mainly the standard schemes recommended for METRAS-RANS have been used. Exceptions are the new time discretization for the TKE equation (Section 3.1.3) and the choice of the advection scheme for the momentum equation.

The influence of the advection scheme is investigated with the CBL test case described in Section 3.2.1. The reference case is the default setting - a 2nd order central scheme including an additional the 7 point Shapiro (1971) filter (CBL_CDF, —). This run is compared with the same setup but using a 2nd order ENO scheme (Schroeder et al. 2006; Harten et al. 1987) without a filter (CBL_ENO, —).

The cross section of vertical wind shows thicker structures for CBL_CDF than for CBL_ENO (Figure 3-11). This indicates a higher overall diffusivity in CBL_CDF, which is due to the employed Shapiro filter in CBL_CDF. The spectra in Figure 3-12 show that lower frequencies are less resolved in CBL_CDF than in CBL_ENO. Both simulations look physically convincing. Even though this test setup does not reveal which setup is closest to nature, the choice of the ENO scheme for METRAS-LES has the advantage that this setup shows smaller total numerical diffusion at small scales, which increases the effective model resolution based on the available methods. Leaving out the filter in the central scheme, as alternative to reduce model diffusivity, is not advisable, as some artificial diffusion is needed for stability reasons (Schultze 2013). Therefore, the ENO scheme is recommended for METRAS-LES. For all other numerical methods the default schemes of METRAS are also applied in METRAS-LES. The used schemes are listed in Table 3-1.
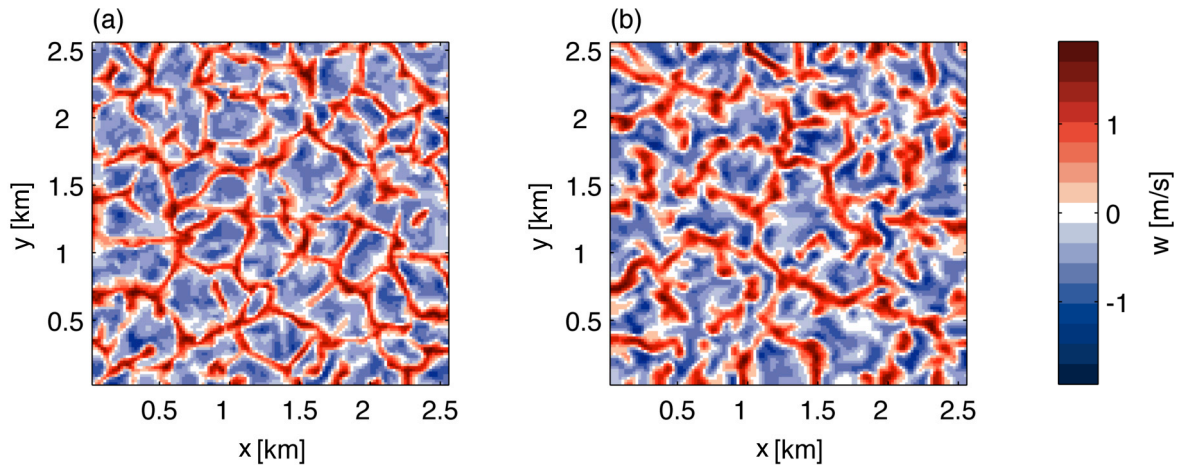

Figure 3-11: Horizontal cross section of vertical wind speed at 70 m above the surface for the model experiments CBL_ENO (a) and CBL_CDF (b).
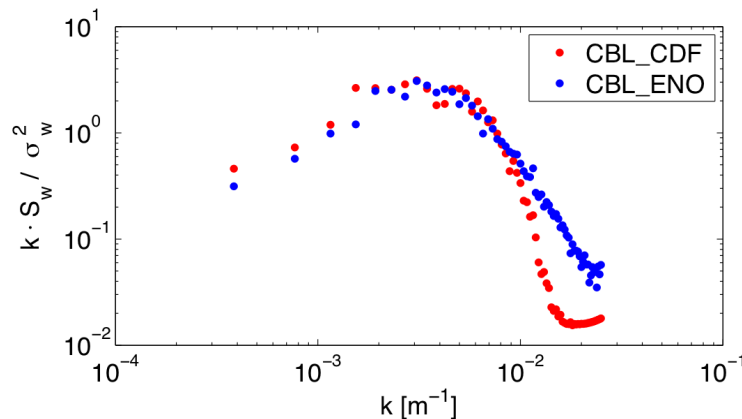

Figure 3-12: Spectra of vertical wind speed at 70 m above the surface after 30 min integration time for the model experiments CBL_ENO (blue) and CBL_CDF (red).

3.3.3 Sensitivity on vertical grid spacing and extension

Regarding the vertical grid spacing and extension two different points should be clarified:

- In order to allow relative flat model domains in simulations of growing CBL it is worth knowing at what boundary layer height interactions with the model top occur, which disturb the results. Thus an experiment is performed to determine the minimum required distance between the top of the model domain and the top of a simulated CBL for undisturbed simulations. This investigation is intended to judge on the required vertical grid extent for idealized simulations with METRAS-LES, like those shown in the previous sections.

- For the incoming shortwave radiation, important for the simulations in Chapter 4 and 5, METRAS assumes the model top at typical mid latitude tropopause heights (Schlünzen 2014, personal communication). Thus the simulation of diurnal cycles in Chapter 4 and 5 requires a vertical extent of the model domain representative for the whole troposphere. To fulfill this demand, but avoiding unnecessary computational costs, vertical grid stretching might be usable. In the following it is investigated, if grid stretching can be applied to simulations of the CBL with METRAS-LES without disturbing the simulation results. This investigation is intended to judge if grid stretching is feasible for simulations with METRAS-LES.

To test the model results for their sensitivity on the vertical grid extension and stretching the simulations of the CBL case have been repeated with varied vertical grids. The reference simulation (CBL_104, —) uses the same equidistant vertical grid as the simulations discussed in Sections 3.2 to 3.3.2 and is repeated in two modifications:

- One simulation is carried out with the half number of vertical grid cells keeping the vertical grid size the same (CBL_052, —). This setup is suitable to investigate the model response on a limited vertical grid domain and on the Rayleigh damping (e.g. Schlünzen et al. 2012a, p. 53) applied to the upper six[5] model levels. The simulation time has been extended to 3 h continued surface heating to investigate the model behavior in the unphysical limit when the convective plumes hit the upper boundary.

- The second sensitivity experiment (CBL_036, —) extends the vertical grid to 11 533 m, which is in the order of typical tropopause heights in the mid-latitudes. The number of grid cells is limited to 36 and vertical grid stretching is used. Only the lowest 200 m of the grid for simulation CBL_036 use the same 20 m vertical resolution as the simulations CBL_052 and CBL_104. This

---

[5] Standard setup in METRAS-RANS, compare se_ewical.f90 line 211–238 METRAS 2.0.4

provides a way to investigate the model behavior in regions with coarse resolution. The stretching factors used are taken from the default setup for METRAS-RANS.

Grid parameters for all three configurations are summarized in Table 3-4. A drawing is given in Figure 3-13. Only the upper levels of the stretched grid are distinguishable in Figure 3-13 to keep the figure at reasonable size / the drawn lines at visible width.
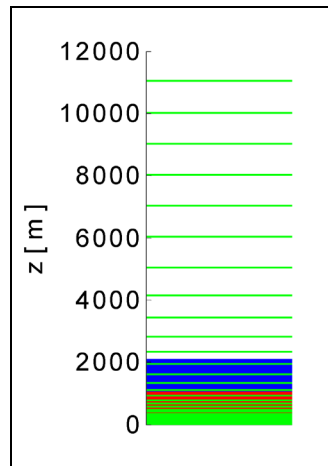

Figure 3-13: Vertical model levels used for sensitivity study on vertical grid: CBL_104 (blue), CBL_052 (red) and CBL_036 (green). Corresponding grid parameters are provided in Table 3-4.

Table 3-4: Grid parameters for the sensitivity studies on vertical grid spacing and extension. The index $_k$ - used to describe vertical levels - is increasing from the surface towards the model top. A drawing of the grids is given in Figure 3-13.

	CBL_104 —	CBL_052 —	CBL_036 —
No. of vertical levels	104	52	36
Height of model grid z_t	2 080 m	1 040 m	11 533 m
Lowest damping layer z_a	1 960 m	920 m	5 533 m
Vertical grid spacing			
for z < 200 m	20 m	20 m	20 m
for z > 200 m	20 m	20 m	$\Delta z_k = \max(\Delta z_{k-1} \times 1.22, 1\,000$ m$)$

Vertical cross sections of instantaneous model states of potential temperature and vertical wind speed are shown in Figure 3-14 and Figure 3-15. The shown time slices, 0:45 h, 1:45 h and 3:00 h, are equivalent to a time integrated heat flux (Section 3.2.1) of $326 \cdot 10^3$ Jm^{-2}, $760 \cdot 10^3$ Jm^{-2} and $1.3 \cdot 10^6$ Jm^{-2}, respectively, prescribed (Section 3.1.4) at the surface.

All three simulations show similar structures after 0:45 min: Rising plumes are shallower than the top of the flattest model domain (1040 m; CBL_052). The individual locations are different between the three simulations, which means that the different vertical grids can be understood as a way to create independent realizations of an

ensemble. After 1:45 h simulation time horizontal inhomogeneities above 1040 m become visible in the simulations CBL_104 and CBL_036 (Figure 3-14 (e) – (f), Figure 3-15 (e) – (f)). Hence, an influence of the lower model domain is possible for the simulation CBL_052 at least from 1:45 h onwards. This influence becomes clearly visible in the cross sections at 3:00 h integration time, when interaction with the model top seems to cause larger plume structures (Figure 3-15 (g) – (h)) and higher average potential temperatures (Figure 3-14 (g) – (h)) in CBL_052 than in CBL_104.

The influence of the vertical grid stretching can be judged by comparing the cross sections from the simulation CBL_036 with those of CBL_104 (Figure 3-14, Figure 3-15). Beside the missing small scale structures the results of CBL_036 and CBL_104 are remarkable similar. This provides some first evidence that vertical grid stretching can most likely be used for simulations of CBL with METRAS-LES without disturbing the model results.
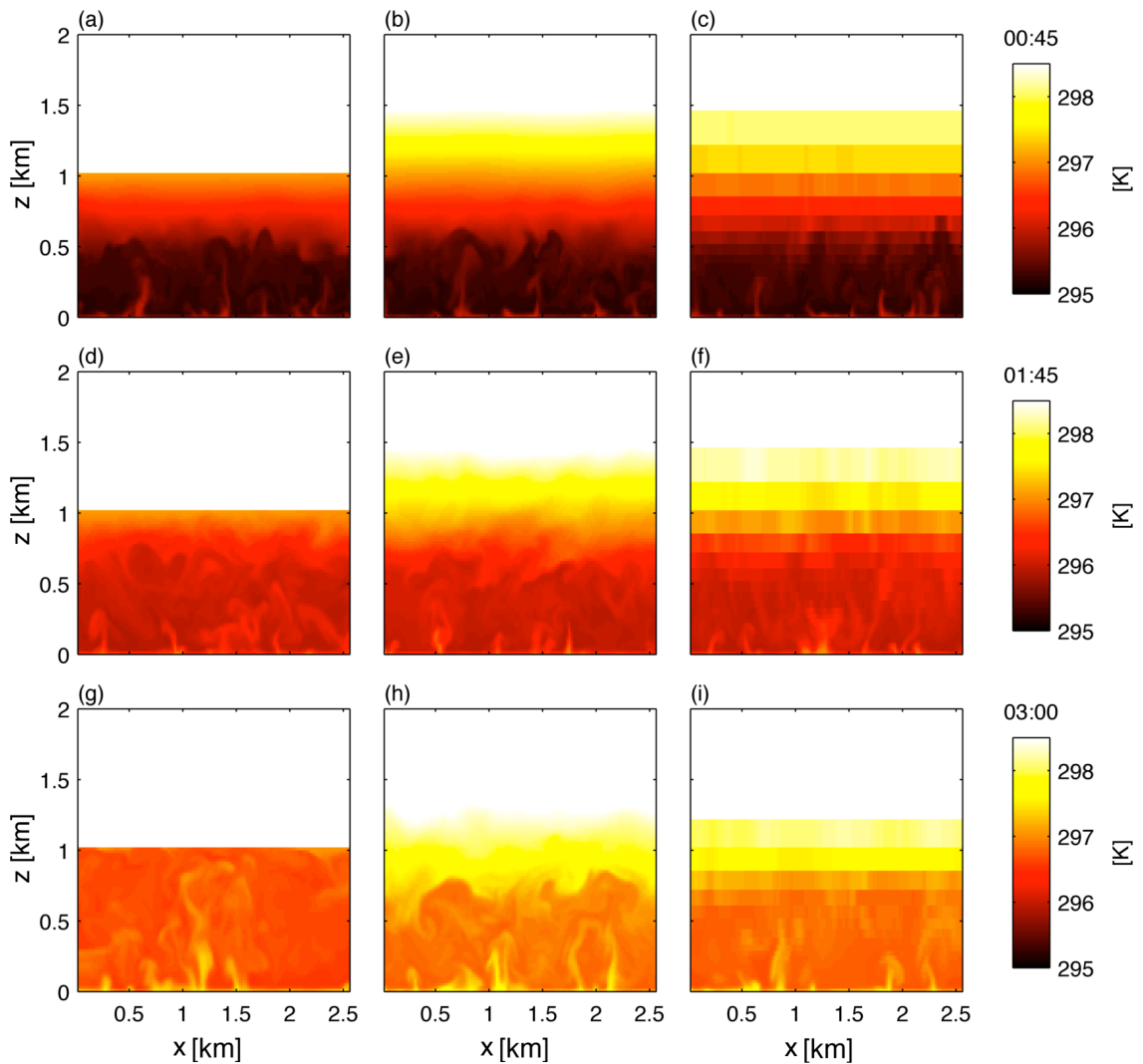

Figure 3-14: Vertical cross section of potential temperature taken in east west direction (1300 m northwards of the southern boundary) after 0:45 h (a) – (c), 1:45 h (d) – (f) and 3:00 h (g) – (i) integration time. For CBL_52 (a,d,g) the white space in the area above 1 km represents the end of the model domain, while for CBL_104(b,e,h) and CBL_036 (c,f,g) the white areas are caused by the selected color scale.
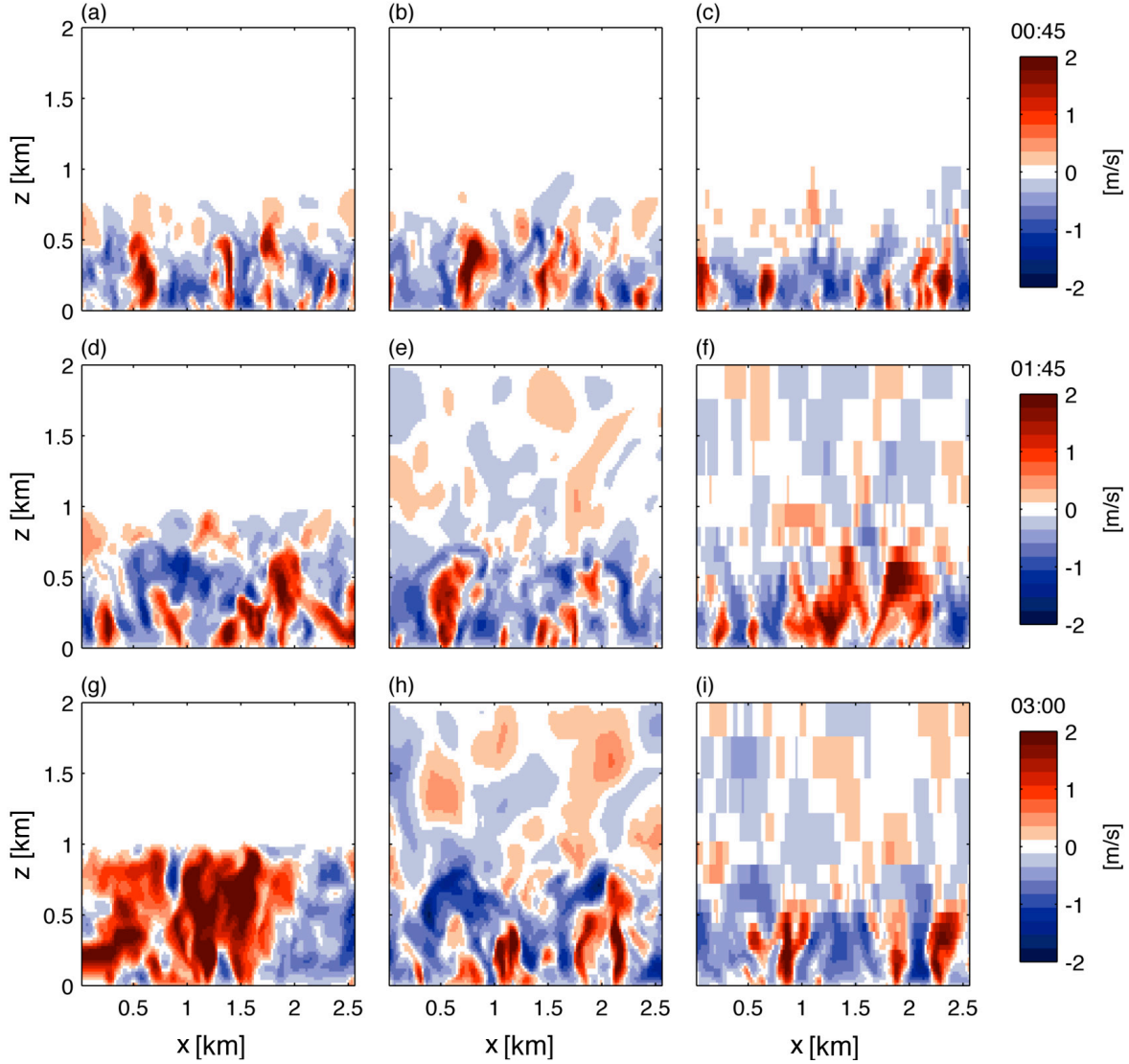
Figure 3-15: Vertical cross section of vertical wind speed taken in east west direction (1300 m northwards of the southern boundary) after 0:45 h (a) – (c), 1:45 h (d) – (f) and 3:00 h (g) – (i) integration time. For CBL_52 (a,d,g) the white space in the area above 1 km represents the end of the model domain, while for CBL_104(b,e,h) and CBL_036 (c,f,g) the white areas are caused by the selected color scale.

The temporal development of area averaged profiles is investigated in terms of characteristic heights, to provide a more quantitative analysis of the influence of the vertical grid. These characteristic heights, which have been introduced in Section 3.3.1, characterize

- the minimum of the resolved heat flux, i.e. $z_i(HF)$

- the null of the Richardson number, i.e. $z_i(Ri)$

- the maximum of the variance of the vertical wind speed, i.e. $z_{\max(\sigma_w^2)}$

- the secondary maximum of the temperature variance, i.e. $z_{\max(\sigma_\theta^2)}$

Figure 3-16 shows time series of the four characteristic heights together with the (scalar) model levels of CBL_032. The time series are calculated from instantaneous three dimensional model variables written out at an interval of 60 s.
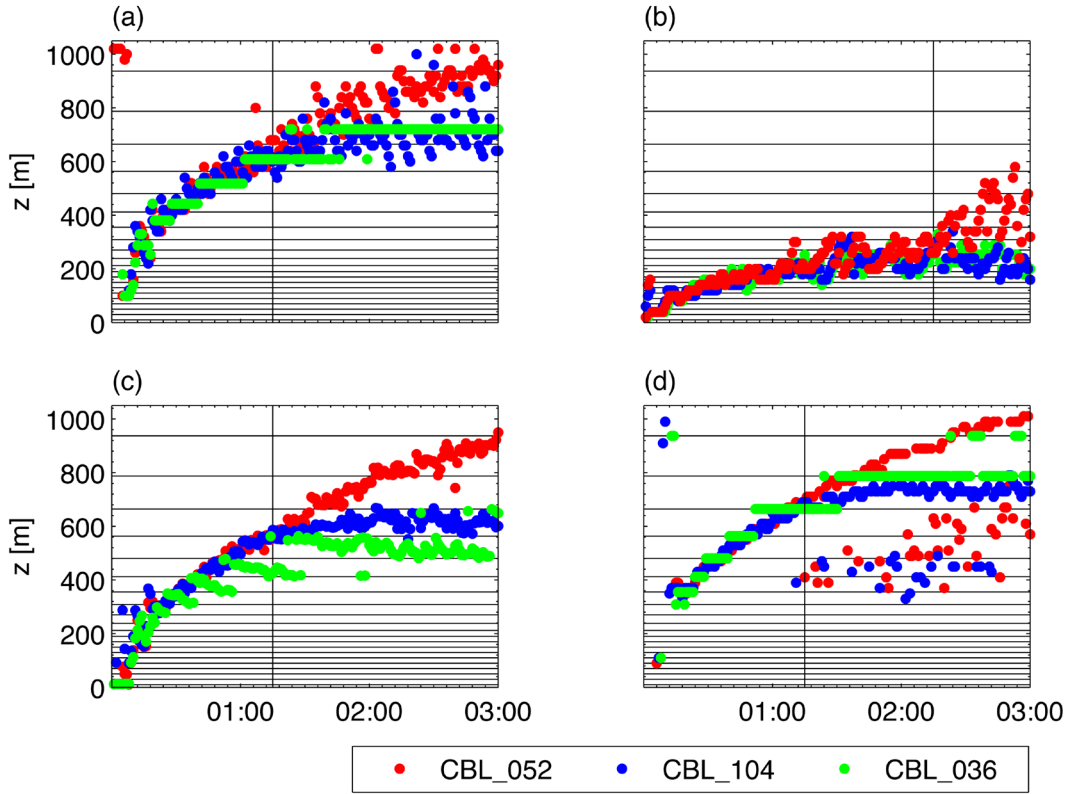

Figure 3-16: Scalar model levels for the grid of CBL_052 are drawn as horizontal lines, the times 1:15 and 2:15 are marked by vertical lines together with the time series of the characteristic heights (a) z_i(HF), (b) $z_{\max(\sigma_w^2)}$, (c) z_i(Ri) and (d) $z_{\max(\sigma_\theta^2)}$.

Up to an integration time of 1:15 h (marked by vertical line in Figure 3-16 (a), (c) and (d)) all four characteristic heights show a similar development in CBL_104, CBL_052 and CBL_032. This is consistent with the ad hoc judgment based on vertical cross sections after 0:45 (Figure 3-14 (a) – (c) and Figure 3-15 (a) – (c)).

The characteristic heights $z_{\max(\sigma_\theta^2)}$, $z_i(Ri)$ and $z_i(HF)$, which all characterize the height of the CBL, start to deviate between CBL_104 and CBL_054 after 1:15 h integration time or correspondently after 543×10^3 J m^{-2} heat supply. This indicates that the simulations of CBL with METRAS-LES are not affected by the top of the model domain, as long as the top of the CBL, measured by z_i(HF) here, stays approximately below 55 % of the domain height z_t (Grid parameters are provided in Table 3-4.). The deviation of CBL_054 from CBL_104 is first detectable in the upper part of the modeled atmosphere. After 2:15 h (977×10^3 J m^{-2}) also lower parts of the model atmosphere are affected by the domain size, which can be seen from the increase in spread of $z_{\max(\sigma_w^2)}$ in Figure 3-16 (b). Approximately $z_{\max(\sigma_w^2)}$ is at 25 % and z_i(HF) at 65 % of the domain height of CBL_054 at this time (Table 3-5). Hence, if z_i(HF) grows above 65 %

of the domain height the simulation will be disturbed by the artificial upper boundary also within the lowest 25 % of the domain.

The required vertical grid extend, can also be characterized in terms of required space between the entrainment zone and the lowest damping layer. Numbers are given in Table 3-5. The simulation used in the previous sections used the vertical grid from CBL_104 and only data from the first 90 min. Therefore with the analysis from above it can be concluded, that besides experiment CBL_054 no other simulation presented in this chapter should be disturbed by the model top.

Table 3-5: Characteristic heights for the reference run CBL_104, visually interpolated to the 2 times 1:15 and 2:15 from Figure 3-16. Normalization is done with the domain height z_t = 1040 m and the height of the lowest absorbing layer z_a = 920 m, both taken from the "flat grid" experiment CBL_052.

	1:15 h simulation time			2:15 h simulation time		
	z	$(z_a - z)/z_a$	z/z_t	Z	$(z_a - z)/z_a$	z/z_t
$z_i(HF)$	600 m	0.35	0.58	700 m	0.31	0.67
$z_{\max(\sigma_w^2)}$	200 m	0.78	0.19	240 m	0.74	0.23
$z_i(Ri)$	585 m	0.36	0.56	618 m	0.33	0.59
$z_{\max(\sigma_\theta^2)}$	670 m	0.27	0.64	730 m	0.20	0.70

The stretched grid in CBL_036 causes that the characteristic heights z_i(HF), z_i(Ri) and $z_{\max(\sigma_\theta^2)}$ increase in larger steps, as the number of vertical grid levels is not sufficient to show a continuous evolution in Figure 3-16. Especially the characteristic heights z_i(HF) and $z_{\max(\sigma_\theta^2)}$, which only depend on the variances and covariances at model levels, jump to the next model level in CBL_032 whenever the corresponding curves for the higher resolved simulation CBL_104 reach the next grid level available in the CBL_032 grid. This shows how the stretched grid reduced the possible resolution without disturbing the resolved scales in an unphysical manner. For z_i(Ri) the agreement between CBL_032 and CBL_104 is less pronounced, as this quantity depends on vertical gradients. The characteristic height $z_{\max(\sigma_w^2)}$ is comparable between CBL_032 and CBL_104 for the whole simulation period and does not show a stepwise development, as it stays in the well-resolved region. This confirms the conclusion that the stretched grid does not impact the simulation of CBL with METRAS-LES, as long as only the well resolved model levels are analyzed.

This analysis shows that besides the obvious loss of details in regions with coarse resolution there is no harm in using stretched grids in METRAS-LES.

3.4 Conclusions

In this chapter results from developing and testing METRAS-LES have been presented, using simulations of free convective boundary layers above a flat and homogeneous surface as test case. Model development include:

- The derivation and implementation of a new implicit method for calculating the dissipation term in the SGS closure (Deardorff 1980) to overcome numerical problems with the existing explicit scheme, which caused unphysical negative SGS TKE (Section 3.1.3). A derivation for the implicit method could not be found in the literature and is thus given in detail in Appendix A.

- A modification of the surface layer scheme of METRAS to allow consistent prescription of heat fluxes at the model surface (Section 3.1.4).

- Exploration and implementation of metrics suitable for interpretation of LES of CBL (spatial spectra, variance profiles, characteristic heights).

Model tests of METRAS-LES show that:

- Vertical grid stretching is harmless for simulation of CBL with METRAS-LES, as long as only the well resolved parts are analyzed (Section 3.3.3).

- For the used CBL test case a model top z_t with twice the altitude as the depth of the CBL, measured by the characteristic height z_i(HF), is sufficient to ensure that no distributions by the upper model boundary occur (Section 3.3.3).

- The stability dependence of the length scale in the Deardorff closure has only little influence and seems to be negligible compared to other influencing factors (Section 3.3.1).

- The effective model resolution of METRAS-LES is in the order of $6 - 8 \, \Delta x$ (Section 3.2.3) and using the ENO scheme for momentum advection is of advantage to resolve small scales (Section 3.3.2).

The available open boundary conditions seem to work sufficiently for the given problem. This point is of general interest for the development of non-idealized atmospheric LES models, as the use of periodic boundary conditions limits model applications to simulations with periodic or semi periodic atmospheric conditions. As the aim of the development of METRAS-LES is to contribute to the step from applying LES for cyclic or semi cyclic landscapes to arbitrary heterogeneous terrain, the applied open boundary conditions might be an important feature as the landscape or the incoming large scale weather conditions might be far from being cyclic.

The performed model improvements correct some severe shortcomings of the model from Fock (2007). The performed studies show that the LES extension of the model METRAS can simulate the development of unsteady convective boundary layers reasonable, also compared to other LES models. Hence, the further developed METRAS-LES extends the range of physical phenomena investigable with the Multiscale Model System M-SYS.

4 LES above a city with simplified surface cover

This chapter introduces and tests the model features like detailed treatment of surface cover and orography, which are needed to advance the use of METRAS-LES from simulations above flat homogeneous terrain (Chapter 3) to simulations above heterogenic urban areas. A short review of related literature, model features and of topographic data, is provided in Section 4.1, including a definition of a new surface class mapping based on the CORINE land cover data. Model simulations are analyzed for the inner city and harbor area of Hamburg (Section 4.2 and 4.3) to demonstrate the applicability of METRAS-LES above heterogeneous surfaces and to study convective boundary layers above Hamburg. Model sensitivities regarding variations of the surface and the SGS modelling are analyzed in Section 4.3 to extract differences between METRAS-LES and METRAS-RANS and to provide guidance for further model development.

To allow a gradual increase of model complexity, to increase comparability with the results from Chapter 3 and to simplify sensitivity experiments simulations in this chapter still neglect the influence of humidity and use relative simple surface data. Further refined simulations of convective situations simulated with METRAS-LES for the model domain are discussed in Chapter 5.

4.1 LES above heterogenic surfaces

4.1.1 Heterogeneous surfaces in LES modelling

Recently, large eddy simulation above complex, none idealized terrain became more popular in the atmospheric modelling community. Some of the meteorological services try to extend their atmospheric models into the turbulence permitting regime, to tune their parameterizations or to learn how to produce forecasts at very small scale (e.g. projects like HD(CP)[2][6] or The GREY Zone Project [7]).

Basu et al. (2008) simulate a diurnal cycle driven by a heat flux calculated with Monin Obukhov similarity theory from temperatures observed at two heights during the Wangara experiment (e.g. Hess et al. 1981). Botnick and Fedorovich (2008) show diurnal cycles of convective boundaries based on observed heat and moisture fluxes in Lamont, Oklahoma. Patton et al. (2005) coupled an LES model with a land surface model to analyze the influence of idealized surface heterogeneities on wet and dry planetary boundary layers. For urban areas LES studies performed with obstacle resolving models often neglect effect of thermal stratification and focus on neutrally

---

[6] http://hdcp2.zmaw.de
[7] http://www.knmi.nl/samenw/greyzone

stratified situations (e.g. Letzel et al. 2012). Wang (2009) investigates the influences of urban circulations on convective boundary layers with idealized large eddy simulations prescribing different heat fluxes for urban and rural areas.

LES studies of convective boundary layers above an urban area are provided in the following parts of this thesis. The focus is on free convective situations with zero large scale wind forcing, which can be successfully simulated with METRAS-LES (Chapter 3) using the implemented radiative boundary conditions described in Schlünzen et al. (2012a, p. 54). Thus, no further work on prescription of resolved turbulent fluctuations on the lateral boundaries is needed here. Attempts to add fluctuations to the normal components of the wind vector at inflow cells of METRAS-LES are discussed in Philipp (2013). Such modifications would be needed to extend the studies presented here to atmospheric situations, in which large scale advection plays an important role.

4.1.2   Temperature and humidity at the surface of METRAS

The following review of the surface temperature and surface humidity scheme available in METRAS summarizes (and partly corrects) Schlünzen et al. (2012a, p. 49 – 51), Schoetter (2013, p. 67 – 68), Bohnenstengel (2012, p. 109 – 115) and Gierisch (2011, p. 10 – 11). It is intended to explain how atmospheric variables at the surface are modeled via settings of surface characteristics. Additionally it may help to understand why the calculation of an artificial surface temperature was a suitable modification to allow prescribed heat fluxes in idealized simulations with METRAS-LES (Section 3.1.4).

In order to simulate a diurnal cycle and to fulfill the surface energy budged

$$S_{net,j} + L_{net,j} + H_j + E_j = -Q_{g,j} \tag{4.1}$$

the following prognostic equation for the surface temperature is calculated

$$\frac{\partial T_{sfc,j}}{\partial t} = \frac{2\sqrt{\pi}\,k_{s,j}}{\nu_s h_{soil,j}}\left(S_{net,j} + L_{net} + H_j + E_j - \sqrt{\pi}\,\nu_{s,j}\frac{T_{sfc,j} - T_{soil}}{h_{soil,j}} \right) \tag{4.2}$$

separately for each (SGS) surface class. Multiple surface classes can be used within one grid cell. For each surface class (denoted by index j) not only surface temperatures $T_{sfc,j}$ but also the fluxes are calculated individually. Surface fraction weighted averages of these SGS fluxes are than provided to the prognostic atmospheric model variables. Equation (4.2) uses the force restore method (Bhumralkar 1975; Deardorff 1978) to handle the ground heat fluxes $Q_{g,j}$. The soil temperature T_{soil} is kept constant at a depth $h_{soil,j} = (k_{s,j} \cdot 86000\ s)^{0.5}$ during the whole integration period. Thermal diffusivity $k_{s,j}$ and thermal conductivity $\nu_{s,j}$ are prescribed per surface class, but the same constant deep soil temperature T_{soil} is used for all classes. The absorbed shortwave radiation is determined by the surface class specific albedo A_j, i.e. calculated by $S_{net,j} = S_\downarrow(1 - A_j)$. The incoming short wave radiation $S_\downarrow$ dependents on the solar zenith angle and cloud

conditions. The longwave radiation budgets $L_{net,j}$ use the Stefan-Boltzmann law, and are therefore functions of the 4th power of the surface temperature. The sensible and latent heat fluxes are calculated with the surface layer scaling variables, i.e. by

$$H_j = c_p \, \rho_0 \, u_{*,j} \, \theta_{*,j} \tag{4.3}$$

$$E_j = l_v \, \rho_0 \, u_{*,j} \, q_{*,j} \tag{4.4}$$

The calculation of the temperature scaling variable $\theta_{*,j}$ involves the calculation of vertical temperature gradients, which uses the surface temperatures according Equation (4.2). The fluxes of momentum and humidity are influenced by the surface temperatures indirectly via the stability functions (Equations (3.36) – (3.37)), which use $\theta_{*,j}$ in the Obukhov length (Equation (3.31)). The momentum roughness length z_0 over water surface classes is adjusted to the wind conditions as functions of the friction velocity u_*. The used roughness lengths for the scalar fluxes are set to $z_{0,\chi} = 0.1 \cdot z_0$ for most surface classes and to a roughness Reynolds number ($u_* \, z_0 \, / \, \nu$) dependent modification of z_0 to parameterize urban and water classes as hydrodynamic rough surfaces. Further details and references for these roughness length adjustments can be found in Schlünzen et al. (2012a, p. 21 – 23).

In order to calculate values for the specific humidity at the surface the following prognostic equation for the bulk soil water availability α is calculated

$$\frac{\partial \alpha_j}{\partial t} = \frac{P + \frac{E_j}{l_v}}{\rho_{water} W_{k,j}} \tag{4.5}$$

using the turbulent moisture flux $E_j \, / \, l_v$ and the precipitation rate P.[8] Initial values for α_j are prescribed individually for each surface class. Following Deardorff (1978) the specific humidity at the surface is than calculated as

$$q_{sfc,j} = \alpha_j \, q_{sat}(T_{sfc,j}) + (1 - \alpha_j) q_{z_p} \tag{4.6}$$

In Equation (4.6) q_{z_p} is the specific humidity in the first atmospheric model level and $q_{sat}(T_{sfc,j})$ the saturation humidity for the surface temperature.

With the above briefly introduced equations, heterogeneous surface cover / land use is represented in the model by a finite set of surface classes. For each surface class the values of albedo A_j, thermal diffusivity $k_{s,j}$, thermal conductivity $\nu_{s,j}$, initial soil water content $\alpha_{j,ini}$, soil water saturation $W_{k,j}$ and a roughness length $z_{0,j}$ are prescribed as

---

[8] The turbulent moisture flux in Equation (4.5) is documented incorrectly in Schlünzen et al. (1996a) / Schlünzen et al. (2012a), but implemented correctly in the model.

constants or class specific functions. This approach requires a mapping between appropriate topographic data to surface classes used by the model.

4.1.3   Specification of surface characteristics

Surface physics of the used METRAS version distinguishes surface characteristics for a set of 10 surface classes in the calculation of fluxes at the surface. The 10 standard classes (Schlünzen et al. 1996b) have been redefined for the model region based on the CORINE Land Cover 2000 data (EEA 2000). As 39 CORINE land cover classes occur in the model domain, aggregating of these classes was needed. The new mapping from 39 to 10 classes, named METRAS_URBAN in the following, has been defined as a look-up table (Appendix D.1) and is based on the CORINE data description and cross checks with satellite images in the visible spectral range, taken from Google Earth. The physical parameters for the new METRAS_URBAN classes (Table 4-1) are set by expert judgment and in consistency with the values of METRAS standard surface classes described in Schlünzen et al. (1996b, p. 25). The resulting map (Figure 4-1 (a)) shows only little details, i.e. the heterogeneity of the city is clearly underestimated. This is an effect of the granularity of the CORINE classification, which is much coarser than the desired grid resolution. The applied aggregation, as well as the rastering from the original shape representation (ESRI 1998) to the model grid, has only negligible influence on the degree of map detail. Due to the low granularity of the CORINE data 86.1 % of the grid cells are characterized by one single surface class (Table 5-3). The 13.9 % of grid cells with multiple surfaces classes are arranged along the borders of the main surface classes (Figure 5-2 (b),) Figure 4-1 (a)). Some artificial modification of the land use has been added to the map (Figure 4-1 (b)) to model the natural surface heterogeneity and to study the model sensitivity on small-scale surface cover variations (Section 4.3.1).
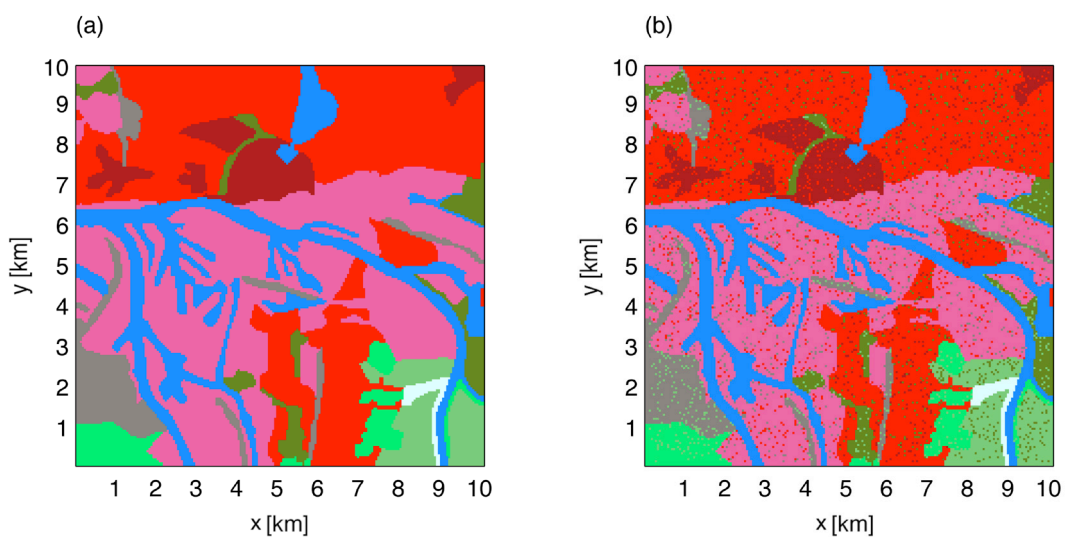

Figure 4-1: Main surface class in the model area (Hamburg, Germany) based on (a) CORINE data and (b) with random variations at grid scale (Section 4.3.1). The surface class mapping METRAS_URBAN (Appendix D.1) is used to set these classes. A color scale is provided together with the used physical surface characteristics in Table 4-1.

Table 4-1: Physical surface characteristics for the surface class mapping METRAS_URBAN: Albedo A, thermal diffusivity k_s, thermal conductivity v_s, soil water vailability α_{ini} (initial value for prognostic Equation (4.5)), saturation value W_k for soil water content W_s and momentum roughness length z_0. The mapping from the CORINE land use classes is given in Appendix D.1. f_1 is a function of zenith angle (Schlünzen et al. 2012a, p. 50). Following suggestions of Clarke (1970), f_2 is a function of the friction velocity u_* (Schlünzen et al. 2012a, p. 22).

Surface class mapping METRAS_URBAN		A_0	k_s [m² s⁻¹]	v_s [J (Ksm)⁻¹]	α_{ini} [m m⁻¹]	W_k [m]	z_0 [m]
Water	0	f_1	1.5×10^{-7}	100	0.980	100	f_2
Mudflat	1	0.10	7.4×10^{-7}	2.20	0.980	0.322	0.100
Harbor & Industry	2	0.20	2.3×10^{-6}	4.60	0.050	0.081	0.600
Mixed Vegetation	3	0.20	5.2×10^{-7}	1.33	0.200	0.138	0.040
Meadows	4	0.20	5.2×10^{-7}	1.33	0.400	0.015	0.020
Traffic	5	0.12	2.3×10^{-6}	4.60	0.05	0.015	0.005
Bushes	6	0.20	5.2×10^{-7}	1.33	0.300	0.081	0.100
Mixed forest	7	0.15	8.0×10^{-7}	2.16	0.300	0.121	1.000
Inner city	8	0.15	2.3×10^{-6}	4.60	0.025	0.484	1.400
Urban	9	0.15	1.4×10^{-6}	2.93	0.050	0.968	0.700

4.1.4 Orography and computational grid

As almost every city includes at least some orography, it might be important to include orography in an LES model intended for urban climate studies. The strategy followed in this thesis to extend the application range of a MeM into the LES regime has the advantage that handling of orography is usually already build into such models. For the chosen model METRAS simulating the flow over a mountain ridge, and comparing model results with an analytical solution (Lilly and Klemp 1979), is a standard test (e.g. Schlünzen 1996, p. 63 – 68) frequently applied. Simulations of flow over steep terrain with METRAS have been analyzed by Niemeier and Schlünzen (1993).

In the model, orography is accounted for by transforming the model equations (Section 3.1.1) in a terrain following coordinate system (Gal-Chen and Somerville 1975; Schlünzen 1988, p. 104ff.). This coordinate system uses a vertical coordinate defined as

$$\eta = z_t \frac{z - z_s(x, y)}{z_t - z_s(x, y)} \tag{4.7}$$

During the initialization phase, the model starts from flat terrain and slowly increases the terrain to the final values via diastrophism (Schlünzen et al. 2012a, p. 65).

Figure 4-2 illustrates the vertical coordinates and shows that the deviation from the Cartesian system is largest at the surface height z_s and disappears at the model top z_t. Please note that the example shown in Figure 4-2 is selected from a mountainous

region to allow better visualization. Especially the ratio z_t / max(z_s) = 10.5 has a much larger value than in the inner city model domain of Hamburg, where the ratio z_t / max(z_s) is only 0.0035.
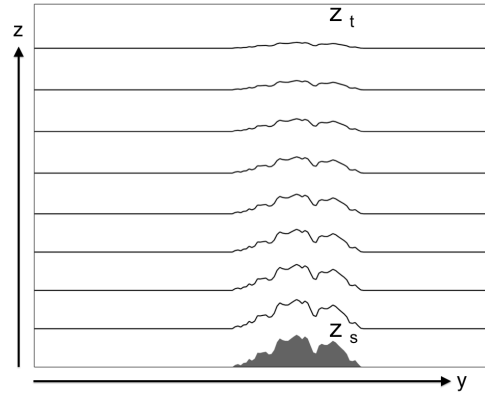

Figure 4-2: Selected model levels of the terrain following coordinates used in METRAS. Note, the axis are scaled differently and the vertical grid stretching is not shown. For demonstration reasons this example is taken from a METRAS orography created by Gierisch et al. (2013) showing a mountainous region (South-North cross section of Spitsbergen / Olav V Land).

The orography used for the model region is taken from the digital elevation model derived from the Shuttle Radar Topography Mission (SRTM) (Farr et al. 2007) and is shown in Figure 4-3.
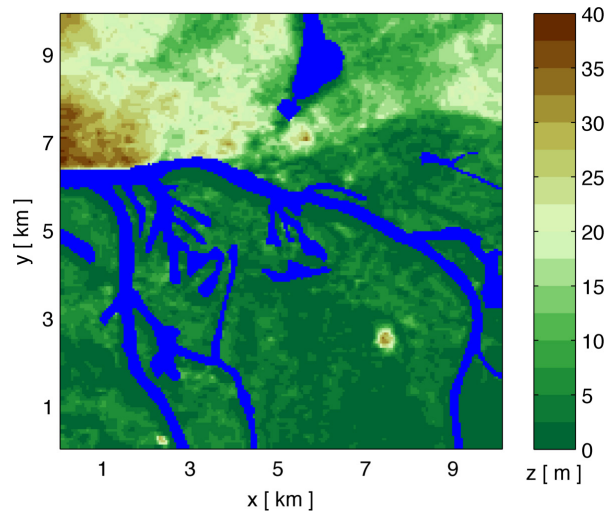
Figure 4-3: Orography in the model domain on a 50 m horizontal grid. Water grid cells, defined as those grid cells characterized by a water cover of at least 50 %, are drawn in blue regardless of their height above sea level.

The model domain (Figure 4-1, Figure 4-3) has a horizontal extension of 10 x 10 km^2 with a horizontal grid spacing of $\Delta x = \Delta y = 50$ m. The vertical grid spacing is $\Delta z = 20$ m up to an altitude of 1.450 m. Above this altitude vertical grid stretching has been used with the same stretching parameters as used in the simulation CBL_036 (Table 3-4). The model top z_t is at 11.196 m. Compared to the simulations in Chapter 3, further differences of the vertical grid are caused by the included orography, i.e. due to $z_s(x,y) \neq 0$ in Equation (4.7).

4.2 CBL above an urban area

4.2.1 Model setup for selected case study

The simulated situation represents an idealized clear sky summer day, without any large scale wind forcing. Thus, it represents one possibility for an autochthonous weather situation, which is of special relevance for the urban climate (VDI 1997) and, therefore, commonly investigated in urban climate assessments performed by environmental consultants (e.g. Funk et al. 2012).

Starting from a resting, stably stratified atmosphere the development of a convective boundary layer is simulated with METRAS-LES, using Equation (4.2) to calculate the surface temperature used to determine the energy fluxes at the surface. For comparability with the experiments discussed in Section 3 these simulations are also performed without considering moisture. The initial profile is calculated with the one-dimensional model METRAS-1D (Schlünzen et al. 2012a, p. 63 – 65) using an initial surface pressure p_{sfc} = 1013.06 hPa, an initial potential temperature at the surface θ_{sfc} = 290.15 K and an initial potential temperature gradient Γ = −0.003 K m^{-1}, as in the simulations discussed in Sections 3.2 – 3.3. The initial profiles are calculated for zero background wind. For numerical reasons METRAS-1D uses a minimum wind speed of 0.1 m s^{-1} in the calculation of the friction velocity according to Equation (3.32). The final wind speed calculated at the end of the one-dimensional initialization run is 0.00004 m s^{-1} at the height z_p of the lowest model level and even lower above. This is an appropriate approximation for the intended zero wind conditions. The balanced profiles of the one-dimensional model are used as start values for the three-dimensional simulations.

The undisturbed surface map (Figure 4-1 (a)) is used with the physical surface parameters according Table 4-1 and the orography shown in Figure 4-3. The model does not include detailed thermodynamics for the upper water layers of lakes or rivers. Instead the temperature of the water bodies are set to a constant value of 290.16 K throughout the whole simulation. This water temperature T_{water} is climatologically representative for May and September (Figure C-1). A diurnal cycle of the water temperatures is neglected, because the average diurnal cycle of water temperatures is only a few tenth of a Kelvin (Figure C-2). The soil temperature T_{soil} has been set to the water temperature. Thus any differences in temperatures between land and water are caused by a changing surface temperature (Equation (4.2)) over the land due to radiative forcing and resulting heat fluxes.

The simulation with these specifications is named HH_CORINE in the following. It is used to check the ability of METRAS-LES to simulate a CBL with the surface energy balance based calculation of surface fluxes using an urban like surface map with modest, but non flat, terrain. This prove of concept simulation, presented in Section 4.2.2 and 4.2.3, is additionally used to demonstrate some characteristic atmospheric features found for free CBL simulations for the investigated model region. HH_CORINE serves as reference simulation for the sensitivity studies following in Section 4.3.

4.2.2 Temporal development of characteristic heights

It is common in boundary layer meteorology to visualize the time development of convective boundary layers by graphs showing time vs. height of the entrainment zone (e.g. Stull 1988, Figure 1.7). Thus, as an intuitive introduction to the temporal development of the simulation HH_CORINE, time series of the characteristic heights $z_i(\text{HF})$, $z_{\max(\sigma_w^2)}$, $z_i(\text{Ri})$ and $z_{\max(\sigma_\theta^2)}$ have been analyzed (Figure 4-4). Using theses derived quantities, introduced in Section 3.3, summarizes the model state over all grid cells. Example profiles, which explain the physical meaning of the characteristic heights, are given in Figure 3-8 (b) for $z_i(\text{Ri})$, in Figure 3-10 (a) for $z_i(\text{HF})$ and in Figure 3-9 for the positions of the variance maxima $z_{\max(\sigma_w^2)}$ and $z_{\max(\sigma_\theta^2)}$.

The characteristic heights have been derived from profiles calculated from instantaneous model variables written at all model levels every 10 minutes. This 10 minute output interval has been chosen to keep the involved data volume manageable. The characteristic heights might fluctuate in time, as they are from instantaneous model results, which are not temporally averaged. The profiles, represented by the characteristic heights, are calculated based on spatial averages on model levels, i.e. on heights with constant η according Equation (4.7). This geometric choice necessarily influences the results of the analysis. One alternative would be the interpolation to constant heights above sea level. This method would be computationally more expensive and it is not clear if it would be beneficial here, as the physical influence of the surface may be better understandable at model levels, which take the distance to the surface into account. Furthermore the differences should be relative small due to the moderate terrain (Figure 4-3). Thus, the simpler approach, i.e. calculating the profiles on model levels, is chosen here.
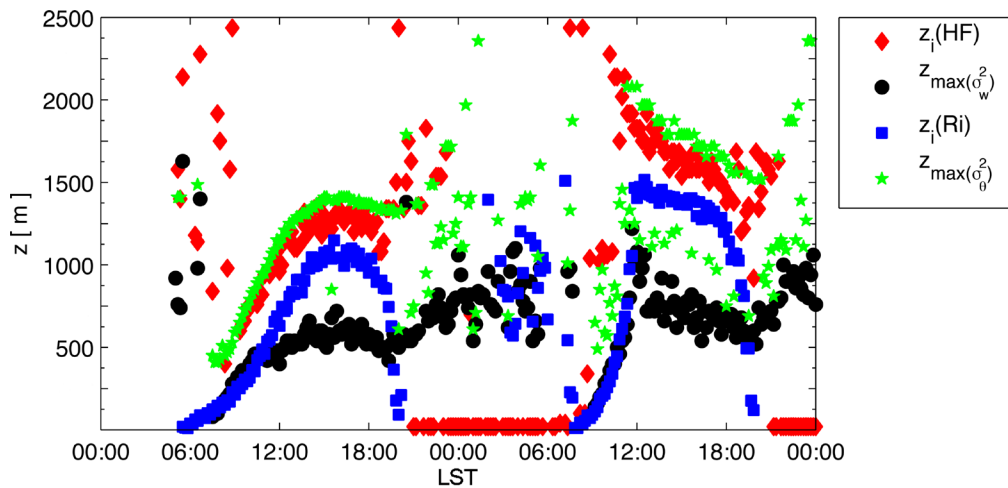

Figure 4-4: Diurnal cycle of characteristic heights (same as in Figure 3-16) for the simulation HH_CORINE using the map / model domain shown in Figure 4-1 (a).

A clear diurnal cycle can be seen in all four characteristic heights (Figure 4-4). The development in the morning of the first simulation day, which is initialized with horizontal homogeneous atmospheric conditions, shows similarities to the boundary layer growth in the experiments with forced heat fluxes (Figure 3-16). During the night

convection breaks down, which results in low values for z_i(HF) and in a large scatter for the other characteristic heights. The second day is characterized by a more rapid development of the convective regime, with some overshooting of the entrainment height, characterized by z_i(HF). This can be explained with a well-mixed residual layer remaining from the previous day, which favors the development of higher convection.

The observed diurnal cycle is a direct consequence of the warming of the surface during the day and can be seen as an first proof that simulations of CBL with METRAS-LES can not only be forced by directly prescribing heat fluxes (Section 3.1.4) but also by calculation of a surface temperature based on the surface energy balance scheme (Section 4.1.2).

Additionally, Figure 4-4 provides insight into the different characteristic heights as measure themselves: The height of maximum potential temperature variance, $z_{\max(\sigma_\theta^2)}$, is the least fluctuating characteristic height during the first day, but it shows largest scatter during the night. Compared to z_i(HF), $z_{\max(\sigma_\theta^2)}$ appears to be a less reliable measure of the height of the convective boundary layer as can be seen from its two fluctuating maxima during the second day. A relative smooth behavior is seen for z_i(Ri), which might be explained by the fact that it includes vertical gradients and thus more data than the other characteristic heights. The height of the maximum vertical wind speed variance, $z_{\max(\sigma_w^2)}$ does not fall to lower levels during the night. z_i(HF) clearly distinguishes between day and night, which makes it relative intuitive. Therefore z_i(HF) may be favorable over z_i(Ri) and $z_{\max(\sigma_\theta^2)}$ and is therefore chosen together with $z_{\max(\sigma_w^2)}$ for further model analysis in the remainder of this text.

4.2.3   Spatial features in a CBL above Hamburg

In contrast to the simulations with prescribed homogeneous heat fluxes in Chapter 3, the simulation HH_CORINE is performed over a somehow heterogenic surface. The two rivers Elbe and Alster cross the model domain causing a land water contrast. Other spatial differences in surface cover like between build up and vegetated area exist as well. These spatial variations of the surface cover and the orography may influence the simulated atmosphere due to different heat and momentum fluxes. Therefore, the introductive analysis of the simulation HH_CORINE is extended from the time development of characteristic heights (Section 4.2.2) to a more spatial orientated view. This allows to check the physical plausibility of model results further and to investigate how main topographic features influence the spatial structure of the simulated convective boundary layer above the inner city and harbor area of Hamburg.

Figure 4-5 (a) shows the instantaneous real temperature at 10 m above ground level at 12:00 LST of the first simulation day. For this time the average 10 m air temperature above all land grid cells is 0.71 K higher than the average 10 m air temperature over all water grid cells. Here, and in the rest of this thesis, water (land) grid cells are defined as grid cells which have at least 50 % SGS water (land) coverage. The average height above sea level of the land grid cells is 5.2 m higher than the average height of the

water grid cells. Following the dry adiabatic lapse rate $g / c_p \approx 0.0098\,\text{K m}^{-1}$ (e.g. Bohren and Albrecht 1998, p. 108 – 109) one would expect 0.05 K lower temperature over the land cells of the model domain. The simulated higher air temperature over land are an effect of heating the land surface by the solar radiation and provide an example how the surface scheme influences the atmospheric model results.

As spatial temperature difference between land and water covered areas causes thermal driven circulations (e.g. Fock and Schlünzen 2012; Pielke 2003) and METRAS is able to simulate sea breeze circulations (Schlünzen 1990) one can expect the existence of river breeze circulations in the model results. In fact the streamlines (Figure 4-5 (a)) and wind vectors (Figure 4-5 (b)) mainly indicate onshore wind, approximately perpendicular to the riversides. The divergence of the horizontal components of the wind field, analyzed for an altitude of 10 m above ground level in Figure 4-5 (b), reveal a divergent wind field over the Alster and parts of the Elbe. This also suggests that a river breeze effect likely exists in the modeled atmosphere.
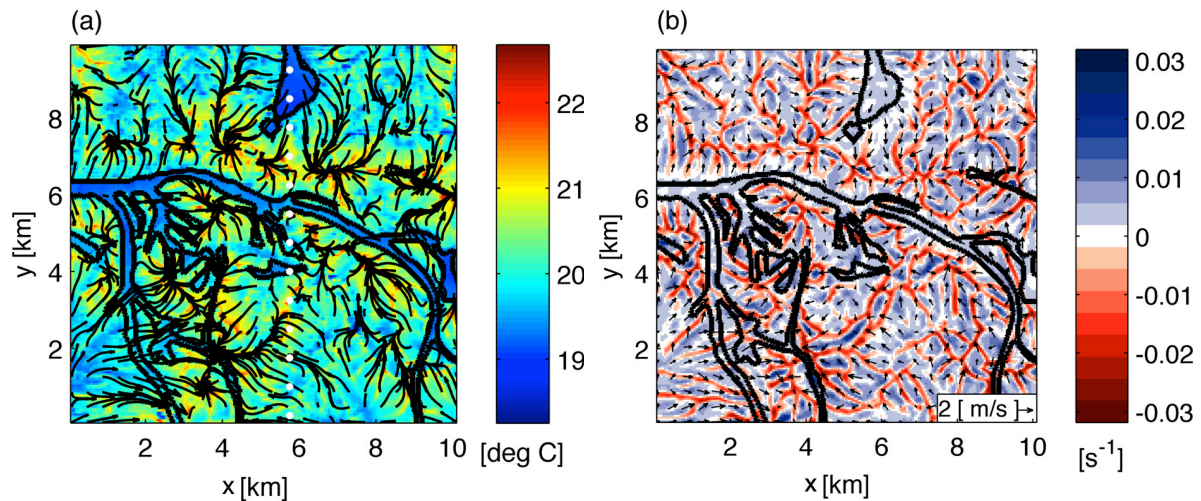

Figure 4-5: Horizontal cross section at 10 m above ground level, taken from instantaneous model output at 12:00 LST of an idealized convective day above Hamburg. Real temperature and curved stream lines are shown in (a), the divergence of the horizontal wind field and wind vectors in (b). The dotted line in (a) marks the position of the South North cross section shown in Figure 4-6.

In addition to the offset in average temperature between land and water, spatial structures are visible in the temperature field, which are caused by convective flow pattern, e.g. hot spots of warmer air occur at locations where the streamlines converge (Figure 4-5 (a)). The maximum 10 m temperature is 2.4 K above the mean 10 m temperature over land for the temperature field shown Figure 4-5 (a). The actual positions of the warmer grid cells vary in time due to the stochastic nature of the LES results (not shown here). Cellular structures, which indicate convective motion, are visible in the divergence of the horizontal wind field over land (Figure 4-5 (b)).

Cross sections of real temperature for lowest 600 m are shown in Figure 4-6 for different times of the first simulated day. The position of this south (left) – north (right) cross section is marked in Figure 4-5 (a). At 6:00 LST only little spatial differences are visible (Figure 4-6 (a)), indicating that convection has not started.

For later output times an increase in temperature and occurring horizontal inhomogeneities can be found in the model results (Figure 4-6 (b) – (d)). The relative narrow vertical structures characterized with higher temperature than the surroundings are related with updrafts, which mix air warmed at the surface to higher elevations. Above the water bodies, like the dammed Außenalster, warming of the air is reduced during the day, which explains the lower near surface temperatures in the northern part of the cross section shown in Figure 4-6 (c) – (d). Besides influences of the surface cover on the temperatures are also influenced by the orography. For example due to different surface elevation heating takes place at different heights (Figure 4-6 (b)).
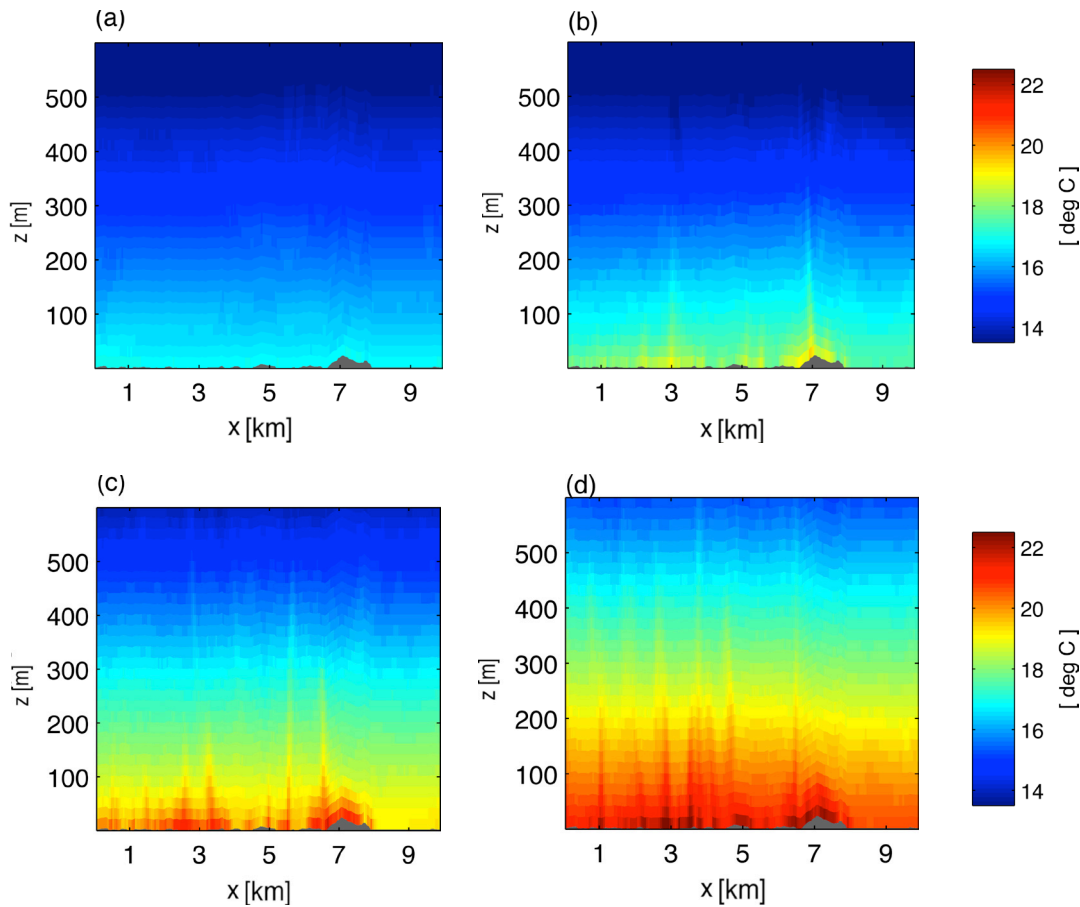
Figure 4-6: Instantaneous values of real temperature at 6:00 LST (a), 9:00 LST (b), 12:00 LST (c) and 15:00 LST (d) for the first simulation day of simulation HH_CORINE. Only the lowest 600 m are shown. The x-z cross sections are taken in south north direction along the dotted line drawn in Figure 4-5 (a).

The analysis of single output time steps and physical reasoning suggest that a river breeze circulation may exist in the model results in addition to the convective flow pattern. To prove this hypothesis and to characterize the mean state of the spatial circulation pattern occurring in the model domain, averaged divergences of the horizontal wind fields are analyzed for 10 m, 100 m and 750 m above ground level (Figure 4-7). The averages have been taken arithmetically over all available model output written between 9:00 LST and 18:00 LST from both simulation days. A regular output frequency of 10 min has been used for this analysis. To show more details, the

750 m level is shown with two different color axes (Figure 4-7 (c) – (d)). This analysis reveal the existence of a near surface convergence zone, which forms between river Elbe and water areas of the dammed Alster in the model results. This feature can also be seen from instantaneous horizontal cross sections (Figure 4-5), but become clearer in averaged analysis. The reason are merging river breeze fronts of Elbe and Alster over the inner city, which are connected with sinking motion and divergent wind fields over the water bodies. The convergence happens at lower altitudes. In the rising air above the near surface convergence the average horizontal flow field is already divergent at 750 m (Figure 4-7 (d)).
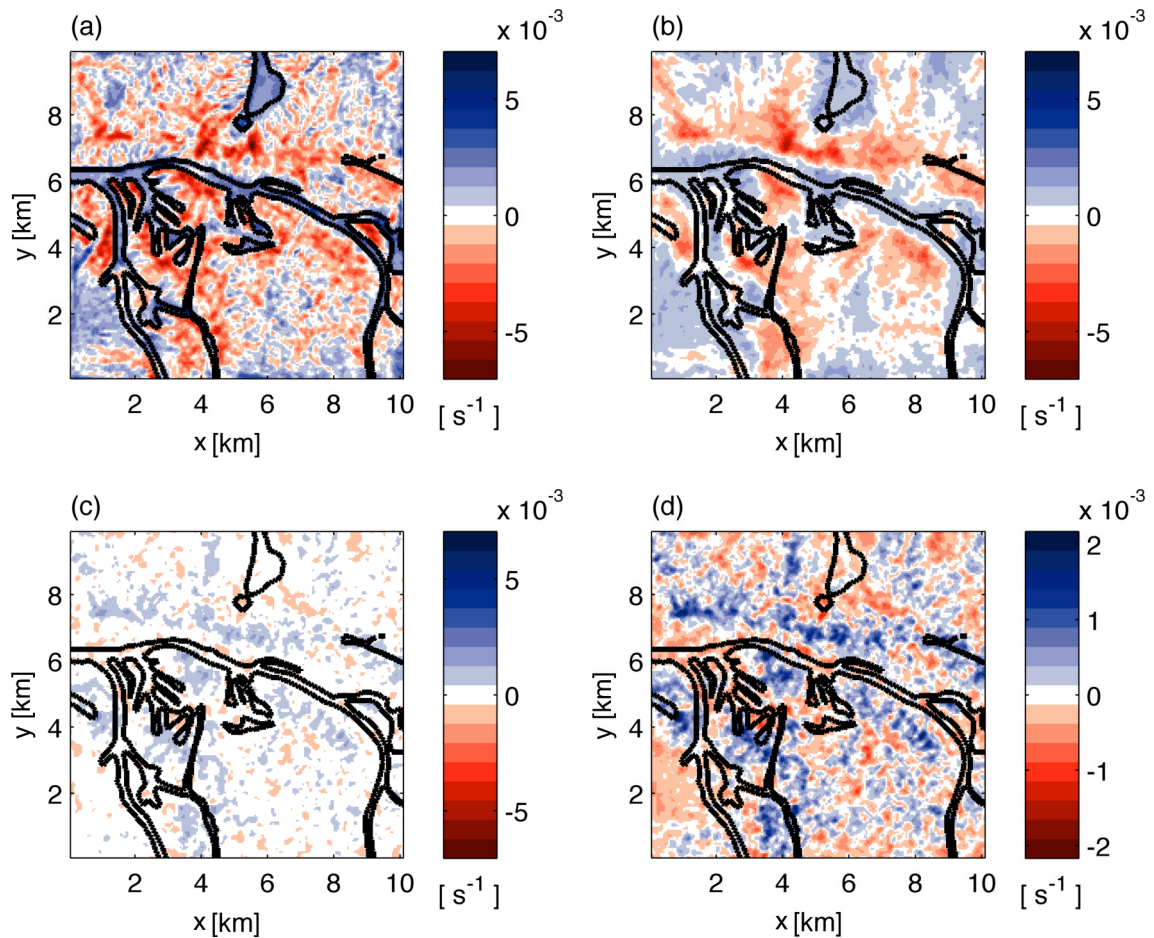
Figure 4-7: Divergence of horizontal wind field at 10 m (a), 100 m (b) and 750 (c,d) above ground level. Arithmetic average from 10 min model output of simulation from 9:00-18:00 LST of both simulation days of HH_CORINE.

The simulations suggest that thermal driven river breeze circulations likely have an influence on the atmospheric state in the inner city of Hamburg under fair weather low wind conditions, which otherwise support development of a convective boundary layer during the day. This may influence temperature, humidity and air pollution by horizontal transport directly, but may also create an indirect effect via the thermally caused ventilation. A quantification should not be taken from the analysis presented here, due to the simplified model setup. Influences of river breezes on flow pattern above urban areas are also known for other cities (e.g. Ryu and Baik 2013). An

additional analysis of the influence of Elbe and Alster on the atmosphere under convective conditions is presented in Chapter 5.

4.3 Variation of simulation techniques

4.3.1 Sensitivity on small scale surface class variations

Characteristic features of the simulated atmosphere are triggered by the underlying surface cover (Section 4.2.3), but the land use data available in CORINE are not detailed enough, to provide a realistic surface heterogeneity at the used horizontal grid size of 50 m (Figure 4-1 (a), Section 5.1). Nevertheless, this idealized setup allows to test the model response on additional surface cover heterogeneity at grid scale: In a sensitivity experiment the reference simulation (HH_CORINE, —) is repeated with the surface class disturbances (HH_NOISE, —), shown in Figure 4-1 (b). In the disturbed map 10 % of the land grid cells have been modified randomly, by replacing the occurring surface classes with other classes, which seem reasonable for the different city quarters. All other model input, including the initial profiles, is the same in both simulations.

Instantaneous horizontal cross sections of potential temperature are shown in Figure 4-8, taken at 15:00 LST of the first simulation day in both experiments. Selected heights are 10 m (Figure 4-8, top), 100 m (Figure 4-8, center) and 1000 m (Figure 4-8, bottom) above ground level. The spatial structures are similar in HH_CORINE (Figure 4-8, right) and HH_NOISE (Figure 4-8, left). Both simulations show reduced convection above the water bodies and the largest positive temperature fluctuations above the inner city, which is due to the thermal and roughness properties of the occurring surface classes (Figure 4-1, Table 4-1). In both setups the influence of the ground decreases with height, apparently at similar rates. In 1000 m above ground level a direct influence of the surface on the potential temperature is hardly recognizable (Figure 4-8, (e) – (f)).

The time development of the characteristic heights $z_i(\mathrm{HF})$ and $z_{\max(\sigma_w^2)}$ is very similar for the simulations HH_CORINE and HH_NOISE during the first day, but shows some more active development for HH_NOISE during the second day (Figure 4-9). Even though it seems plausible that additional surface heterogeneity may trigger more atmospheric mixing, this cannot concluded certainly from this analysis. Some model instabilities occurs during the night as the model has difficulties in handling the occurring stable stratifications in LES mode. Therefore the "initial conditions" after the less reliable simulated night may show larger differences between the simulations HH_CORNE and HH_NOISE. Thus the results for the second day are more uncertain than those for the first day. Furthermore the surface changes have not made in a surface fraction conserving way. This means, the total energy conversion by surface cooling or heating might be slightly different between the two simulations. Hypothetical the similarity of the time development might be more similar for the second day, if this surface modifications would have been made in an energy

conserving way. But surface cover conserving topography experiments following in Chapter 5, do not support this hypothesis.
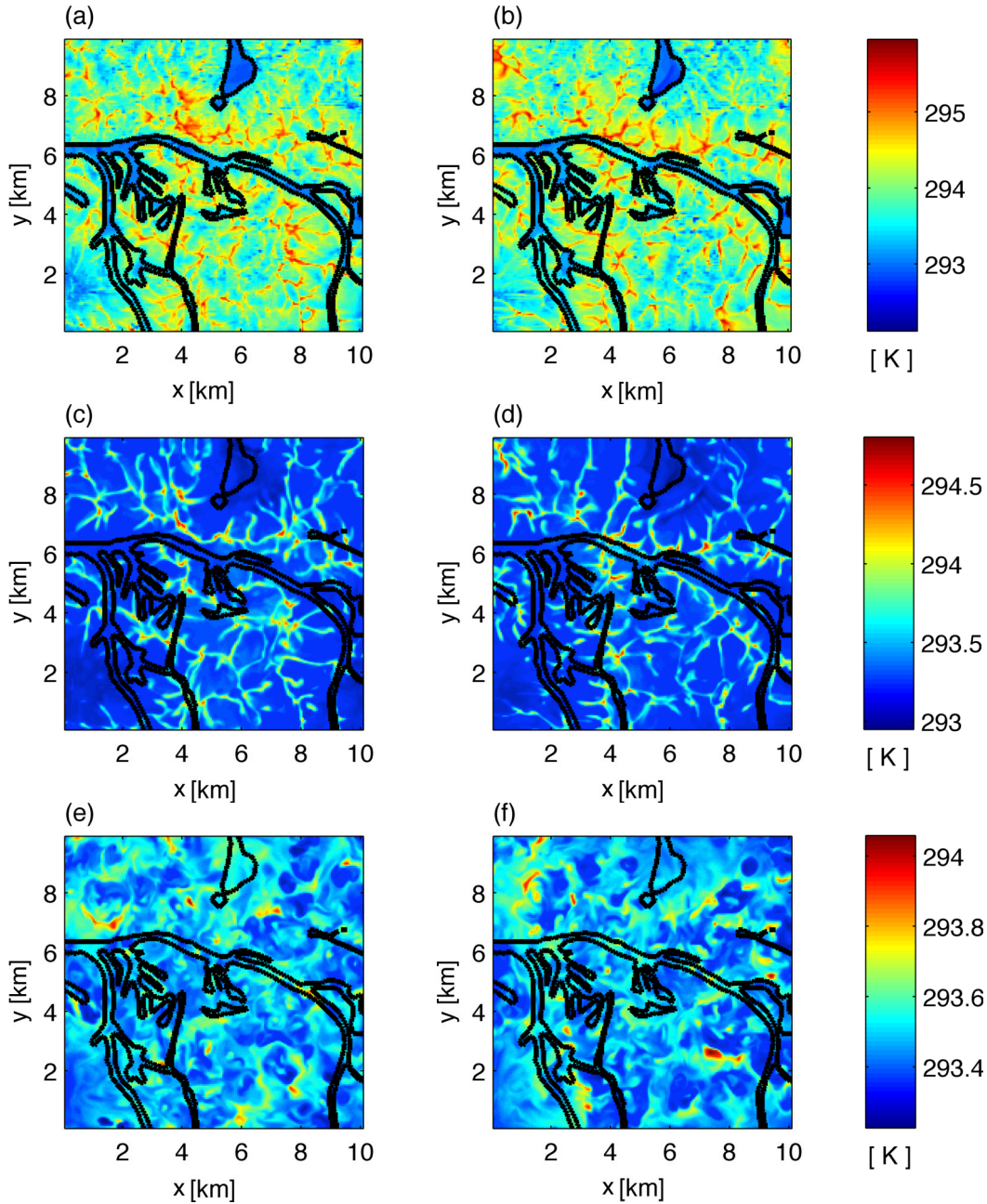

Figure 4-8: Potential temperature at 10 m (a,b), 100 m (c,d) and 1000 m (e,f) above ground level taken at 15:00 LST of the first simulation day from the simulation HH_NOISE (a,c,e) and HH_CORINE (b,d,f).

Besides the structural and temporal similarity of the two simulations, it is clear, that they represent different solutions in the sense of independent members of an ensemble. Thus modification of 10 % of the surface classes at randomly chosen grid cells is a sufficient method to create an independent ensemble member. Such a modification seems not very large compared with the uncertainties, which occurs in the surface data anyway. Typical error sources are limited details of the data sets (Figure 4-1), combination in groups of land use / surface cover classes (Appendix D.1) and rastering to the computational grid. Further uncertainties arise from assigning the

physical parameters (Table 4-1) to the individual classes and the applied physical model (Section 4.1.2). Hence, land use driven ensembles, implemented by disturbed maps, seem to be a reasonable approach to deal with the stochastic nature of LES results in (urban) modelling. The capability of defining surface cover based ensembles could be particular important for the simulation of non-stationary situations, as for these situations statistical converging results are not obtainable by expansion of the simulation length.
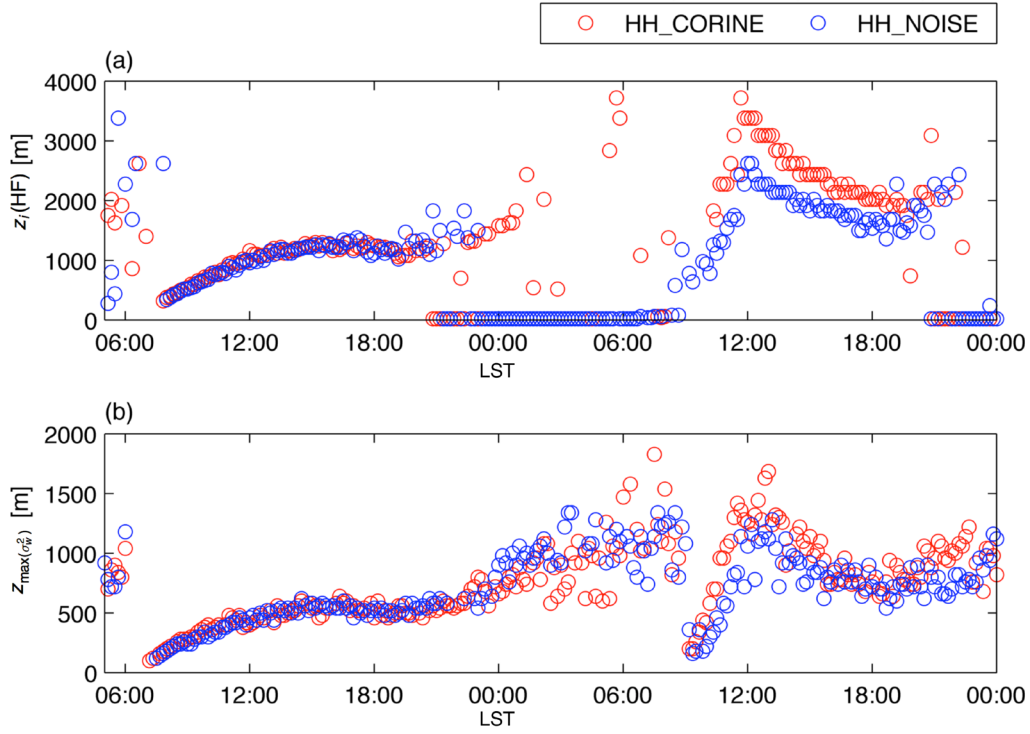

Figure 4-9: Development of the characteristic heights z_i(HF) (a) and $z_{\max(\sigma_w^2)}$ (b) as simulated in the experiments HH_CORINE (red) and HH_NOSIE (blue).

4.3.2 Sensitivity on surface layer TKE parameterization

The investigated situations are mainly controlled by the processes occurring near the surface. Therefore model assumptions and constants used to describe physical processes in the surface layer influence the model results. In the following they should be analyzed for the influence of the near surface parameterization of the subgrid scale turbulent kinetic energy. In the lowest atmospheric layer subgrid scale turbulent kinetic energy is parameterized with

$$\overline{e} = \left(\frac{u_*}{c}\right)^2 \tag{4.8}$$

Equation (4.8) has been derived for the neutral Prandtl layer (Detering 1985, p. 25) in the context of a RANS turbulence closure. The same or similar equations have been used by Raasch (1988, p. 35), Lenderink and Holtslag (2004) and Gross (2010) to set the subgrid scale TKE. The value of c in the surface layer TKE parameterization is derived from measured or simulated data. METRAS-RANS uses $c = 0.5$, which is also

the number provided by Therry and Lacarrère (1983) based on measurement data. Lopez (2002) found an optimal value $c = 0.55$ for obstacle resolving simulations with MITRAS-RANS by comparison with wind tunnel data and cites values between 0.4 and 0.61 from literature. Detering (1985: 26-27) cites values between 0.27 and 0.61 depending on atmospheric stability, with the lowest values valid for unstable stratification. The LES model PALM (Raasch and Schröter, 2001), in the version used in the intercomparison study presented in Section 3.2.3, uses $c = 0.1$ but has a commented code line[9] to experiment with using $c = 0.4$.

Equation (4.8) is used in METRAS-RANS to guarantee a continuous matching for the fluxes calculated from the surface layer parameterization and those calculated with the Prandtl-Kolmogorov closure (Appendix B). The similarity between the RANS and the LES closure (Fock 2007) makes it apparent to try the same approach also for LES mode. Unfortunately, this is impossible which will be explained in the following, because this helps to understand the experimental setting of c. One might expect that trying to adjust the length scale Δ and adding other stability correction terms to the diffusion coefficients for the LES SGS model (Section 3.1.2) could allow to derive Equation (4.8) in analogy to what is done in Appendix B for the RANS closure. Taken this analogy further one might expect that the formulation of the exchanges coefficients (Equation (3.6)) would cause $c = c_k = 0.1$.

However, for LES mode the fundamental assumption (Equation (B.1) and Equation (B.13)) made for the flux matching is not suitable. The surface fluxes (right hand side of Equation (B.1) and (B.13)) should not balance with the subgrid scale fluxes (left hand side Equation (B.1) and (B.13)). Instead they should balance with the sum of the resolved fluxes plus the subgrid scale fluxes. This is a consequence of the concept of LES, which aims to simulate parts of the turbulent fluxes at resolved scales. Thus, sticking to the approach from Appendix B would require to include resolved fluxes on the left hand side of equation (B.1) and (B.13). Thus, for LES mode Equation (4.8) is empiric without proper closed theoretic foundation.

As in LES less energy should be contained in the SGS motions than in RANS (Figure 2-1), one could hardly argue that the SGS turbulent kinetic energy should be larger in METRAS-LES than in METRAS-RANS. Thus setting the variable c in METRAS-LES to values smaller than 0.5 (used in METRAS-RANS) seems to be wrong from the reasoning given above. It is not clear, which value for c should be used for METRAS-LES. To assess the sensitivity on the parameter c in Equation (4.8), the case HH_NOISE (Section 4.3.1) has been run with four different values for c (Table 4-2). Simulation results are provided in Figure 4-10, Figure 4-11 and Figure 4-12.

---

[9] In PALM Equation (4.8) is set in subroutine prandtl_fluxes.f90, in METRAS-LES in the subroutine se_sgsm_deardo.f90 and in METRAS-RANS in the subroutine se_tke_sink.f90.

Vertical cross sections of potential temperature deviations are shown in Figure 4-10. Largest differences are visible near the surface. The simulation HH_TKE_0.1 shows relatively homogeneous temperature fields. With increasing c, and thus decreasing turbulent kinetic energy smaller and warmer updrafts are visible.

Table 4-2: Parameters and names for sensitivity experiments on variations of c (Equation (4.8)) in surface layer TKE parameterization.

	HH_TKE_0.1	HH_TKE_0.3	HH_TKE_0.5	HH_TKE_1.0
c	0.1	0.3	0.5	1.0
$\overline{e}\,(z = z_p = 10\ \mathrm{m})$	$100 \cdot u_*^2$	$11.1 \cdot u_*^2$	$4 \cdot u_*^2$	$1 \cdot u_*^2$
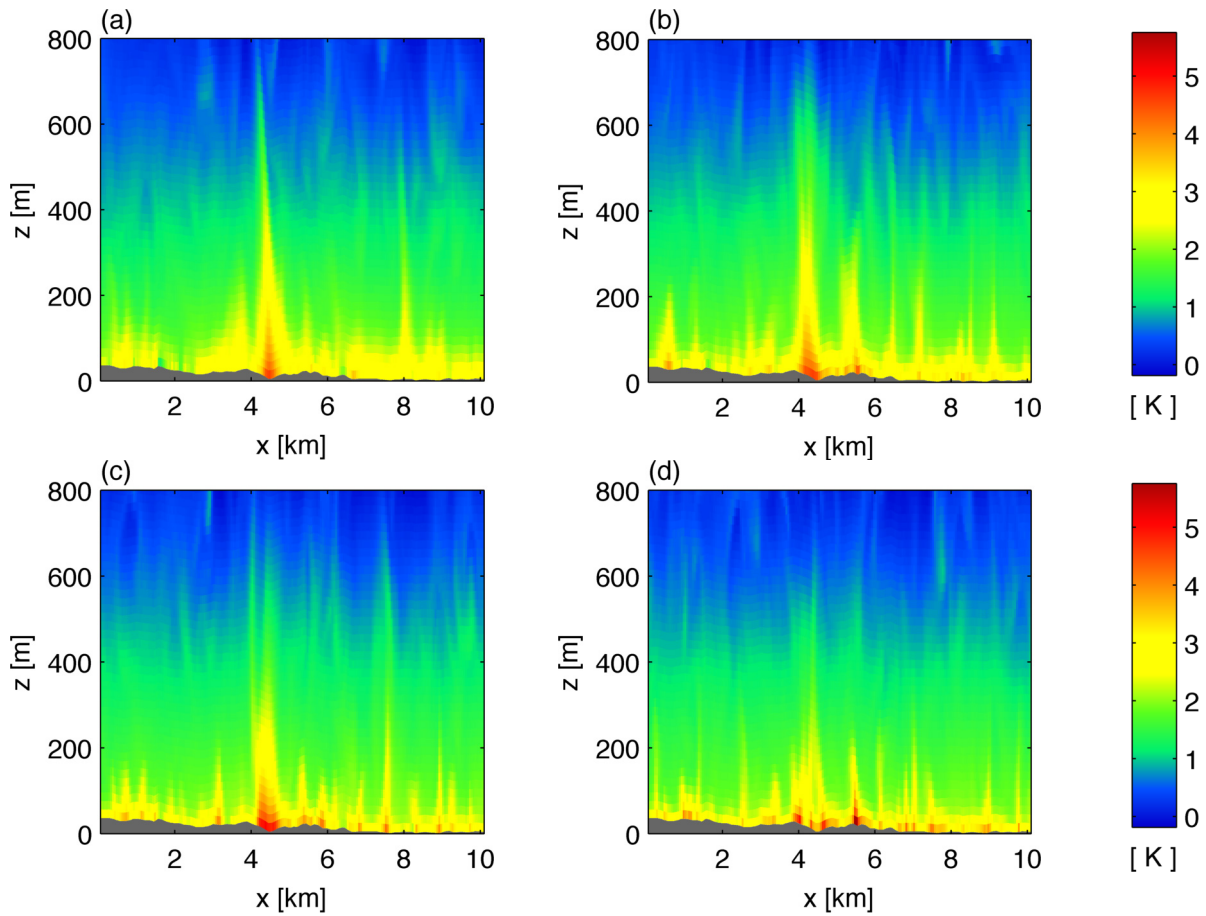
Figure 4-10: Vertical cross section of potential temperature deviation at $y = 7$ km and 11:00 LST for the experiments with (a) $c = 0.1$ (HH_TKE_0.1), (b) $c = 0.3$ (HH_TKE_0.3), (c) $c = 0.5$ (HH_TKE_0.5) and (d) $c = 1.0$ (HH_TKE_1.0). The position of the vertical cross section is marked by a black line in Figure 4-11.

To have a closer look into the effect near the surface, horizontal cross sections of real temperature at 10 m above ground are shown in Figure 4-11. The temperature field shows a notable response to the value for c used in Equation (4.8). In simulation HH_TKE_0.1 (Figure 4-11 (a)) the 10 m temperature is considerably influenced by surface cover and orography. For example, colder areas are visible over the landfill Georgswerder (position in Figure 4-11 (a): $x = 7.8$ km, $y = 3$ km). This hill has an altitude of 40 m and is the point of highest elevation in the model domain (Figure 4-3).

This and similar effects seem to decrease with increasing values for c (Figure 4-11 (b) – (d)). Instead stronger influence of convective flow structures occurs.
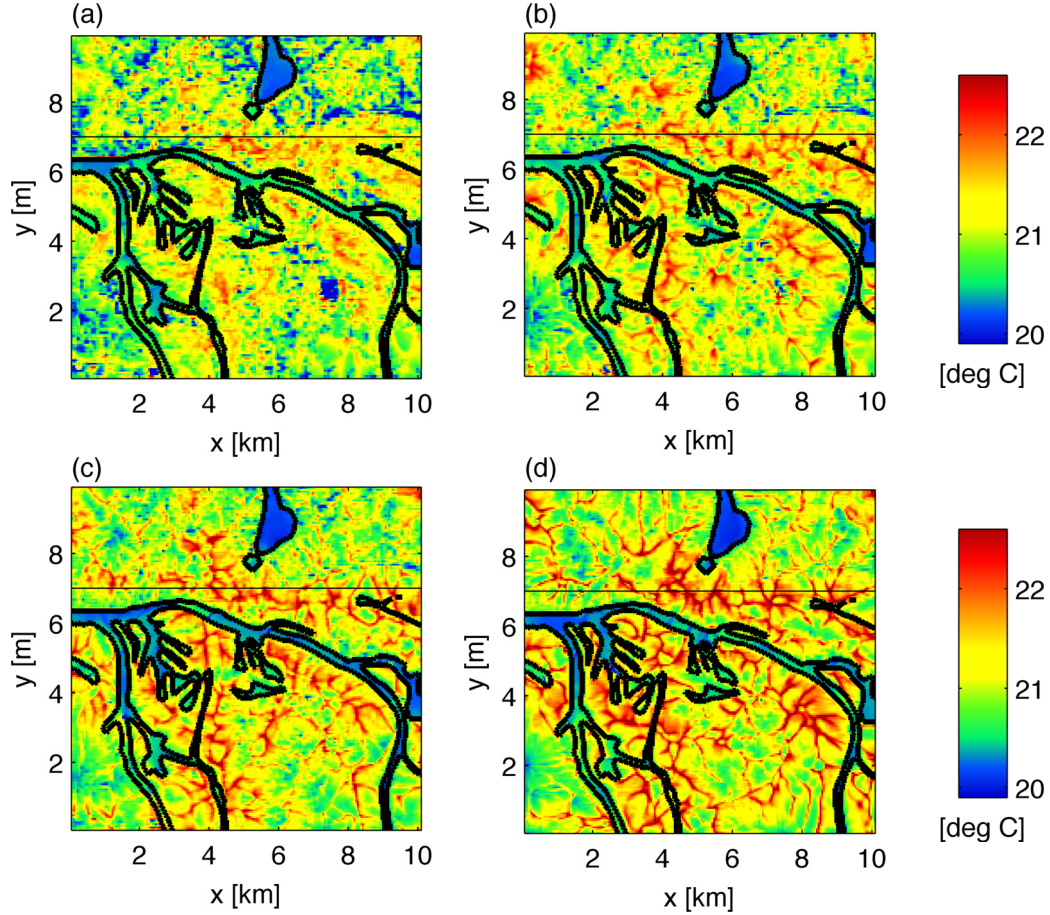

Figure 4-11: Real temperature at 10 m above ground (lowest model level) at 14:00 LST for the experiments with (a) c = 0.1 (HH_TKE_0.1), (b) c = 0.3 (HH_TKE_0.3), (c) c = 0.5 (HH_TKE_0.5) and (d) c = 1.0 (HH_TKE_1.0).

The observed behavior can be explained by the decrease of subgrid scale diffusion from case HH_TKE_0.1 (c = 0.1) to case HH_TKE_1.0 (c = 1.0). In simulation HH_TKE_0.1 resolved structures of the convective boundary layer are strongly suppressed near surface due to large diffusion coefficients.

As the SGS turbulent kinetic energy is also mixed to the model levels above the surface layer, the setting of c is not only important for the model results in the lowest model level. Figure 4-12 shows horizontal cross sections of real temperature at 100 m above sea level taken from instantaneous model output for 14:00 of the first simulated day. The simulated structures are more diffuse in case HH_TKE_0.1 than in case HH_TKE_0.5.

In summary this sensitivity study shows that the variable c needs to be suitably selected as the resulting SGS diffusivity influences the results of METRAS-LES considerably. Setting c to c_k = 0.1 is not desirable for METRAS-LES since it produces a too strong coupling to the surface, which was in parts demonstrated here. Furthermore it results in a quite diffusive model setup. In order to determine a more

optimal value comparisons with data from measurements or results from direct numerical simulation would be needed.
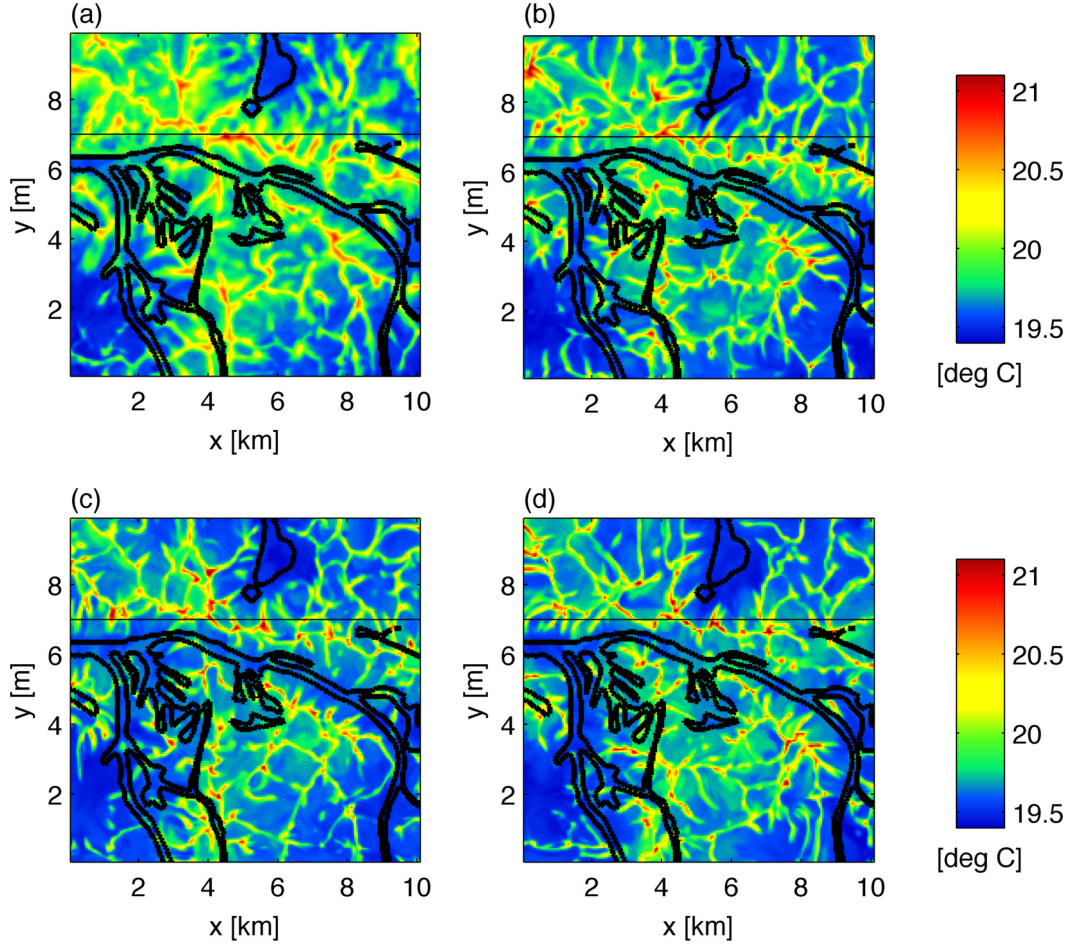

Figure 4-12: Horizontal cross sections in x-y direction of real temperature in 100 m above sea level for the experiments with (a) c = 0.1 (HH_TKE_0.1), (b) c = 0.3 (HH_TKE_0.3), (c) c = 0.5 (HH_TKE_0.5) and (d) c = 1.0 (HH_TKE_1.0). Linear interpolation has been applied to calculate the value at 100 m above sea level from model levels. Instantaneous values are shown for 14:00 LST of the first simulated day.

4.3.3   Sensitivity on subgrid scale model (LES / RANS)

As a further sensitivity study a variant of the simulation HH_NOISE has been repeated with three different model versions: METRAS-LES, METRAS-RANS (Schlünzen et al. 2012a) and METRAS-PCL (Schlünzen and Bigalke 2010), which is the M-SYS component deployed for environmental consulting. The aim of this model intercomparison is to investigate differences between the LES and RANS solutions for the simulation of a CBL above Hamburg. The simulation with METRAS-LES uses the SGS closure described in Section 3.1.2 (HH_LES, ▬). The simulation with METRAS-RANS (HH_RANS, ▬) uses the Prandtl-Kolmogorov closure (Schlünzen et al. 2012a, p. 26 – 27) but with switched off counter gradient term to allow larger similarity to the simulation with METRAS-LES. The simulation with METRAS-PCL (HH_PCL, ▬) uses a first order RANS turbulence closure, which includes a counter gradient term (Schlünzen and Bigalke 2010, p. 4). The simulation HH_PCL may be influenced by

additional model differences, as it is performed with METRAS-PCL, which is based on an older M-SYS model version.

The three models are compared regarding the spatial variability of real temperature at 10 m above ground level for the period from 7:10 LST until 12:10 LST for the first simulation day. The analysis is based on instantaneous model output. The output interval is 10 min for HH_LES and HH_RANS and 6 min for HH_PCL. For the analysis horizontal averages, taken over the complete model domain at 10 m above ground at each individual output time step, are subtracted from the values at each grid cell. This filters the diurnal cycle of the temperature. Frequency distributions are calculated from this filtered temperature fields using all available time steps (Figure 4-13 – Figure 4-15).
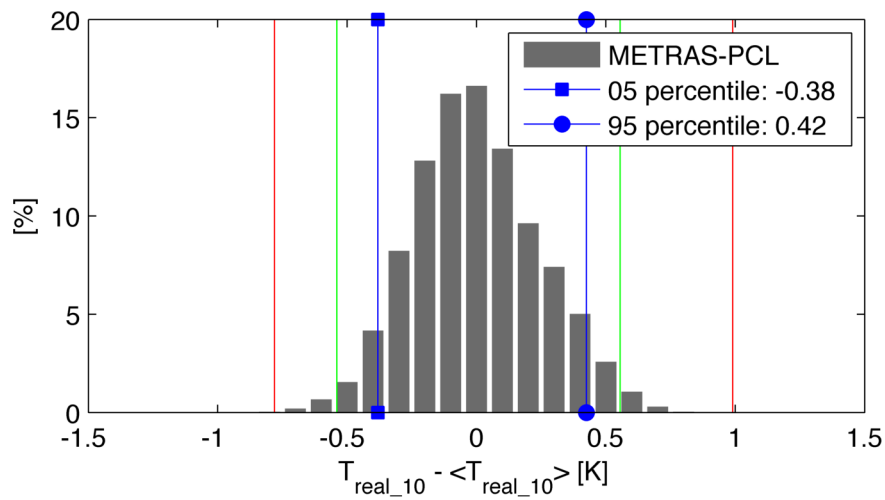

Figure 4-13: Deviation of 10 m real temperature from horizontal average calculated from 50 output times between 7:10 LST and 12:10 LST taken from the simulation HH_PCL. Percentiles of this distribution are marked in blue, percentiles from HH_RANS (Figure 4-14) in green and percentiles from HH_LES (Figure 4-15) in red.
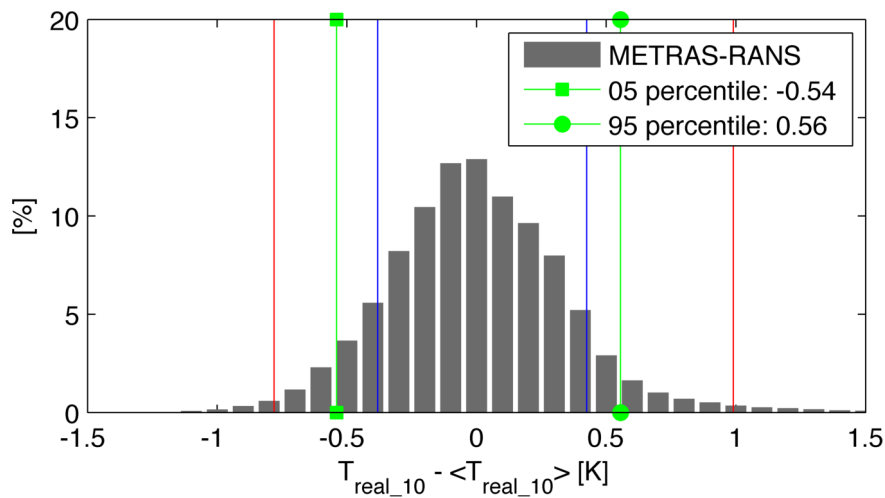

Figure 4-14: Deviation of 10 m real temperature from horizontal average calculated from 30 output times between 7:10 LST and 12:10 LST taken from the simulation HH_RANS. Percentiles of this distribution are marked in green, percentiles from HH_PCL (Figure 4-13) in blue and percentiles from HH_LES (Figure 4-15) in red.
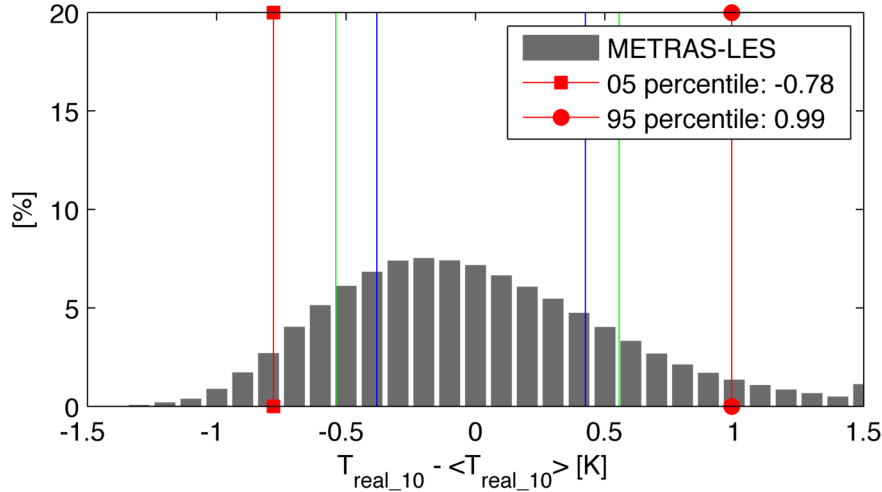
Figure 4-15: Deviation of 10 m real temperature from horizontal average calculated from 30 output times between 7:10 LST and 12:10 LST taken from the simulation HH_LES. Percentiles of this distribution are marked in red, percentiles from HH_PCL (Figure 4-13) in blue and percentiles from HH_RANS (Figure 4-14) in green.

The smallest temperature range is found in the distribution of the simulation HH-PCL (Figure 4-13). The difference between the 5 and the 95 percentile is only 0.8 K. For the simulation HH-RANS (Figure 4-14) a wider distribution is found. Here the difference between the 5 and the 95 percentile is 1.1 K. For the simulation HH_LES (Figure 4-15) the widest distribution is found with 1.77 K difference between the 5 and the 95 percentile. Thus in this analysis the spatial temperature range provided by METRAS-LES is more than twice as large as the one simulated by METRAS-PCL. The distribution for HH_LES is skewed to the right, because near surface warmer air concentrates in relative small updrafts (e.g. Figure 4-8 (a)) and the sinking of cooler air happens more smoothly in the centers of convective cells and over water.

4.4 Conclusions

This chapter proves that the application range from METRAS-LES can be extended from the simulation of developing CBL above flat, homogeneous and constantly heated surfaces (Chapter 3) to the simulation of complete diurnal cycles of free convective situations above heterogeneous surfaces heated by the time and location dependent incoming solar radiation (Section 4.2.2).

Simulating of a second day is possible, even though the model results for the night are not completely reliable, because the LES approach breaks down with the used resolution for stable stratification. This limitation may decrease the comparability of simulation results for the second simulation day. Therefore, most model analysis presented in this chapter concentrates on the time from 9:00 LST to 18:00 LST of the first simulation day.

In addition to proving that the usage of the thermodynamic surface scheme from METRAS-RANS (Section 4.1.2) allows successful simulations of time dependent CBL with METRAS-LES (Section 4.2.2 – Section 4.3.2), the presented simulations show that

inclusion of modest orography is possible in simulations performed with METRAS-LES (e.g. Figure 4-6).

For calculation of surface boundary values in simulations above a somehow heterogeneous area representing the city of Hamburg, CORINE land cover data have been mapped to surface classes (Section 4.1.3, Appendix D.1). Smaller modifications of surface cover seem to be a suitable trigger for ensemble simulations of CBL (Section 4.3.1). This is especially important, because limited knowledge about surface characteristics at grid scale allows a large degree of freedom in describing the surface. Thus, using surface cover driven ensembles seems to be an appropriate approach for urban climate modelling in general, not only for performing large eddy simulations above urban areas.

The parameterization of the subgrid-scale turbulent kinetic energy in the surface layer has an important contribution to the overall diffusivity of the model and thus on the resolved scales (Section 4.3.2). Conceptual differences between the LES to the RANS approach show that this parameterization can only be used in the RANS model to enforce continuous fluxes at the top of the surface layer (Section 4.3.2, Appendix B). Switching between the RANS and the LES approach demonstrates that LES increases the spread of simulation results (Section 4.3.3), which might be helpful for urban applications dealing with representativity or with the exceedance of short time extreme values.

Numerical studies of the diurnal cycle of a convective boundary layer were used to understand some characteristics of CBL above the inner city and the harbor area of Hamburg. Under calm wind conditions the development of CBL is supported by the model. Additional to the convective motions, already seen in the simulations of Chapter 3, the model simulations include river breeze circulations. The resulting atmospheric conditions include therefore combined influences of convection motions and river breeze circulations. A near surface flow convergence occurring between the Elbe River and the artificial lake Außenalster is found in model results, averaged from 9:00 LST to 18:00 LST (Section 4.2.3). The river breeze influence might be important for flow and temperature structures under free convective conditions and therefore most likely contribute to the local climate of the city of Hamburg.

For interpretation of the results of this Chapter it should also be noted, that the simulations are still quite idealized. For example moisture is still neglected, which influences the buoyancy and the energy exchanges at the surface. The used CORINE land cover data does not provide a detailed map at 50 m resolution (Section 4.1.3). To check the importance of map details finer grained surface data have been used for model experiments in Chapter 5.

5   LES above a city with varied surface complexity

Chapter 4 showed diurnal cycles of CBLs above the city of Hamburg, simulated with METRAS-LES. The map used for these model experiments is very coarse and underestimates the surface heterogeneity.

The influence of the granularity of the used surface data on the simulation of convective situations above the inner-city and harbor of Hamburg is investigated in the following Chapter. This is intended to answer the question to what extent details of topographic data are relevant for simulations of convective boundaries above heterogeneous urban areas. The needed level of detail is discussed along the requirements to evaluate model simulations for urban applications. The performed model experiments are based on more detailed topography data (Section 5.1), which are artificially simplified (Section 5.2) to analyze the influence of surface heterogeneity and to continue the discussion of topographic influence on the atmosphere above the inner-city of Hamburg during convective conditions (Section 5.3).

5.1   Detailed topography data for Hamburg

5.1.1   Mapping of surface classes

Detailed surface classes for the Hamburg inner-city and harbor region have been derived from the ATKIS Basis-DLM (AdV 2009a). The shapes in the original ATKIS data set are overlapping and thus non-exclusive for certain areas. To exploit the full heterogeneity of these data, some reordering was needed to get the smallest shapes in the foreground. The reordered data have been rastered to a 12.5 m grid, which served as input for the derivation of surface classes at the model resolution of 50 m. Hence, 16 raster cells could be used to calculate the SGS distribution of surface classes within one model grid cell.

As for the CORINE data (Section 4.1.3), a remapping from the land use oriented ATKIS classification to 10 physical meaningful surface classes was needed. A tabular description of the original ATKIS classes has been compiled by Kirschner (2009), based on the official data documentation (AdV 2003). Both, description and documentation, are not always intuitive in the terms of physical processes like heat or momentum fluxes, acting at the land air interface. Therefore samples of all occurring classes have been checked against satellite pictures in the visible spectral range to perform an expert judgment for the physical classification. Figure 5-1 shows the main surface classes resulting from the newly defined mapping. The detailed mapping is provided in Appendix D.2 and is called METRAS_URBAN_A in the following. Table 5-1 contains the surface characteristics for the METRAS_URBAN_A classes. Compared to the surface classes in the METRAS_URBAN mapping (Table 4-1), the METRAS_URBAN_A mapping results in one additional urban class and drops one vegetation class for that, i.e. it includes the class suburban but not the class mixed

forest. The mapping METRAS_URBAN_A is tailored for the ATKIS classes occurring in the inner-city of Hamburg. Mappings of ATKIS data for other model domains may need some adjustments.

Table 5-1: Physical surface characteristics for surface classes in METRAS_URBAN_A, like those given in Table 4-1 for the METRAS_URBAN classes .The mapping from the ATKIS classes towards the METRAS_URBAN_A classes is given in Appendix D.2.

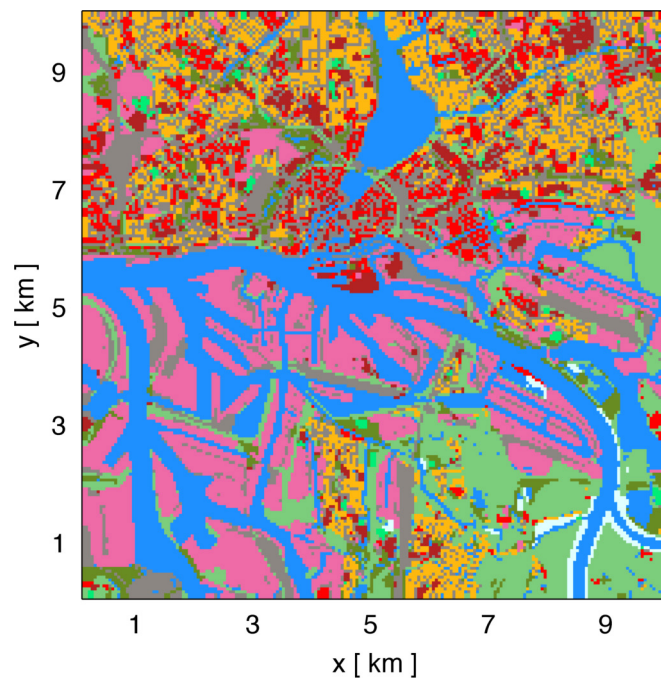| Surface classes for mapping METRAS_URBAN_A		A_0	k_s [m^2s^{-1}]	ν_s [$J\,K^{-1}s^{-1}m^{-1}$]	α [$m\,m^{-1}$]	W_k [m]	z_0 [m]
Water	0	f_1	1.5×10^{-7}	100	0.980	100.0	f_2
Mudflat	1	0.10	7.4×10^{-7}	2.20	0.980	0.322	0.100
Harbour & Industry	2	0.20	2.3×10^{-6}	4.60	0.050	0.081	0.600
Mixed Vegetation	3	0.20	5.2×10^{-7}	1.33	0.200	0.138	0.040
Meadows	4	0.20	5.2×10^{-7}	1.33	0.400	0.015	0.020
Traffic	5	0.12	2.3×10^{-6}	4.60	0.050	0.015	0.005
Bushes	6	0.20	5.2×10^{-7}	1.33	0.300	0.081	0.350
Sub Urban	7	0.15	1.0×10^{-6}	2.93	0.050	0.968	0.700
Urban	8	0.15	1.4×10^{-6}	4.60	0.050	0.484	1.400
Urban Compact	9	0.15	2.3×10^{-6}	4.60	0.025	0.300	2.000

Figure 5-1: Main surface classes in model domain on a 50 m horizontal grid. The surface classes are based on ATKIS data using the surface class mapping METRAS_URBAN_A (Appendix D.2). A color scale is provided together with the used physical surface characteristics in Table 5-1.

The mapping METRAS_URBAN_A assigns 91 ATKIS classes to 10 model classes, while the mapping METRAS_URBAN only assigns 42 CORINE classes to 10 model classes. The distribution of the SGS surface classes for the model domain is provided in Table 5-2:

58.8 % of the total model domain is covered by built-up areas (class: 2, 5, 7, 8 and 9), 21.4 % by water (class: 0) and 19.8 % by vegetation (class: 1, 3, 4 and 6).

Table 5-2: Distribution of subgrid scale surface classes (Table 5-1) in the model domain shown in Figure 5-1.

Class		O [%]	Class		O [%]
Water	0	21.4	Traffic	5	19.8
Mudflat	1	0.8	Bushes	6	4.5
Harbour & Industry	2	17.2	Sub Urban	7	11.2
Mixed Vegetation	3	13.7	Urban	8	5.8
Meadows	4	0.8	Urban Compact	9	4.8

The number of SGS surface classes per grid cell has been determined for the ATKIS based map (Figure 5-1) and the CORINE based map (Figure 4-1 (a)), to compare the granularity of these maps quantitatively. As expected, more SGS surface classes exist in the METRAS_URBAN_A map (Figure 5-2 (a)) than in the METRAS_URBAN map (Figure 5-2 (b)). More than 55 % of all grid cells in the METRAS_URBAN_A map have two or more surface classes, while more than 86 % of all grid cells of the METRAS_URBAN map have only one unique surface class (Table 5-3).
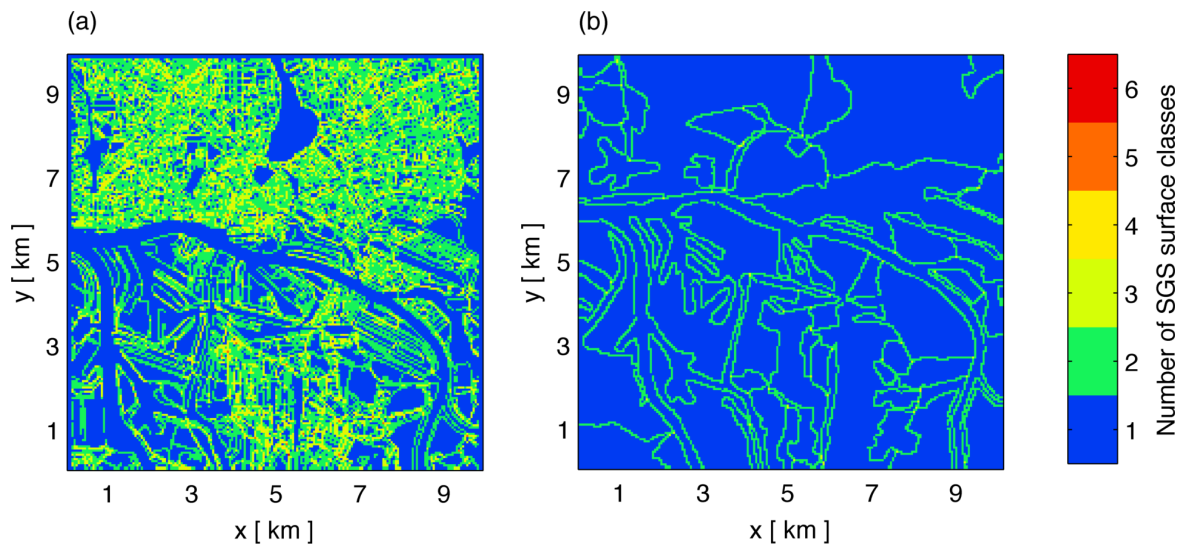

Figure 5-2: Map of number of subgrid scale surface classes for the map (Figure 5-1) based on ATKIS data / the mapping METRAS_URBAN_A (a) and for the map (Figure 4-1 (a)) based on CORINE data / the mapping METRAS_URBAN (b). The corresponding frequency distribution is given in Table 5-3.

Table 5-3: Frequency distribution of the number of subgrid scale surface classes per grid cell for the METRAS_URBAN_A (Figure 5-2 (a)) and METRAS_URBAN (Figure 5-2 (b)) maps.

map	1 surface class / cell	2 surface classes / cell	3 surface classes / cell	4 and more surface classes / cell
METRAS_URBAN_A	44.1 %	39.0 %	14.8 %	2.1 %
METRAS_URBAN	86.1 %	13.7 %	0.2 %	0.0 %

5.1.2 Correction of orography data

Orography data have been taken from the digital elevation model ATKIS DGM5 (AdV 2009b). These orography data are less noisy than the SRTM data used for the simulations discussed in Chapter 4. They are used here for a better representation of the real orography due to higher resolution of the data. A plot of the ATKIS DGM5 based model orography with 50 m horizontal resolution is provided in Figure 5-4 (a).

The original ATKIS DGM5 data include some inconsistencies in the surface heights of the river Elbe: Stripes with more than 1 km width and a maximal surface height deviation of approximately 1.5 m exist in the data. Most likely these stripes are an effect from merging the data from laser scans measured at different times without a sufficient tide[10] correction. To correct the erroneous data, heights of all water grid cells in the southern half of the model domain have been set to zero. This correction is not applied to the northern half of the domain to keep the different height for the Alster, which is ca. 3 m above sea level and not influenced by tidal flow. Height changes of the Elbe due to tidal effects are ignored in all simulations presented in this thesis.

5.2 Model experiments with varied surface heterogeneity and orography

5.2.1 Creation of modified maps

Four different surface class maps have been created, based on the METRAS_URBAN_A mapping introduced in Section 5.1.1. Each of the four surface class maps (Figure 5-3) has been used once with the real orography and once with flat terrain (Figure 5-4). Thus a set of eight simulations is available to analyze the effects of orography and surface heterogeneity on CBL above Hamburg. The individual surface class experiments are explained and named below. For the naming of the experiments with flat terrain the suffix "_F" is added to the names used for the surface class experiments.

The reference simulation ORIG / ORIG_F (— / −−) uses the original surface classes resulting directly from the METRAS_URBAN_A mapping (Figure 5-3 (a)). This map is modified by redistributing the surface classes of all land grid cells randomly to define the simulation setup MIX_L / MIX_L_F (— / −−, Figure 5-3 (b)). Here, and in the following, land grid cells are defined as grid cells, which have less than 50 % SGS water coverage. The SGS surface class distribution of all land grid cells, as calculated from the ORIG map, is provided in Table 5-4. This distribution still includes 2 % water coverages, due to the definition of land grid cells. The setup HOMO / HOMO_F (— / −−, Figure 5-3 (c)) uses this surface class distribution at each land grid cell.

---

[10] The mean tidal range at the gauge in Hamburg St. Pauli is 3.64 m, based on data taken from 2001-11-01 until 2010-10-31 (WSV 2014).

Thus HOMO / HOMO_F uses an artificially homogenized land surface, which exhibits the same SGS surface class distribution as the other setups. The setup MIX_A / MIX_A_F (— / – –, Figure 5-3 (d)) redistributes the surface classes from all grid cells of the ORIG setup randomly, including the water grid cells.
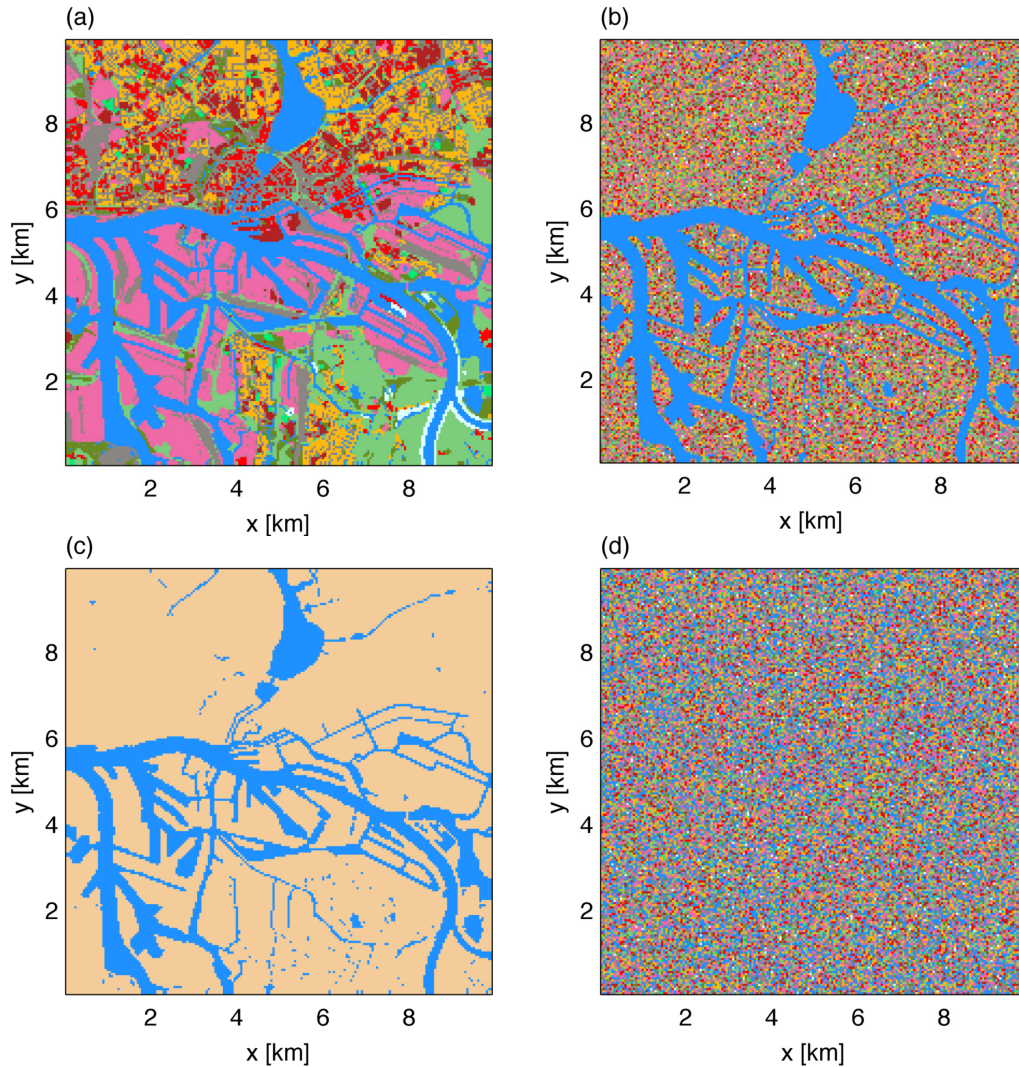

Figure 5-3: Main surface classes for the simulations ORIG/ORIG_F (a), MIX_L/MIX_L_F (b), HOMO/HOMO_F (c) and MIX_A/MIX_A_F (d). The color scale for (a), (b) and (d) is provided in Table 5-4. For (c) a separate land color is chosen, to illustrate that it is an artificial surface, using the SGS surface class distribution provided in Table 5-4.

Table 5-4: Surface class distribution for land grid cells (water coverage smaller 50 %) in Figure 5-3 (a), (b), (d). Subgrid scale fractions are included in the listed percentages. This surface class distribution is used for all land grid cell in the simulations HOMO and HOMO_F (Figure 5-3 (c)).

Class		O [%]	Class		O [%]
Water	0	2	Traffic	5	24
Mudflat	1	1	Bushes	6	6
Harbour & Industry	2	22	Sub Urban	7	14
Mixed Vegetation	3	17	Urban	8	7
Meadows	4	1	Urban Compact	9	6

The total domain averaged surface cover of individual classes from the reference map ORIG is conserved in all three surface class modification scenarios (MIX_L, HOMO and MIX_A). Conserving the total surface covers preserves the domain averaged surface characteristics, which is important for the comparison of the different simulations. For example this causes the same overall albedo of the model domain, which is needed to have the same amount of solar radiation for heating the surface during the day. The number of SGS surface classes (Table 5-3) is conserved in the redistribution scenarios MIX_L and MIX_A, but not in the homogenized setup HOMO. The surface flux averaging scheme (Schlünzen et al. 2012a, p. 20) is used for all four surface class setups, the parameter averaging scheme (Schlünzen et al. 2012a, p. 19) is not used.

The experiments MIX_L and MIX_A redistribute the surface classes only, but not the orography. There are only two states of orography, the original or flat terrain. Figure 5-4 shows the orography together with all possible water masks resulting from the different surface class scenarios.
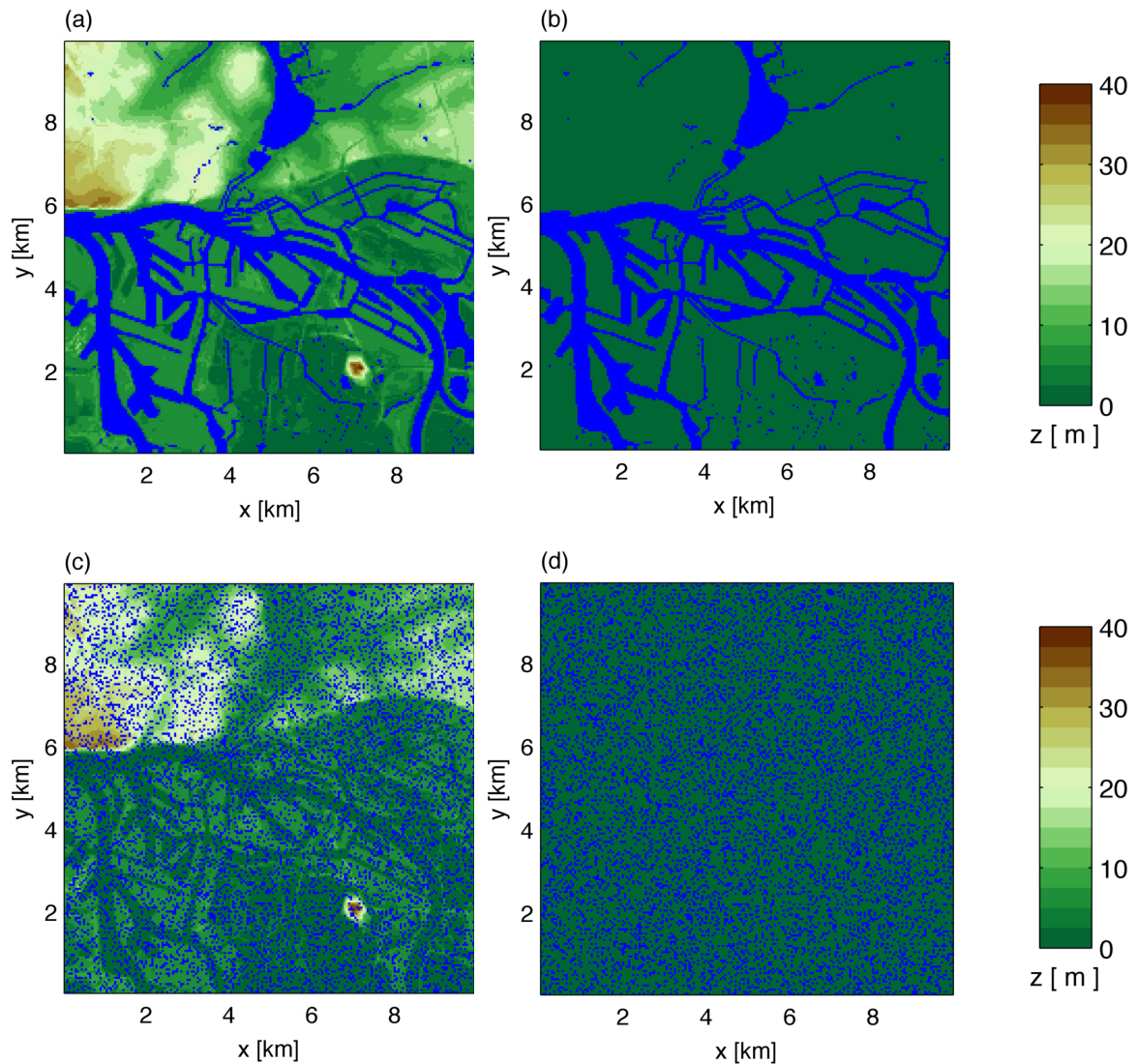

Figure 5-4: Orography and water masks for (a) the simulation setups ORIG, MIX_L and HOMO, for (b) ORIG_F, MIX_L_F and HOMO_F, for (c) MIX_A and for MIX_A_F (d). Grid cells with at least 50 % water coverage are marked in blue.

5.2.2   Description of model setup

The basic setup describes the simulation of a developing CBL over the course of a day, using the atmospheric input parameters described in Section 4.2.1. Zero large scale wind is assumed. In order to get a setup with little diffusion, $c = 1$ is used in Equation (4.8). The main distinction from the simulation setup introduced in Chapter 4 is the usage of different topographic maps to describe surface class and elevation. For each of the eight maps specified in Section 5.2.1 one simulation over 43 hours integration time has been performed, using 05:00 LST as initialization time. The starting date is the 15th July, which influences the calculation of solar radiation within the model (Schlünzen et al. 2012a, p. 93 – 97). For this date sunrise in Hamburg is at 04:01 LST and sunset at 20:33 LST.[11]

For performance reasons a major different model version (pre-release version of METRAS 2.1.1) has been used here, compared to the model version used for the simulations presented in Chapter 3 and Chapter 4 (METRAS-LES development based on METRAS 1.3). The used pre-release version of METRAS 2.1.1 differs only in technical details from the METRAS 2.1.1 release. It includes all tested METRAS-LES features and many other developments. For example it includes a restructured handling of SGS surface classes, which would in principle allow to use more than 10 surface classes, a basic loop parallelization (Augustin et al. 2008), a parallel solver for the pressure equation implemented by Bockelmann (2013, personal communication) and a refined sea ice model.

Besides using refined and modified topography data (Section 5.2.1) the setup used here differs from the setup used in Chapter 4 by inclusion of humidity. Thus a more complete model is used, which includes more physical processes. For example moisture fluxes influence the energy exchanges at the surface and where the moisture content of the air modifies buoyancy. During model initialization a homogeneous relative humidity of 50 % was assumed for the whole model domain. This value is chosen in consistency with urban climate assessments for Hamburg performed by Funk et al. (2012). Time series of volume integrated model variables show, that in none of the performed simulations condensation takes place during the first 19 h of time integration. Therefore, focusing in the analysis on the first simulation day guaranties a cloud free situation. This is helpful for more robust sensitivity studies, as occurrence of clouds can create larger feedbacks. Such feedbacks can complicate the analysis of single run sensitivity studies and may require larger ensembles to provide robust results. Nevertheless, for the sake of completeness results from the second day

---

[11] These times for sun rise and sunset have been calculated independently from the calculation in the model. Times listed here are calculated based on internet query for sunrise and sunset times in Hamburg at July 15th (Wolfram|Alpha 2014) and the time difference of 50 min between LST and UTC available from metadata in the NetCDF model output.

are presented as well, even though some isolated clouds form in some of the simulations.

5.3 Model results with varied surface heterogeneity and orography

5.3.1 Sensitivity on instantaneous values of meteorological variables

To provide an introduction to the different model solutions gained from the simulations of the topography experiment (Section 5.2) instantaneous cross sections of real temperatures are shown for 10 m (Figure 5-5) and 150 m (Figure 5-6) above ground level. These model snapshots are taken from the simulations of the orography experiment (defined as simulation set ORIG, ORIG_F, MIX_L, MIX_L_F, HOMO, HOMO_F, MIX_A and MIX_A_F) at 12:00 LST of the first simulation day.

The temperature fields above land are structured by convective flow fields. The 10 m cross sections of the simulations ORIG, ORIG_F, MIX_L, MIX_L_F, HOMO and HOMO_F (Figure 5-5 (a) – (f)) show large similarities among each other and a clear influence of the water surfaces. In principle these model solutions are similar to the results from the simulations presented in Chapter 4 (only partially shown here). For the simulations MIX_A and MIX_A_F, which also redistribute the water cells, structural difference from the reference solution ORIG (Figure 5-5 (a)) can be seen in the model results (Figure 5-5 (g) – (h)). Here the simulations are more similar to the results from Chapter 3, even though differences exist due to influences of orography and the mosaic distribution of surface classes.

At 150 m above the ground the same similarity between the setups ORIG, MIX_L and HOMO is found (Figure 5-6 (a), (c), (e)). In contrast to the temperature fields near the surface, more differences between the simulations with flat and real orography are visible. For example there is an edge in the temperature field associated with the slopes north of the Elbe valley in all simulations with orography (e.g. Figure 5-6 (e), x = 0 – 2 km, y = 6 – 8 km). The pure orographic effect is visible from the experiment MIX_A, which leaves out the additional thermal driven surface effects, due to the mixed surface classes (Figure 5-6 (g)). This orographic influence is mainly an effect of the terrain following analysis. Higher altitudes above sea level are visible by areas with lower air temperatures. This influence would be less pronounced in fields of potential temperature, because the vertical gradient of potential temperature can be expected to be (near) neutral in the CBL above a super adiabatic surface layer. Similar to the 10 m temperature fields the main structural difference among the eight simulations is between the two experiments redistributing the water surfaces (MIX_A/MIX_A_F) and the other six experiments.
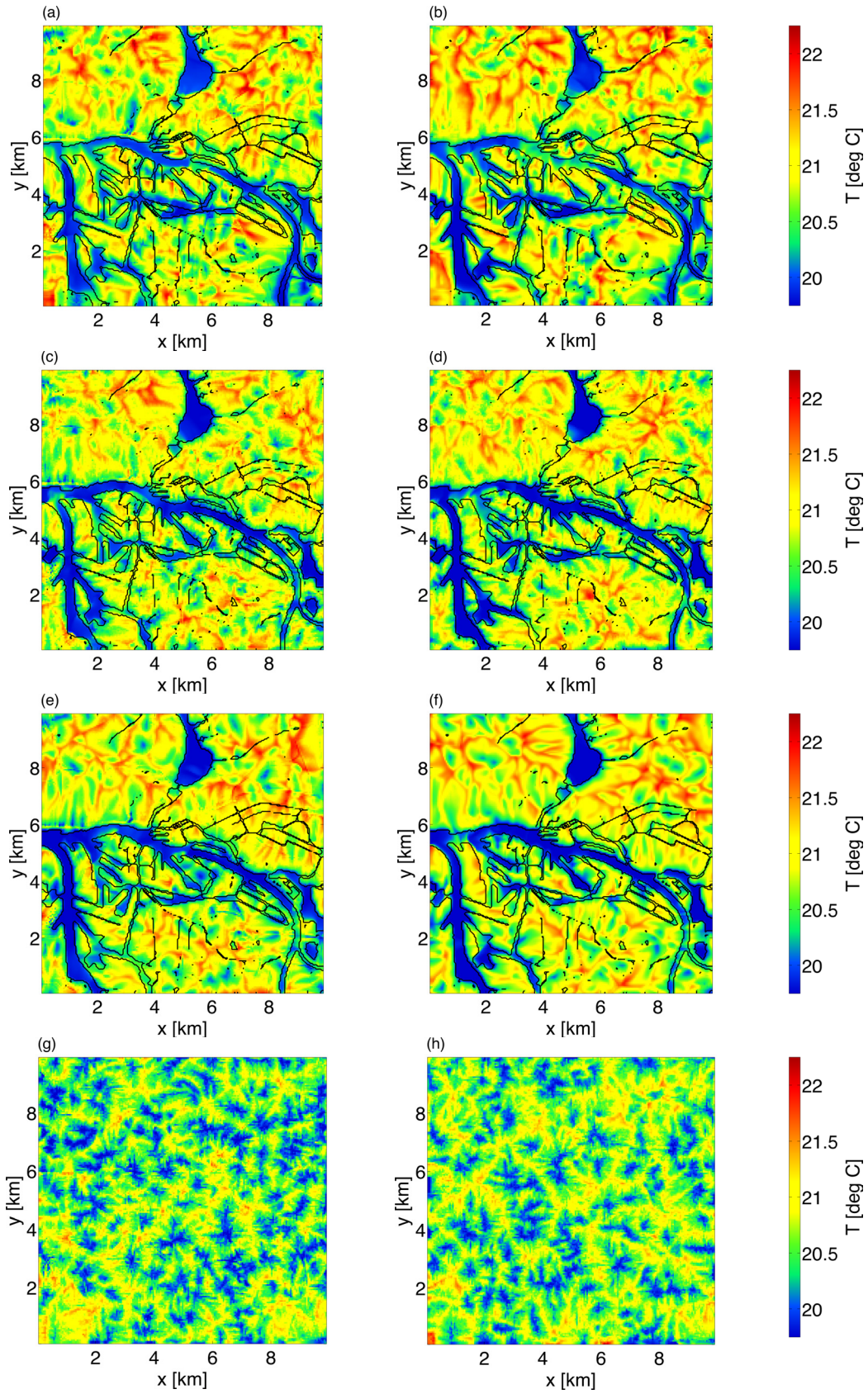
Figure 5-5: Real temperature at 10 m above ground level at 12:00 LST of the first simulation day for the experiments ORIG (a), ORIG_F (b), MIX_L (c), MIX_L_F (d), HOMO (e), HOMO_F (f), MIX_A (g) and MIX_A_F (h).
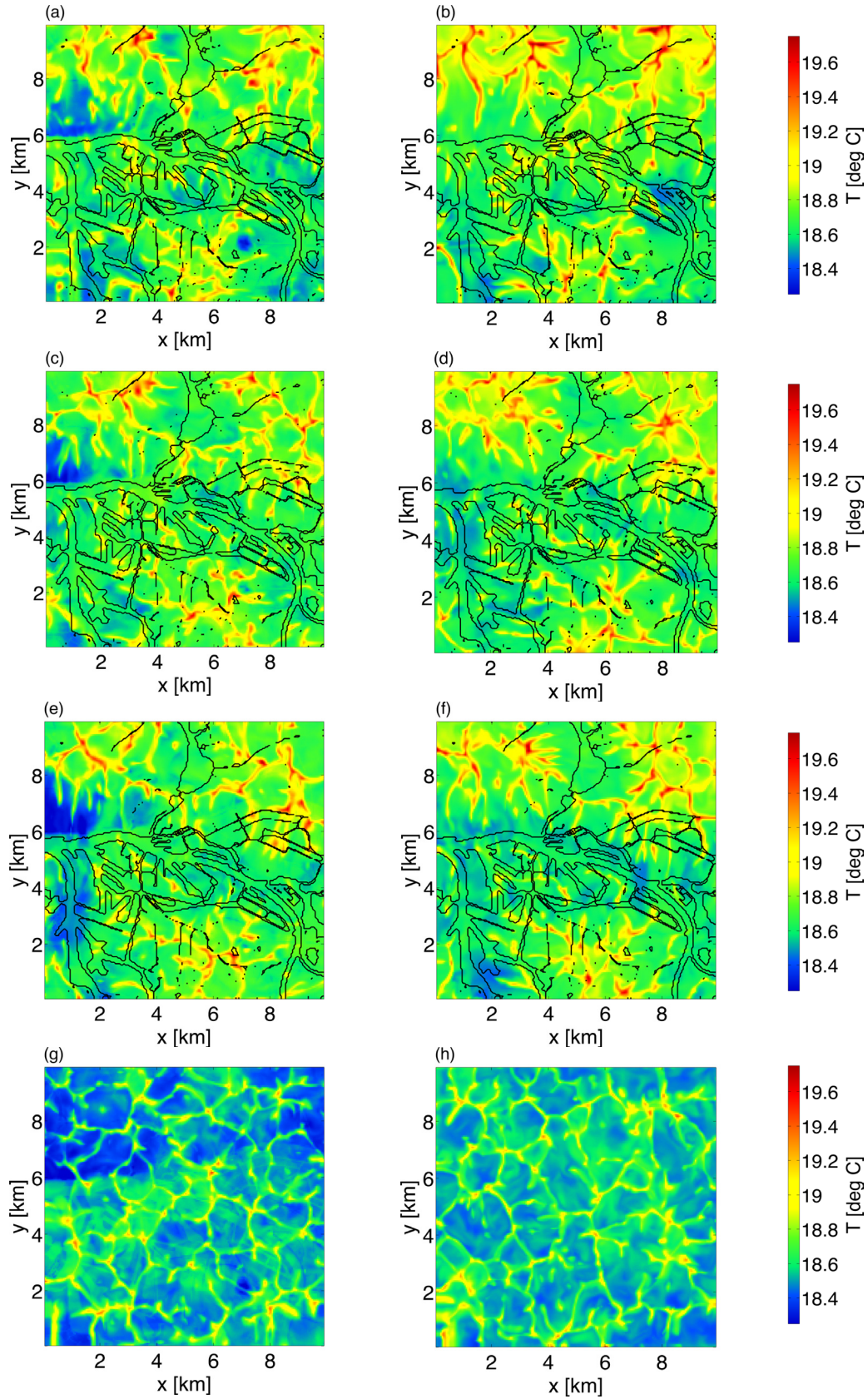
Figure 5-6: Real temperature at 150 m above ground level at 12:00 LST of the first simulation day for the experiments ORIG (a), ORIG_F (b), MIX_L (c), MIX_L_F (d), HOMO (e), HOMO_F (f), MIX_A (g) and MIX_A_F (h).

The above given introduction into the model results indicates that the land water contrast may have a larger impact on the model results than the smaller scale surface

heterogeneities and the orography. More quantitative assessments of the topography experiment are following in the next sections. Besides providing a first impression of the experiment outcome, the shown examples demonstrate, that a CBL situation above the city of Hamburg can be simulated also with the major changed model version of METRAS-LES. The principle findings from the validation and sensitivity experiments discussed in Chapter 3 and Chapter 4, should also hold true for the experiment results discussed in the following.

5.3.2   Sensitivity of averaged values of meteorological variables

In the following it is investigated to what extent domain averaged model results are sensitive on the topography experiment described in Section 5.2. In the context of urban climate applications such analyses might be interesting for questions, which do not require or allow further spatial distinction. An example might be the estimating of biometeorological indices for an urban population, which is only described by a homogeneous population density. From a modelling perspective the domain averaged analysis investigates to what extent spatial details of surface data are needed in simulations performed for such questions. Additionally, analyzing the topography experiments in terms of domain averages provides further possibilities to discuss physical mechanism acting in CBL situations on the atmosphere above Hamburg.

Sensitivity of real temperature

As a first step, area averaged real temperatures at 10 m above ground level have been calculated for all eight simulations. Figure 5-7 shows time series of these arithmetic averages, taken (a) over all grid cells, (b) over all land grid cells and (c) over all water grid cells. Additionally, all values between the 5 and 95 percentiles are marked in Figure 5-7 for the simulations ORIG (■) and MIX_A_F (■), to provide a measure of the distribution width. The percentiles are also separately analyzed for all grid cells and the land and water grid cells alone. The time series in Figure 5-7 are calculated from instantaneous model output, written every 10 min. They show smooth diurnal cycles, which do not fluctuate in time. Thus, temporal fluctuations occurring in the model solutions are local and balance each other in this domain averaged analysis.

The area averaged air temperatures show similar diurnal cycles for nearly all experiments, especially during the first day. Only the two scenarios MIX_A and MIX_A_F, which redistribute the water grid cells from the rivers Elbe and Alster within the model domain, show lower averages of the 10 m temperatures over all grid points. Similarly, the 5 and 95 percentiles over land are at lower levels in the simulation MIX_A_F compared to the simulation ORIG. The opposite effect is visible for the water cells, i.e. the absence of connected water areas causes higher temperature peaks over water. Due to the dominance of the land cells (Section 5.1.1) the lower values are also visible in the domain averages and percentiles.
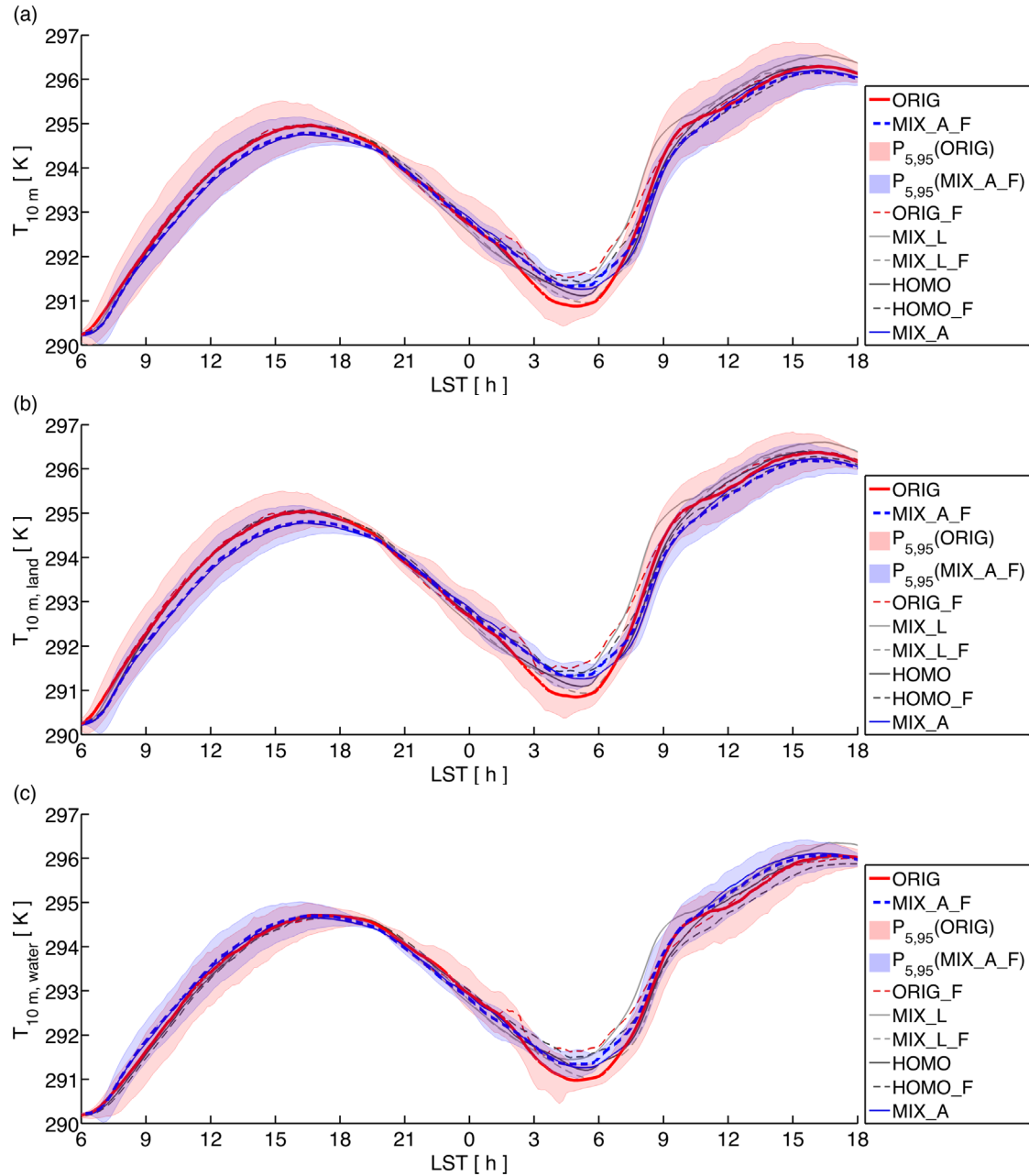
Figure 5-7: Real temperatures at 10 m above ground level for the topography experiment defined in Section 5.2.1. Time series show spatial arithmetic averages over all grid cells (a), over all land grid cells (b) and over all water grid cells (c). The shaded area include 90 % of all values and are bounded by the 5 and 95 percentiles from the simulation ORIG (red) and MIX_A_F (blue).

The differences of the area averaged temperatures from the area averaged temperature of the reference simulation ORIG have been calculated. Arithmetic means of these differences have been calculated over all available (daytime) output times in the interval from 09:00 LST to 18:00 LST. For the simulation MIX_L_F, the last considered model output is 17:10 LST of the second day, due to numerical instabilities in the model. The missing 50 min are ignored in the analysis of this simulation. All other simulations are complete. The resulting daytime mean temperature differences are provided in Table 5-5 as quantitative summary of the differences in the area averaged time series.

Table 5-5: Temperature difference and difference between 5 and 95 percentiles of real temperature, analyzed from the topography experiment. Given values are time averages calculated from spatial averages / percentiles taken over all grid cells (white), all land grid cells (green) and all water cells (blue) at 10 m above ground. Time averaging is done from 9 LST to 18 LST. Red font colors mark values lower than occurring in the reference experiment. Bold font marks differences to the reference experiment of at least 0.2 K for the mean difference and 10 % for the normalized percentile difference.

| | $T - T_{ORIG}$ [K] | | $P_{05,95}(T)$ [K] | | $P_{05,95}(T)$ / $P_{05,95}(T_{ORIG})$ | |
	day 1 9–18 h	day 2 9–18 h	day 1 9–18 h	day 2 9–18 h	day 1 9–18 h	day 2 9–18 h
ORIG	0.0	0.0	1.3	1.2	1.00	1.00
only land	0.0	0.0	1.1	1.0	1.00	1.00
only water	0.0	0.0	1.0	1.0	1.00	1.00
ORIG_F	0.0	0.0	1.4	1.3	1.08	1.08
only land	0.1	0.1	1.1	1.1	1.03	1.03
only water	0.0	0.0	1.1	1.0	1.02	0.99
MIX_L	0.0	**0.3**	1.3	1.1	0.97	0.92
only land	0.0	**0.2**	1.0	0.9	**0.90**	**0.88**
only water	0.0	**0.3**	1.1	1.0	1.05	0.99
MIX_L_F	0.0	0.1	1.3	1.3	1.04	1.03
only land	0.0	0.1	1.0	1.0	**0.90**	0.93
only water	-0.1	0.0	1.1	1.1	1.08	1.03
HOMO	0.0	0.0	1.3	1.2	1.00	0.99
only land	0.0	0.0	1.0	1.0	0.92	0.93
only water	-0.1	0.0	1.1	1.0	1.06	1.00
HOMO_F	0.0	**-0.2**	1.4	1.3	1.07	1.06
only land	0.0	-0.1	1.0	1.0	0.93	0.93
only water	-0.1	**-0.2**	1.1	1.0	1.06	1.00
MIX_A	**-0.2**	-0.1	1.0	0.9	**0.76**	**0.75**
only land	**-0.3**	**-0.2**	1.0	0.9	**0.88**	**0.87**
only water	0.1	**0.2**	0.9	0.9	0.91	**0.87**
MIX_A_F	**-0.2**	**-0.2**	0.9	0.9	**0.73**	**0.72**
only land	**-0.3**	**-0.2**	0.9	0.9	**0.84**	**0.84**
only water	0.1	0.1	0.9	0.9	**0.88**	**0.85**

Table 5-5 also provides the mean daytime difference between the 5 and 95 percentiles for each experiment as absolute and as normalized values. The normalization with the percentile distance of the reference simulation ORIG has been done prior time averaging. Thus due to rounding effects the given normalized values can slightly deviate from values, which could be received by normalization of the absolute percentile differences given in Table 5-5. The tabular comparison distinguishes the analysis for all grid cells, for the land grid cells and for the water grid cells, as done in

the time series. All values, which are reduced by 10 % (percentile difference) or 0.2 K (mean difference) compared to the reference experiment ORIG, are marked in bold in Table 5-5, to support the interpretation of the results. Likewise any reduction compared to the experiment ORIG is marked by red font color.

The domain averaged temperatures in the experiments ORIG_F, MIX_L, MIX_L_F, HOMO and HOMO_F are very similar, especially for the first simulation day (Figure 5-7). For these experiments the daytime average temperature differences from the reference simulation show at most deviations of -0.1 K for the average over the water cells during the first simulation date (Table 5-5). Hence, homogenizing the surface classes over land and flattening the orography does not influence the area averaged 10 m temperature in any important way for the simulated CBL situation.

For the experiments MIX_A and MIX_A_F, which also redistribute the water surfaces, an effect on domain averaged temperature can be seen in Figure 5-7, also for the first day. For this day, their daytime mean 10 m temperature is 0.2 K lower than in the reference simulation (Table 5-5). This decrease of temperature happens over land only, while over water a smaller increase acts in the opposite direction. The 0.2 K lower domain averaged temperature is small compared to the amplitude of the simulated diurnal cycle, which is in the order of 5 K (Figure 5-7). However, it is not small compared to the spatial distribution within the domain, as the differences between the 5 and 95 percentiles are in the order of 1 K during daytime (Table 5-5).

A small reduction of the temperature distribution width, characterized by the difference of the 5 and 95 percentile, is found over land in the redistribution / homogenization experiments MIX_L, MIX_L_F, HOMO and HOMO_F, going along with a small increase over water (Table 5-5). The reductions compared to the reference simulation ORIG are smaller than 10 % for nearly all analysis periods. Like for the mean values the influence on the distribution width is largest in the experiments MIX_A and MIX_A_F, which show a reduction of approximately 25 % in the daytime percentile difference compared to the reference simulation ORIG.

The redistribution of the water cells has stronger effects on the domain average and distribution width of 10 m real air temperature, than all other performed topography experiments. The results suggests, that for a realistic simulation of domain averaged statistics of 10 m air real temperature the correct spatial distribution of water surfaces should be kept, as only keeping the correct distribution of water surfaces leads to different model results.

Sensitivity of sensible heat flux

To investigate the physical reasons for the lower average temperatures in the experiments MIX_A and MIX_A_F, time series of domain averaged sensible heat fluxes have been calculated (Figure 5-8). Similar to the analysis of the 10 m temperature, the 5 and 95 percentiles for the experiments ORIG and MIX_A_F are also shown in Figure

5-8 and summarizing daytime averages of mean differences and percentile differences are provided in Table 5-6.
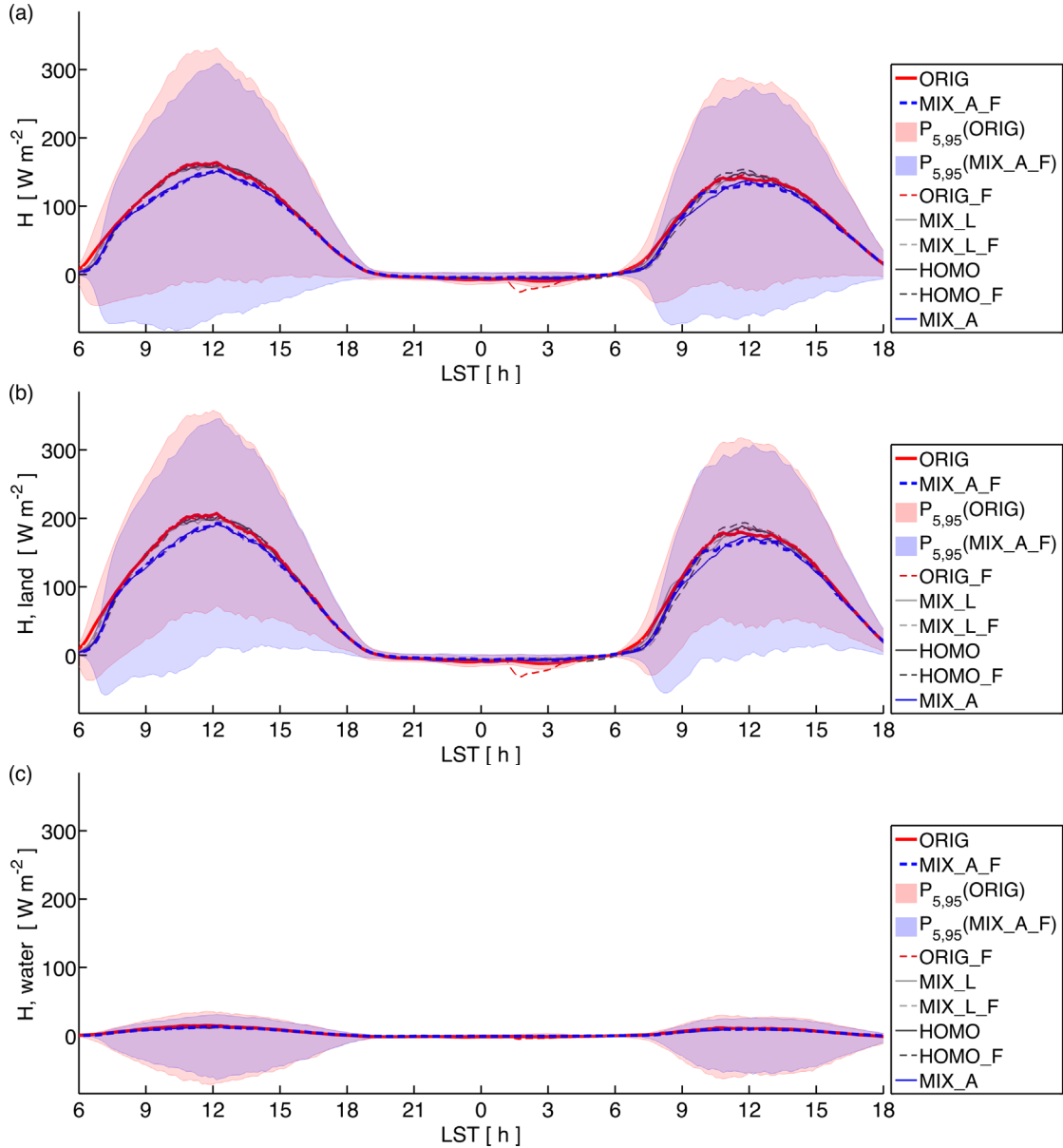

Figure 5-8: Same as Figure 5-7 but for the sensible heat flux in the surface layer.

Consistent with the findings for temperature the experiments MIX_A and MIX_A_F show lower domain averaged mean sensible heat fluxes, while the other experiments are more similar to each other. The reductions of the heat fluxes over land are in the order of 10 W m^{-2} for the experiments MIX_A and MIX_A_F (Table 5-6), but one order of magnitude smaller for the other experiments. For the reference simulation ORIG, the time average of the heat flux between 9:00 and 18:00 is 117 W m^{-2} for the first and 103 W m^{-2} for the second simulation day. Therefore the maximum change over all grid points is 7.7 %, found for MIX_A_F at the first day.

The distribution width, measured by the difference between 95 and 5 percentile, does not decrease for the land cells in the experiments MIX_L and MIX_A_F. Instead lower

values for the 5 percentile of the heat fluxes over land (Figure 5-8 (b)) result in an increase of the percentile difference compared to the reference simulation. The experiments HOMO and HOMO_F, which have a homogenized land surface, show a reduction of a little more than 20 % in the percentile distance over land. The remaining 80 % of the spatial variability of the heat flux over land is most likely to be explained by the variable flow and temperature fields in the simulated CBL and river breeze regime.

Table 5-6: Same as Table 5-5 but for the sensible heat flux in the surface layer. Corresponding time series are shown in Figure 5-8. Bold font marks difference to the reference experiment of at least 5 W m^{-2} for the flux difference and 10 % for the percentiles.

	HF - H$_{FORIG}$ [W m^{-2}]		P$_{05,95}$(HF) [W m^{-2}]		P$_{05,95}$(HF) / P$_{05,95}$(HF$_{ORIG}$)	
	day 1 9–18 h	day 2 9–18 h	day 1 9–18 h	day 2 9–18 h	day 1 9–18 h	day 2 9–18 h
ORIG	0.0	0.0	247	223	1.00	1.00
only land	0.0	0.0	213	192	1.00	1.00
only water	0.0	0.0	74	67	1.00	1.00
ORIG_F	0.0	0.6	247	222	1.00	1.00
only land	0.0	0.7	212	191	1.00	1.00
only water	0.2	0.3	75	66	1.02	0.99
MIX_L	-1.2	-3.2	251	220	1.02	0.99
only land	-1.6	-4.0	218	191	1.02	1.00
only water	0.0	-0.3	73	65	1.00	0.98
MIX_L_F	-1.4	0.0	251	248	1.01	1.03
only land	-1.8	-0.1	218	217	1.02	1.05
only water	0.1	-0.2	72	70	0.98	0.98
HOMO	0.1	0.2	**211**	**190**	**0.86**	**0.86**
only land	-0.4	-0.2	**164**	**148**	**0.78**	**0.79**
only water	-1.5	-1.1	**64**	**56**	**0.86**	**0.84**
HOMO_F	-0.3	0.3	**212**	**191**	**0.86**	**0.86**
only land	-0.9	-0.2	**166**	**148**	**0.79**	**0.78**
only water	-1.4	-0.9	**64**	**57**	**0.87**	**0.84**
MIX_A	**-8.8**	**-7.4**	270	**241**	**1.10**	1.08
only land	**-11.0**	**-9.32**	**249**	**222**	**1.17**	**1.16**
only water	-1.1	-0.8	**65**	**59**	**0.90**	**0.89**
MIX_A_F	**-9.0**	**-5.9**	269	243	1.09	1.09
only land	**-11.3**	**-7.5**	**248**	**222**	**1.17**	**1.16**
only water	-1.1	-0.6	**65**	**61**	**0.90**	0.91

The reduced variability in the heat fluxes over land for the setup HOMO/HOMO_F has only little effects on mean fluxes. This indicates, that for simulations, which should only provide mean values, the spatial details in in the surface map from Figure 5-3 (a)

are most likely not needed. Instead a simplified map with a homogenized surface (Figure 5-3 (c)) might be sufficient, as long as the correct percentages of the surface class distribution and the land water contrast are kept.

Table 5-6 shows, that most simulations with flat surfaces (MIX_L_F, HOMO_L_F and MIX_A_F) result in lower daytime fluxes for the first simulation day compared to the respective simulations with orography (MIX_L, HOMO and MIX_A). This effect is small (0.2 W m^{-2}) and opposed for the second simulation day and in the simulation pair ORIG / ORIG_F. To check, if there is really a small effect, larger ensembles would be needed. But it can be concluded, that the domain averaged heat flux is more sensitive on redistributing the water cells than on flattening the moderate terrain. Thus neglecting the terrain results in a smaller error than neglecting the proper localization of the water areas, which is a very plausible result for simulations in the Hamburg inner-city and harbor model domain.

Sensitivity of horizontal wind speed

The above analysis has shown, that redistributing the water grid cells randomly in the model domain (experiments MIX_A and MIX_A_F) results in lower surface heat fluxes over land, which may be claimed responsible for lower surface layer temperatures. One physical explanation might be the missing river breeze circulation, caused by the Elbe and Alster in the other experiments. The absence of this additional circulation could cause lower wind speeds over land in the pure convective scenarios MIX_A and MIX_A_F. Lower wind speeds would cause lower friction velocities according Equation (3.32) and thus lower heat fluxes according Equation (3.30). To verify this hypothesis, the same analysis as performed for temperature and heat fluxes is repeated for horizontal wind speed at 10 m above ground level (Figure 5-9, Table 5-7).

The analysis of the horizontal wind speed confirms the hypothesis that a notable reduction of wind speed occurs in the simulations MIX_A and MIX_A_F (Figure 5-9). Over all grid points it is above 25 % (Table 5-7), with larger contributions over land. Over water also the land modification experiments MIX_L/MIX_L_F and HOMO/HOMO_F show a reduced wind speed. Most likely different surface properties of the adjacent riverside land cells contribute to that. The distribution width decreases with similar rates as the mean values (Table 5-7). This could be seen as an indicator, that the shape of the wind distribution keeps similar in all simulations.

Simulations to estimate domain averages of the thermally induced horizontal wind speeds requires the correct land / water distribution. E.g. including of river breeze effects in the simulation is needed, just including the near surface compensating flow from convective cells in the water surface redistributing experiments underestimates the occurring wind.
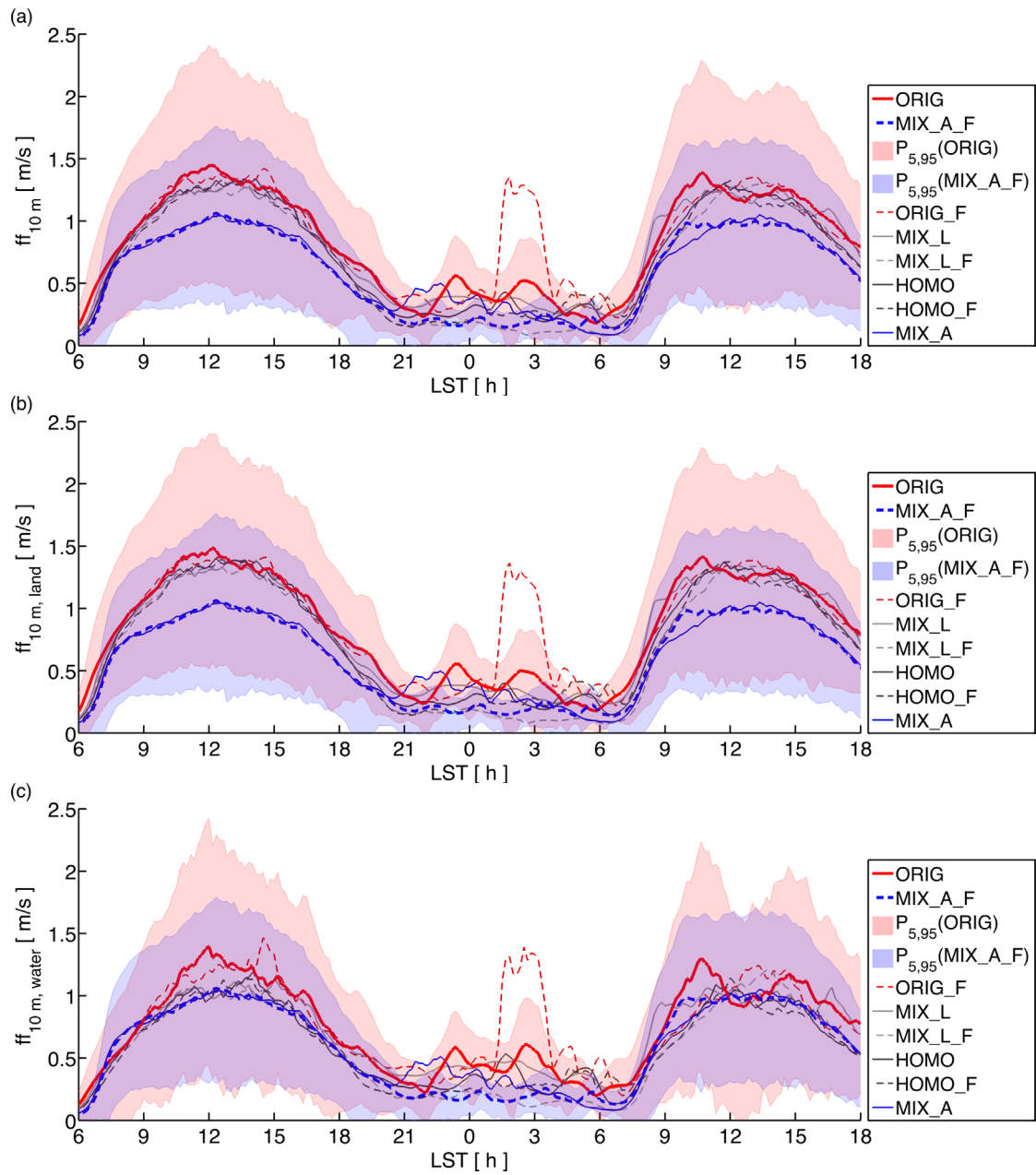
Figure 5-9: Same as Figure 5-7 but for the horizontal wind speed at 10 m above ground level.

Table 5-7: Same as Table 5-5 but for horizontal wind speed at 10 m above ground level. Bold font marks difference to the reference experiment of at least 0.2 m s^{-1} or 10 %.

	ff - ff$_{ORIG}$ [m s^{-1}]		(ff – ff$_{ORIG}$) / ff$_{ORIG}$		P$_{05,95}$(ff) [m s^{-1}]		P$_{05,95}$ff) / P$_{05,95}$(ff$_{ORIG}$)	
	day 1 9–18 h	day 2 9–18 h	day 1 9–18 h	day 2 9–18 h	day 1 9–18 h	day 2 9–18 h	day 1 9–18 h	day 2 9–18 h
ORIG	0.00	0.00	0.00	0.00	1.61	1.56	1.00	1.00
only land	0.0	0.00	0.00	0.00	1.57	1.52	1.00	1.00
only water	0.00	0.00	0.00	0.00	1.62	1.56	1.00	1.00
ORIG_F	0.00	-0.03	0.00	-0.03	1.61	1.54	1.00	0.99
only land	0.00	-0.02	0.00	-0.02	1.56	1.49	1.00	0.98
only water	0.00	-0.07	0.00	-0.07	1.66	1.51	1.02	0.97
MIX_L	-0.07	-0.04	-0.06	-0.03	1.55	1.52	0.96	0.99
only land	-0.05	-0.03	-0.04	-0.03	1.48	1.47	0.95	0.97
only water	-0.12	-0.06	-0.11	-0.06	1.57	1.53	0.97	1.00
MIX_L_F	-0.10	-0.09	-0.08	-0.08	1.50	1.51	0.93	0.94
only land	-0.08	-0.08	-0.07	-0.07	1.44	1.46	0.91	0.93
only water	-0.16	-0.13	-0.15	-0.13	1.51	1.48	0.93	0.93
HOMO	-0.06	-0.08	-0.05	-0.07	1.55	1.49	0.96	0.95
only land	-0.04	-0.06	-0.03	-0.05	1.49	1.43	0.95	0.94
only water	-0.16	-0.17	-0.15	-0.17	1.50	1.41	0.92	0.90
HOMO_F	-0.08	-0.11	-0.07	-0.10	1.53	1.44	0.95	0.92
only land	-0.06	-0.09	-0.05	-0.08	1.47	1.37	0.93	**0.90**
only water	-0.17	-0.19	-0.16	-0.18	1.50	1.39	0.92	**0.89**
MIX_A	**-0.30**	**-0.28**	**-0.25**	**-0.24**	1.21	1.19	**0.75**	**0.77**
only land	**-0.34**	**-0.32**	**-0.28**	**-0.27**	1.20	1.18	**0.76**	**0.78**
only water	-0.18	-0.14	-0.17	-0.14	1.25	1.23	**0.77**	**0.79**
MIX_A_F	**-0.31**	**-0.27**	**-0.26**	**-0.23**	1.19	1.19	**0.74**	**0.77**
only land	**-0.34**	**-0.31**	**-0.28**	**-0.26**	1.18	1.18	**0.75**	**0.78**
only water	-0.19	-0.13	-0.18	-0.13	1.23	1.23	**0.76**	**0.79**

Sensitivity of vertical wind speed

The wind speed analysis above (Figure 5-9, Table 5-7) includes only the horizontal wind components. Thus, the analysis of the domain averaged near surface fields is completed by the analysis of vertical wind speed in 20 m above ground level.

Figure 5-10 shows the diurnally cycle of mean vertical wind speed over the land cells (a) and over the water cells (b), as well as the 5 and 95 percentiles for the simulations ORIG ( ) and MIX_A_F ( ). In difference to the other variables (Figure 5-7, Figure 5-8 and Figure 5-9) the diurnal cycle of the percentiles is much more dominant than the diurnal cycle of the mean values, because up and down winds balance each other in the spatial average. This indicates that the vertical wind speed is more influenced by convective plumes than by an organized river breeze circulation. The same reason

explains, why there is no relevant difference visible in the distribution width between the experiments ORIG and MIX_A_F.
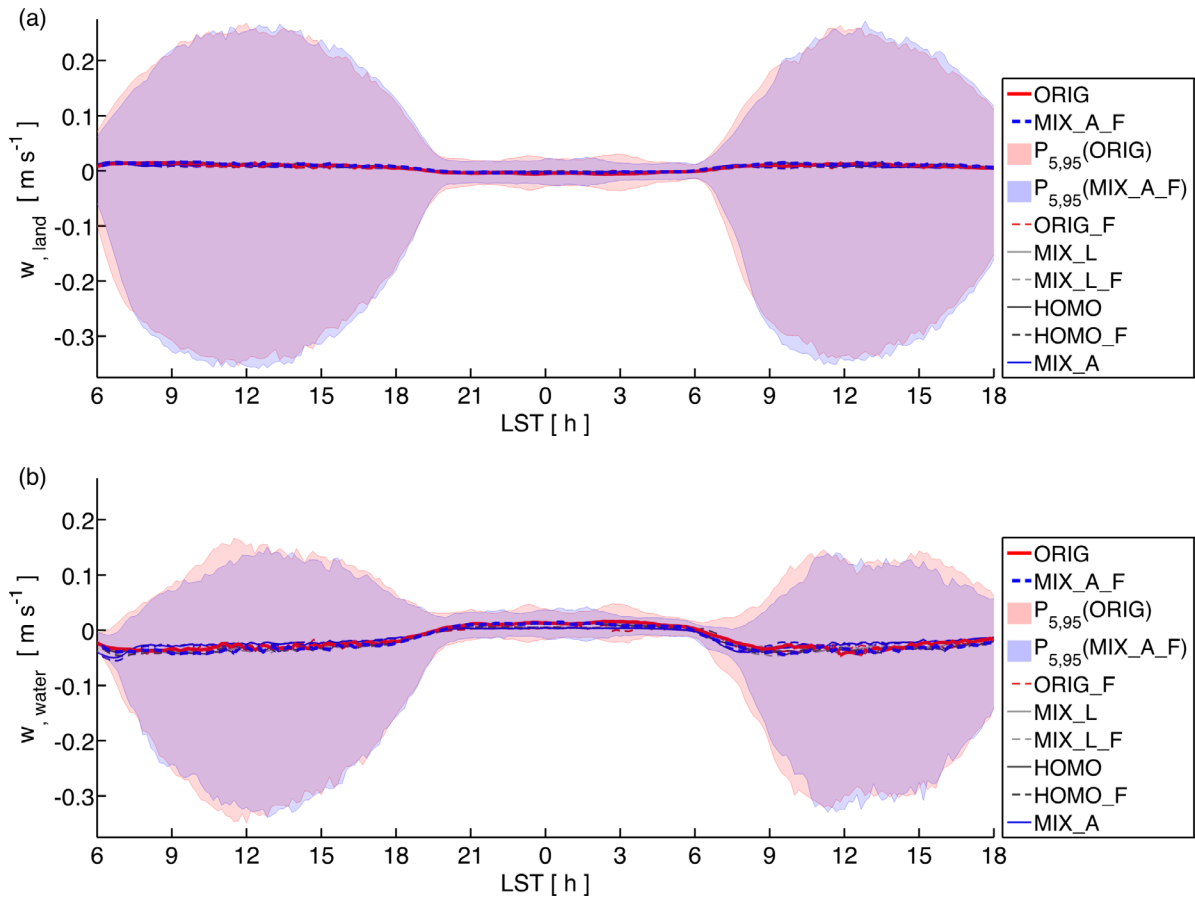

Figure 5-10: Vertical wind speed at 20 m above ground level for the topography experiment defined in Section 5.2.1. Spatial arithmetic averages are shown as time series over (a) all land grid cells and (b) over all water grid cells. The 5 and 95 percentiles from the simulations ORIG (red) and MIX_A_F (blue) are marked by shaded areas.

The y-axis in Figure 5-10 does not allow to compare the mean values between the different simulations. Thus Figure 5-11 shows the mean values at a proper scale. Providing averages above land cells (×, □) and above water cells (○, +) in one figure gives the opportunity to analyze the occurring thermal circulations in the time domain: During daytime on average rising motion occurs over land and sinking motion over the water areas. During night signs reverse and the difference between rising and sinking motion decrease. Hence, circulations during night are weaker than during the day, which is also supported by the horizontal wind speed (Figure 5-9). The reasons are the missing convection during the night and the fact that land sea breeze like circulations are normally weaker during night than during day (e.g. Bock et al. 2002, p. 179).

The distribution of vertical wind speed is different over water than over land. The strongest downward motions are approximately the same over both surfaces, which can be seen from the 5 percentile (Figure 5-10). The different 95 percentiles over land and water show that upward motion is suppressed over the colder water areas.

An effect of orography can be seen during nighttime: Downslope winds towards the lower rivers cause an additional mass flow which needs to be balanced by upward motion above the low-lying rivers Elbe and Alster in simulation ORIG, MIX_L and HOMO. During daytime all mean values over land are similar for all members of the topography experiment. This indicates, that the details of the topography are not important to simulate the vertical motions under convective conditions.
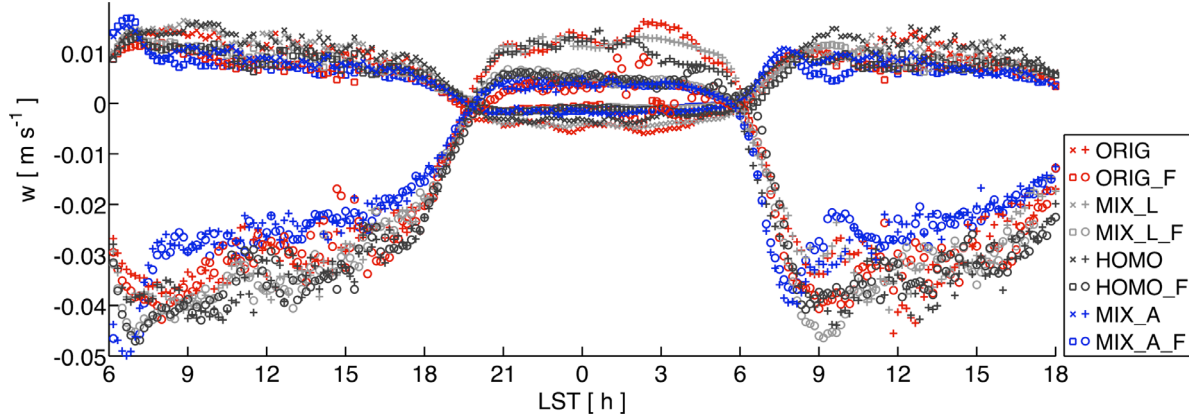
Figure 5-11: Vertical wind speeds from topography experiment (Section 5.2) shown as arithmetic average over all land cells (×, □) and over all water cells (○, +). Simulations with flat terrain are marked by (○, □). Related percentiles are provided in Figure 5-10.

5.3.3   Sensitivity of vertical extension and structure of boundary layer

In Section 5.3.2 model results from the topography experiment (Section 5.2) have been analyzed as averages from all (or selected) grid cells near the surface. To extent the discussion to higher elevations, characteristic heights (Section 3.3.1) have been calculated from instantaneous model output with an output interval of 10 min. This analysis incorporates data from all grid cells of the model and is intended to investigate how topography affects the vertical structure of the daytime CBL above the model area. Only times between 9:00 and 18:00 LST are examined, because convection breaks down during night (Figure 5-11). Also, the LES modus may not be justified for the used model resolution (Section 5.1.1) during nocturnal, stably stratified conditions.

Time series of the height of the CBL, as measured by the characteristic height z_i(HF), are shown in Figure 5-12. The presented time series are moving averages using a symmetric window of two hours, which also use data before 9:00 LST and after 18:00 LST. The moving averages are needed for better comparison of the topography experiments, because z_i(HF) fluctuates on the output interval of 10 min. Time series of the characteristic heights at all output time steps are presented in Appendix E to demonstrate how this fluctuating variable is fitted by the moving average (Figure E-1). Additionally moving standard deviations are shown for the simulations ORIG and MIX_A_F.
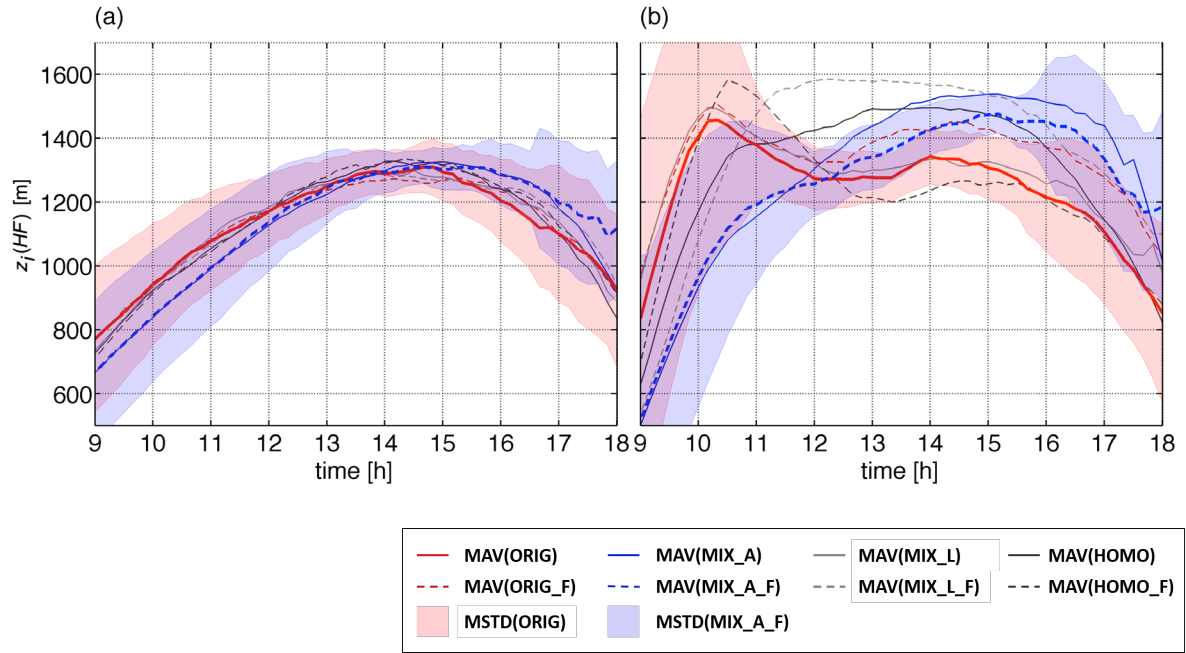
Figure 5-12: Moving average (MAV, MathWorks 2013) for the height of the minimum of the resolved heat flux for all topography experiments defined in Section 5.2.1. Solid lines mark the simulations including orography, dashed lines the simulations with flat terrain. Moving standard deviations (MSTD, D'Errico 2014) are shown as shaded areas for the simulations ORIG (red) and MIX_A_F (blue). MSTD and MAV use a two hour centered window to filter the data points shown in Figure E-1 and one hour of data before and after the shown interval.

Figure 5-12 shows, that the experiments MIX_A and MIX_A_F exhibit a delayed boundary layer development in the morning, but also delay the decrease of z_i(HF) in the afternoon. For the first day this delay is about half an hour. For the second day the quantification is more uncertain, which can also be seen by the larger spread of the other experiments. The delay in MIX_A and MIX_A_F is most likely caused by the decreased heat fluxes (Figure 5-8) for the experiments, for which the water surfaces are redistributed within the model domain.

In consistency with the findings from Section 5.3.2 the analysis of z_i(HF) shows, that the influence of orography is smaller than the influence of surface class distribution. Further on, the analysis suggests, that the correct localization of water surfaces does not only affect the near surface statistics, but also modifies the time development of the complete CBL and impacts the lowest 1 – 2 km of the atmosphere. One application where such details might be relevant could be the assessment of urban air quality, because the height of the boundary layer is important for the volume, in which pollutions can be mixed. A delayed CBL development in the morning can cause longer periods of pollution load due to near surface emissions. Therefore the existence of Elbe and Alster may eventually be helpful for improving the morning air quality in Hamburg, by supporting the growth of convective boundary layers. Nevertheless, it should be noted, that this hypothesis on possible impact on air quality is speculative based on the presented model experiments. Further studies would be needed to check its validity.

The characteristic height z_i(HF) provides a measure for the top of the CBL. For comparison the structure of the simulated CBL the height of the maximum vertical wind variance $z_{\max(\sigma_w^2)}$ is calculated as second characteristic height (Figure 5-13). The time delay found in the analysis for z_i(HF) for the simulations MIX_A and MIX_A_F can also be found in this second characteristic height. The experiments MIX_L/MIX_L_F and HOMO/HOMO_F show somehow larger values for $z_{\max(\sigma_w^2)}$ than the reference simulation ORIG. From the presented analysis it is unclear if there is a clear physical reason or if that is a random result, which just shows the spread of possible solutions.
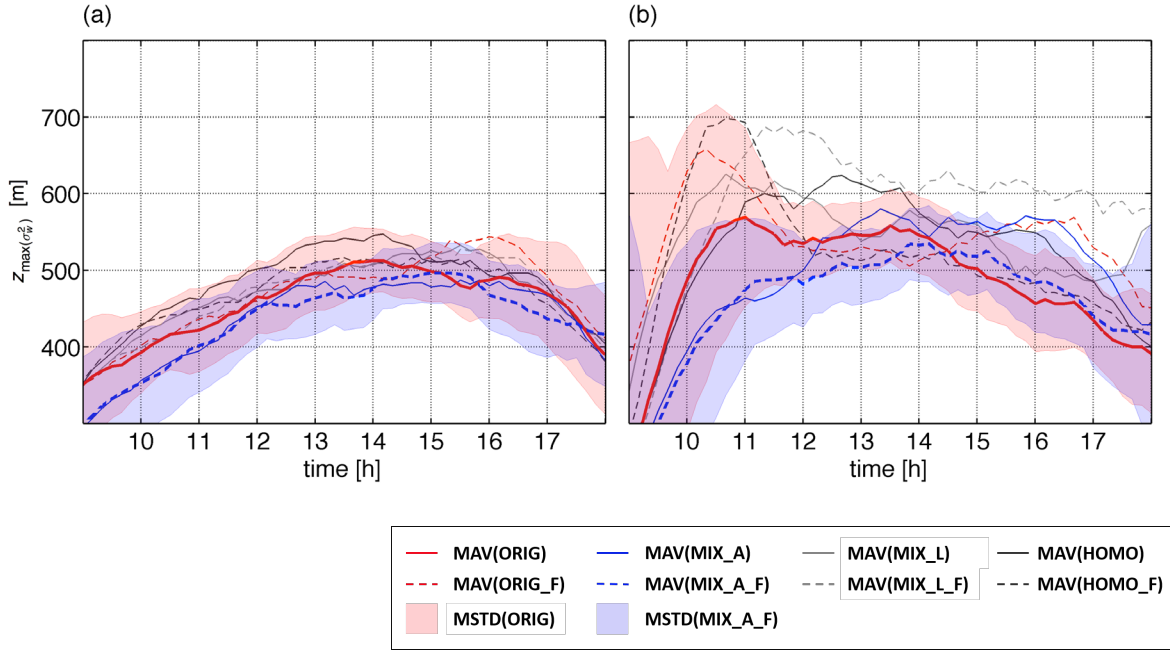
Figure 5-13: Same as Figure 5-12, but for height of maximum variance of vertical wind. The data points used for the moving averages / standard deviations are provided in Figure E-2. The range of the vertical axis in Figure 5-13 covers $5/12 \approx 0.42$ of the range used in Figure 5-12. This accounts for the median ratio between these two characteristic heights as it has been calculated from the simulation results between 9:00 and 18:00 (Table 3-1).

Daytime median of ratios of the two characteristic heights z_i(HF) and $z_{\max(\sigma_w^2)}$ has been calculated to check, if the CBL vertical structure differs between the experiments (Table 5-8). The ratios do not differ a lot, but it is noticeable, that the simulations MIX_A and MIX_A_F have smaller ratios. Thus the bulge of the vertical wind variance is not only located at absolute lower altitudes (Figure 5-13), but also relative within the developing CBL. This could be caused by the lower heat fluxes and the missing river breeze circulations in these simulations.

Table 5-8: Median of the ration $z_{\max(\sigma_w^2)} / z_i$(HF) between 9:00 and 18:00.

	ORIG	ORG_F	MIX_L	MIX_L_F	HOMO_L	HOMO_L_F	MIX_A	MIX_A_F
DAY1	0.40	0.42	0.42	0.41	0.42	0.41	0.39	0.38
DAY2	0.40	0.39	0.42	0.43	0.40	0.41	0.39	0.37

5.4 Conclusions

This chapter investigated the role of topography details for simulating diurnal cycles of free convective boundary layers above the inner-city and harbor area of Hamburg. Model experiments based on modifications of surface classes and topography (Section 5.2.1) have been analyzed (Section 5.3). For the experiments in this chapter all model developments done for METRAS-LES have been included into a recent version of METRAS. This helps to sustain features contributed by this thesis in the M-SYS code for the future.

The preparation of the model experiments lead to interpretation and analysis of orography data (Section 5.1). Additional outcome of this preparation of geographic data, which goes beyond the pure creation of the needed maps (Figure 5-3 and Figure 5-4), can be summarized as follows:

- A new mapping from land use orientated ATKIS Basis-DLM classes to physical classes suitable for simulations with M-SYS has been defined (Appendix D.2).

- An analysis of maps, based on ATKIS and CORINE data, show that on a 50 m grid considerable more grid cells include SGS surface classes for the model domain in Hamburg (Section 5.1.1). This provides a quantitative measure for the additional granularity of the ATKIS data.

- Inconsistencies in the heights of the Elbe could be identified in the digital elevation model ATKIS DGM5. These inconsistencies can easily be overlooked in the visualization of the data for larger domains, but should definitely be corrected for high resolution data usage.

- Distributions of surface classes have been determined for the inner city and harbor area of Hamburg (Table 5-2 and Table 5-4).

The performed topography experiment has the following outcome: The main differences are between the simulations MIX_A / MIX_A_F and all other simulations. Temperatures and horizontal wind speeds at 10 m and sensible heat fluxes in the surface layer are lower in the experiments MIX_A / MIX_A_F compared to all other experiments (Section 5.3.2). Additionally the height of the convective boundary grows at lower rates (Section 5.3.3). This is an effect of the missing thermal circulation systems in the experiments MIX_A / MIX_A_F. The same reduction effect is visible in the land homogenization and mixing experiments (HOMO / HOMO_F, MIX_L / MIX_L_F), but on smaller scales (Table 5-6, Table 5-7).

The physical principle should be the same for the reduction in MIX_L, MIX_L_F, HOMO, HOMO_F, MIX_A and MIX_A_F. There might be two reasons for the different scales. First lower water temperatures than land temperatures could cause that distributing of water cells reduce horizontal temperature gradients more effectively. The second reason could be larger water patches.

6 Overall summary and Outlook

This thesis followed two main topics – investigating questions regarding the urban climate of Hamburg and extension of METRAS for large eddy simulation. The scientific question followed up is than understanding the structure and development of convective boundary layers above Hamburg.

As technical basis the transformation of METRAS-RANS to METRAS-LES is targeted first. The conceptual step for transferring a RANS model into an LES model is applying a different filter (Section 2.3.1). In praxis this means that a SGS model suitable for LES is needed. Simply reducing the grid sizes will not turn a RANS model into an LES model. An example for this is provided in Section 4.3.3: The temperature distribution gained from the LES model has a wider range and a different shape than the temperature distribution from the RANS solution. For METRAS-LES the implemented SGS model is described in Section 3.1.2. A new implicit time integration for the dissipation of SGS TKE has been derived, to stabilize the calculation of the SGS model (Section 3.1.3, Appendix A). Some sensitivity studies suggest that parts of the used closure may contain unneeded complexity (Section 3.3.1) and others show that the TKE parameterization applied in the surface layer, has quite large impact on the filter properties of the closure (Section 4.3.2). A corrected method to prescribing heat fluxes has been implemented METRAS-LES (Section 3.1.4). This model steering is used in model intercomparison and sensitivity studies, which are used to increase the trust in the model and to discover suitable model parameters for simulations of CBL above flat terrain (Chapter 3).

The application of METRAS-LES above heterogeneous non-flat (Section 4.1.4) urban areas is tested in Chapter 4. Here the available surface scheme from METRAS (Section 4.1.2) can be used, which requires a map of surface classes (Section 4.1.3). Reusing of the similarity theory based surface scheme also for LES provides stability dependent calculation of surface exchange processes. But this approach is not without problems, because not all used concepts of surface layer similarity are strictly valid in the LES concept. An example provides the non-applicability of the flux matching concept (Section 4.3.2, Appendix B). The model applications over a simplified map of Hamburg (Figure 4-5) show, that under CBL conditions river breeze circulations likely occur over Hamburg (Section 4.2.3) and that grid scale variations of the surface classes of 10 % of the grid cells are sufficient to trigger independent ensembles (Section 4.3.1).

The simulation of the CBL above the map with simplified surface cover showed interesting interactions with the underlying harbor city, even though the map is obviously quite coarse. This motivates to continue the studies of CBL above Hamburg with refined surface data. For the ATKIS data a finer surface mapping has been defined (Section 5.1.1, Appendix D.2). This mapping METRAS_URBAN_A is not only used for the studies presented in this thesis. Instead it served as starting point for a modified mapping to more than 10 classes, valid for the metropolitan region of Hamburg on coarser grid resolutions (Schlünzen et al. 2012b) and also used by Hoffmann (2012),

Schoetter (2013), Flagg et al. (2014a,b) and Fischer (2014). Modification of map details (Section 5.2) helped to investigate the influence on map details on the CBL. It is found that the heterogeneity provided in the surface class map as well as the orography can be neglected for area averaged analysis of temperature, wind and heat fluxes within the surface layer. But redistribution of water surface creates modification of the model results, which are most likely caused by a reduction of 10 m wind speed by 25 % due to the missing mesoscale circulations (Section 5.3).

In order to bridge the gap between RANS mesoscale modelling and obstacle resolving microscale modelling, the presented modelling with METRAS-LES can only be a first step. Next steps will be maturing the presented simulations by comparison of model results with measurement data. For example one could enlarge the domain to include the Hamburg Weather Mast (Brümmer et al. 2012), which includes turbulence measurements. The near surface processes are very uncertain in the model. Besides looking into fine adjustment of parameters, one should think about how processes can be represented alternatively. Other steps might be nesting METRAS-LES in mesoscale simulations and using the LES results as boundary conditions for obstacle resolving models. This later step seems to be a fundamental task to bring the urban simulations to higher resolutions. Simply increasing the resolution in the current setup will not be sufficient, as larger buildings would need to become resolved. Hence, much additional work will be needed to reach the far-reaching aims formulated on the first pages of this thesis. Both RANS and LES modelling still need improvements. Therefore, the answer to the question if LES is needed or if RANS is sufficient for urban modelling, cannot be given here.

Besides all incompleteness and left over uncertainties, some facts about the urban climate of Hamburg could be found as well: River breeze will likely exist in Hamburg for calm wind, fair weather conditions. In this case a daytime convergence between Alster and Elbe will possibly exist. Related effects should be studied in more details, also with modified atmospheric input and with fine-tuned surface characteristics. In the presented study a relative low water temperature of 17 °C is used. So this might be also a candidate for different settings.

This work is intended to improve the understanding of modelling the atmosphere at the scales needed for investigations of the urban climate. Hopefully, it adds to the related knowledge, as modelling is a useful tool to understand qualitatively and quantitatively how the atmosphere responds to urban areas. Such understanding is needed by urban planners and decision makers to (re)build the cities in a way, which is good for their inhabitants.

Appendix A: Implicit method for dissipation of TKE

A.1 Application to METRAS-LES

The numerical method developed for the calculating of the dissipation term in the SGS TKE equation applied in METRAS-LES (Section 3.1.3) includes the integration of Equation (3.27). Details of the integration are presented below. Equation (3.28) is derived in in Appendix A.1.1 and Equation (3.29) is derived in Appendix A.1.2.

A.1.1 Grid length scale

For the case that l and c_ε are constant, e.g. l is described by the grid length scale $l = \Delta = \left(\Delta x {\cdot} \Delta y {\cdot} \Delta z \right)^{1/3}$ the method explained in Section 3.1.3 requires only the integration of

$$\int_{\hat{\bar{e}}^{n+1}}^{\bar{e}^{n+1}} \left(\hat{\bar{e}}^{n+1} \right)^{-3/2} d\hat{\bar{e}}^{n+1} = -\frac{c_\varepsilon}{l} \int_t^{t+\Delta t} dt \; . \tag{A.1}$$

Solving the integrated equation

$$\frac{1}{\sqrt{\bar{e}^{n+1}}} - \frac{1}{\sqrt{\hat{\bar{e}}^{n+1}}} = \frac{c_\varepsilon}{2l} \Delta t \tag{A.2}$$

for the finial value $\bar{e}^{n+1}$ provides the needed diagnostic Equation (3.28) for the subgrid scale turbulent energy at the end of the time step

$$\bar{e}^{n+1} = \frac{1}{\left(\dfrac{1}{\sqrt{\hat{\bar{e}}^{n+1}}} + \dfrac{c_\varepsilon \Delta t}{2l} \right)^2} = \hat{\bar{e}}^{n+1} \frac{1}{1 + \dfrac{c_\varepsilon \Delta t \sqrt{\hat{\bar{e}}^{n+1}}}{l} + \dfrac{c_\varepsilon^2 \Delta t^2 \hat{\bar{e}}^{n+1}}{4 l^2}} \tag{A.3}$$

which has been implemented into the model.

A.1.2 Atmospheric length scale

For stable conditions the length scale l is modeled according by Equation (3.16) as a function of the Brunt Väisälä frequency and the subgrid scale turbulent energy

$$l = 0.76 \cdot \sqrt{\bar{e}} \, / \, N_{BV} \tag{A.4}$$

Using (A.4) and taking into account that $c_\varepsilon(l)$ is described by Equation (3.24), the differential Equation (3.27) for calculating the dissipation of SGS turbulent kinetic energy writes as

$$\frac{\partial \hat{\bar{e}}^{n+1}}{\partial t} = -\frac{\left(0.19 + 0.74 \dfrac{0.76 \cdot \sqrt{\hat{\bar{e}}^{n+1}} \, / \, N_{BV}}{\Delta} \right) \cdot \left(\hat{\bar{e}}^{n+1} \right)^{3/2}}{0.76 \cdot \sqrt{\hat{\bar{e}}^{n+1}} \, / \, N_{BV}} \tag{A.5}$$

$$\frac{\partial \hat{\bar{e}}^{n+1}}{\partial t} = -0.25 \cdot N_{BV} \cdot \hat{\bar{e}}^{n+1} - 0.74 \cdot \frac{\left(\hat{\bar{e}}^{n+1}\right)^{3/2}}{\Delta} \quad . \tag{A.6}$$

Hence the resulting integral is

$$\Delta t = -\int_{\hat{\bar{e}}^{n+1}}^{e^{n+1}} \frac{1}{0.25 \cdot N_{BV} \cdot \hat{\bar{e}}^{n+1} + \frac{0.74}{\Delta} \cdot \left(\hat{\bar{e}}^{n+1}\right)^{3/2}} d\hat{\bar{e}}^{n+1}$$

$$\Downarrow \quad \text{with} \quad a = N_{BV}/4 \quad \text{and} \quad b = 0.74/\Delta \tag{A.7}$$

$$\Delta t = -\int_{\hat{\bar{e}}^{n+1}}^{e^{n+1}} \frac{1}{ax + bx^{3/2}} dx$$

.

With the help of the solution for the indefinite integral

$$\int \frac{1}{ax + bx^{3/2}} dx = \frac{2\ln(\sqrt{x})}{a} - \frac{2\ln(a + b\sqrt{x})}{a} + const \tag{A.8}$$

provided by Wolfram|Alpha (2010) it can be easily seen that integral (A.7) is solved by

$$\Delta t = \frac{2\ln(\sqrt{\bar{e}^{n+1}})}{a} - \frac{2\ln(a + b\sqrt{\bar{e}^{n+1}})}{a} - \frac{2\ln(\sqrt{\hat{\bar{e}}^{n+1}})}{a} + \frac{2\ln(a + b\sqrt{\hat{\bar{e}}^{n+1}})}{a} \tag{A.9}$$

Solving Equation (A.9) for $\hat{\bar{e}}^{n+1}$ delivers the searched implicit solution (3.29) for the dissipation term as can be seen from a few algebraic transformations:

$$\ln\frac{a + b\sqrt{\hat{\bar{e}}^{n+1}}}{\sqrt{\hat{\bar{e}}^{n+1}}} = \ln\frac{a + b\sqrt{\bar{e}^{n+1}}}{\sqrt{\bar{e}^{n+1}}} - \frac{a}{2}\Delta t$$

$$\Downarrow \quad \text{with} \quad c = \ln\frac{a + b\sqrt{\bar{e}^{n+1}}}{\sqrt{\bar{e}^{n+1}}} - \frac{a}{2}\Delta t \tag{A.10}$$

$$\frac{a + b\sqrt{\hat{\bar{e}}^{n+1}}}{\sqrt{\hat{\bar{e}}^{n+1}}} = \exp(c)$$

$$a = \sqrt{\hat{\bar{e}}^{n+1}}(\exp(c) - b)$$

$$\Downarrow$$

$$\hat{\bar{e}}^{n+1} = \frac{a^2}{(\exp(c) - b)^2}$$

Resubstitution of a, b according Equation (A.7) and resubstitution of c according Equation (A.10) results in

$$e^{n+1} = \frac{\dfrac{N_{BV}^2}{16}}{\left(\exp\left(\ln\dfrac{\frac{N_{BV}}{4} + \frac{0.74}{\Delta}\sqrt{\hat{\overline{e}}^{\,n+1}}}{\sqrt{\hat{\overline{e}}^{\,n+1}}} + \Delta t \dfrac{N_{BV}}{8} \right) - \dfrac{0.74}{\Delta} \right)^2} . \tag{A.11}$$

Which is the second solution implemented in the model (Equation (3.29)).

A.2 Application to MITRAS

The method for integrating the dissipation term developed for METRAS-LES (Section 3.1.3 and Appendix A.1) can be ported to the microscale model MITRAS-RANS. MITRAS uses a different parameterization for the dissipation term than METRAS-LES. Thus the integration of Equation (3.26) needs to be modified:

The turbulence model in MITRAS parameterizes the dissipation by the 3/2 power of the turbulent kinetic energy:

$$\varepsilon = \frac{\left(c_m\right)^3}{\kappa(1 + \kappa/\lambda)\cdot f(Ri)} \cdot \overline{e}^{\,3/2} \tag{A.12}$$

where $\lambda = 100$, $c_m = 0.55$ and $f(Ri) = 1 - 5Ri$ is used for $Ri > 0$ and $f(Ri) = 1$ else. Hence Equation (A.12) can be simplified written as

$$\varepsilon = const\,\frac{\overline{e}^{\,3/2}}{l(Ri)} \tag{A.13}$$

Using Equation (A.13) in Equation (3.26) means that only the simple equation

$$\frac{\partial \rho_0 \alpha^* \hat{\overline{e}}^{\,n+1}}{\partial t} = -\rho_0 \alpha^* c_1 \frac{\left(\hat{\overline{e}}^{\,n+1}\right)^{3/2}}{l(Ri)} \tag{A.14}$$

needs to be solved. ρ_0, α^* and $l(Ri)$ are assumed to be constant within one time step, hence solving the integral

$$\int_{\hat{\overline{e}}^{\,n+1}}^{\overline{e}^{\,n+1}} \left(\hat{\overline{e}}^{\,n+1}\right)^{-3/2} d\hat{\overline{e}}^{\,n+1} = -\frac{c_1}{l(Ri)}\int_t^{t+\Delta t} dt$$

and solving the result for $\overline{e}^{\,n+1}$ provides the an analytic solution for the dissipation of turbulent kinetic energy, which has been implemented into MITRAS:

$$\overline{e}^{\,n+1} = \frac{1}{\left(\dfrac{c_1}{2\cdot l(Ri)}\Delta t + \dfrac{1}{\sqrt{\hat{e}^{\,n+1}}}\right)^2}$$

$$= \frac{1}{\dfrac{c_1^2}{4\cdot l(Ri)^2}\Delta t^2 + \dfrac{c_1}{l(Ri)}\Delta t\,\dfrac{1}{\sqrt{\hat{e}^{\,n+1}}} + \dfrac{1}{\hat{e}^{\,n+1}}}$$

$$= \hat{e}^{\,n+1}\,\frac{1}{\dfrac{c_1^2}{4\cdot l(Ri)^2}\Delta t^2 \cdot \hat{e}^{\,n+1} + \dfrac{c_1}{l(Ri)}\Delta t \cdot \sqrt{\hat{e}^{\,n+1}} + 1}$$

$$(A.15)$$

Appendix B: TKE in the surface layer and flux continuity

It is possible to show that $\bar{e} = u_*^2 / c^2$ (Equation (4.8)) can be used in MITRAS-RANS to ensure that fluxes are continuous between a Monin Obukhov similarity theory based surface layer parameterization and the subgrid scale fluxes calculated from the TKE based RANS closure above. Lopez (2002) showed this for neutral stratification. This derivation is repeated here for the Prandtl-Kolmogorov closure of METRAS-RANS (Schlünzen et al. 2012a, p. 26 – 27) and extended for non-neutral stratification. Further references and a discussion of applicability of the same concept for METRAS-LES are provided in Section 4.3.2.

B.1 Momentum flux matching in METRAS-RANS

For simulations with METRAS-RANS it is important that fluxes are matching at the interface between the first and the second atmospheric grid cell (Lüpkes and Schlünzen 1996). For this matching the limit values of the parameterizations for the surface layer fluxes and those from the subgrid scale model at higher levels need to be equal at the matching height. In the following, equations from the scientific documentation of M-SYS / METRAS-RANS (Schlünzen et al. 2012a) are cited with Sci-doc (x.y).

The desired equality of the momentum fluxes at the interface between the first and the second atmospheric grid layer can be expressed by the limits

$$\lim_{z \downarrow z_p} K \frac{\partial u}{\partial z} \overset{!}{=} \lim_{z \uparrow z_p} K \frac{\partial u}{\partial z} \tag{B.1}$$

Here $\lim_{z \downarrow z_p}$ represents the limit value for the flux formulation from above the surface layer at height z_p, while $\lim_{z \uparrow z_p}$ represents the limit values for the fluxes coming from below z_p at height z_p. It can be written by using the definition of the diffusion coefficients according Sci-doc (3.55) as

$$\lim_{z \downarrow z_p} \left(c_1 l \sqrt{\bar{e}} f(Ri) \cdot \frac{\partial u}{\partial z} \right) = \lim_{z \uparrow z_p} K \frac{\partial u}{\partial z} \tag{B.2}$$

Here c_1 is set to 0.5, the mixing length l is defined according Sci-doc (3.56) and $f(Ri)$ is a short notation for

$$f(Ri) = \begin{cases} (1 - 5Ri) & \text{for} \quad Ri > 0 \\ (1 - 16Ri)^{1/4} & \text{for} \quad Ri \leq 0 \end{cases} \tag{B.3}$$

For the limit value at z_p, $\lim_{z \uparrow z_p}$, the flux can be written with Sci-doc (3.36)

$$\lim_{z \downarrow z_p} \left(c_1 l \sqrt{\bar{e}} \frac{\partial u}{\partial z} f(Ri) \right) = \frac{\kappa u_* z}{\phi_m} \frac{\partial u}{\partial z} \tag{B.4}$$

In METRAS-RANS Equation (B.4) is fulfilled by adjusting the value of e according Equation (4.8). Thus Equation (B.4) is solved for e which is then set in the model:

$$\overline{e}_{z_p} = \left(\frac{\kappa z u_*}{\phi_m f(Ri) c_1 \lim_{z \downarrow z_p} (l)} \right)^2$$

(B.5)

The limit of the mixing length l according Sci-doc (3.65)

$$\lim_{z \downarrow z_p} (l) = \lim_{z \downarrow z_p} \left(\frac{\kappa z}{1 + \kappa (z - z_p)/\lambda} \right) = \kappa z$$

(B.6)

cancels the with the numerator. Therefore, Equation (B.5) can be written as

$$\overline{e}_{z_p} = \frac{u_*^2}{\left(\phi_m (z/L) \cdot c_1 \cdot f(Ri) \right)^2}$$

(B.7)

The general connection (Sci-doc (3.16)) between z/L and Ri

$$Ri = \frac{z}{L} \frac{\phi_h}{\phi_m^2}$$

(B.8)

which also implies $\mathrm{sgn}(Ri) = \mathrm{sgn}(z/L)$, as $\phi_h > 0$, allows to rewrite (B.3) in terms of the stability parameter z/L

$$f(\mathrm{Ri}) = f(z/L) = \begin{cases} (1 - 5zL^{-1}\phi_h\phi_m^{-2}) & \text{for} \quad z/L > 0 \\ (1 - 16zL^{-1}\phi_h\phi_m^{-2})^{1/4} & \text{for} \quad z/L \leq 0 \end{cases}$$

(B.9)

The profile functions in (B.7) and (B.9) are defined with Sci-doc (3.15)

$$\phi_m = \begin{cases} \left(1 - 16zL^{-1}\right)^{-1/4} & \text{for} \quad z/L \leq 0 \\ 1 + 5zL^{-1} & \text{for} \quad z/L > 0 \end{cases}$$

(B.10)

$$\phi_h = \begin{cases} \left(1 - 16zL^{-1}\right)^{-1/2} & \text{for} \quad z/L \leq 0 \\ 1 + 5zL^{-1} & \text{for} \quad z/L > 0 \end{cases}$$

(B.11)

Using Equation (B.10) and Equation (B.11) in Equation (B.9) shows that $f(z/L) = \phi_m^{-1}$, independently of z/L. Therefore f and ϕ_m cancel in Equation (B.7), which simplifies to

$$\overline{e}_{z_p} = \frac{u_*^2}{c_1^2}$$

(B.12)

Equation (B.12) provides momentum flux matching for the Prandtl-Kolmogorov closure regardless of atmospheric stability. This independence from stability is enforced by the choice of the function $f(Ri)$.

B.2   Heat flux matching in METRAS-RANS

The derivation for the heat flux matching

$$\lim_{z\downarrow z_p} K \frac{\partial \theta}{\partial z} \overset{!}{=} \lim_{z\uparrow z_p} K \frac{\partial \theta}{\partial z} \tag{B.13}$$

can be done in analogy to the momentum flux matching (Appendix B.1). Using Sci-doc (3.37) in Equation (B.13) results in

$$\lim_{z\downarrow z_p} K \frac{\partial \theta}{\partial z} = \frac{\kappa u_* \theta_*}{\phi_h} \frac{\partial \theta}{\partial z} \ . \tag{B.14}$$

The formulation of the diffusion coefficients (Sci-doc (3.55)) includes a different formulation of the stability term

$$f(Ri) = \begin{cases} (1-5Ri) & \text{for} \quad Ri > 0 \\ (1-16Ri)^{1/2} & \text{for} \quad Ri \le 0 \ , \end{cases} \tag{B.15}$$

which cancel out the same way, as shown above, due to the stability functions in surface layer (Sci-doc (3.15)).

Therefore, the flux matching can also be forced for the heat fluxes by setting the TKE according to Equation (B.12), which forces the diffusion coefficients to values that cause the same fluxes as those provided by the parameterizations in the surface layer. The same holds true for moisture fluxes, as they use the same stability functions and exchange coefficients as the heat fluxes.

Appendix C: Water temperatures in Hamburg

As parts of this thesis have shown that the water surfaces can have important influences on the atmospheric state for low wind situations, a short overview on available measurements of water temperatures in the metropolitan region of Hamburg is provided here. The short climatological data analysis presented below can serve as a reference to set water temperatures in further modeling studies of the urban climate found in Hamburg.

Among other parameters the "Wassergütemessnetz (WGMN)" operated by the "Institut für Hygiene und Umwelt" monitors water temperatures for the most important waters of Hamburg. The data are provided online[12] for different sites, with a time resolution of 10 min. First data range back to 1988. But not all sites have such long history. The following analysis concentrates on the measurements of water temperatures measured at three different sites in the river Elbe (Blankenese, Bunthaus, Seemannshöft) and one site in the Alster (Lombardsbrücke). Data for sites of small water streams (Ammersbeck, Tarpenbek, Wandse) are not discussed here. The geographical coordinates of the analyzed sites can be found in Table C-1.

Table C-1: Selected measurement sites of the WGMN providing water temperatures for waters in Hamburg. Time period of analyzed data set, location in longitude and latitude and the number of complete days is given.

station	time periode	latitude / longitude	#days with $T_{water(day)}$
Blankenese Elbe	1988-05-01 2010-06-31	53.555925° N 9.804675° W	5 807
Bunthaus Elbe	1988-05-01 2010-06-31	53.461651° N 10.064324° W	4 642
Seemannshöft Elbe	1988-05-01 2010-06-31	53.540186° N 9.880625° W	5 198
Lombardsbrücke Alster	1993-12-03 2010-06-31	53.557134° N 9.997993° W	4 122

Daily (arithmetic) mean values have been calculated from downloaded 10 min values. Days with missing values have been ignored from further analysis, leaving days in corresponding to a range of 11 – 15 years (Table C-1.). Based on these daily mean values, monthly averages have been calculated over the whole available time series for all four stations (Figure C-1). The temperature measured in the Alster seems to be a bit lower than those measured in the Elbe. Possible physical reasons can be a stronger

---

[12] http://www.hamburg.de/wasserguetemessnetz

vertical mixing in the Elbe due to larger flow velocities, or reduced thermal heating caused by shading through the bridge for the Alster site. Nevertheless, all available daily means have been used for calculating the annual averages, regardless if the data for the particular day were available for all four sites or not. Therefore differences between averaged temperatures can also an effect of the different statistical samples. To provide some measure for the uncertainty of the analyzed annual cycle, monthly averaged standard deviation for the water temperature at the Blankenese site have been drawn as error bars in Figure C-1.

Older water temperature measurements taken between 1951-1965 (republished by Rosenhagen et al. 2011) show similar annual cycle and a temperature in the Elbe which is 0.7 °C higher in the annual mean than in the Alster. The summer maximum in this older measurements is 19.8 °C for the Elbe and thus lower than in the recent analysis. This may be due to changed environmental conditions, but possible influences measurement methods or changed locations should be taken into account.

With this analysis of the annual cycle of water temperature in Hamburg the ad hoc chosen water temperature of 17 ° C in the simulation presented in Section 4 and 5 can be seen as characteristic for May or September.
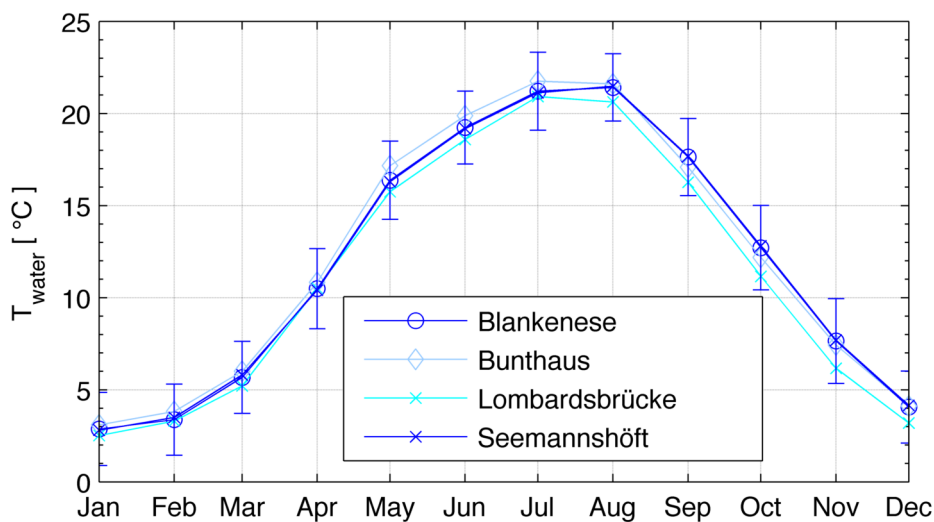
Figure C-1: Monthly mean water temperatures for the rivers Elbe and Alster measured by the WGMN. The error bars show the +/- standard deviation of daily means for the water temperature in Blankenese.

Deviations of the 10 min values from the daily means have been averaged over the whole available time series to create an averaged diurnal cycle (Figure C-2). The shaded areas indicate the corresponding standard deviations. The weak diurnal cycle has also been found for similar analysis for individual seasons (not shown here). The stronger diurnal cycle in the Alster is most likely an effect of weaker vertical exchange through mechanical mixing compared to the Elbe.
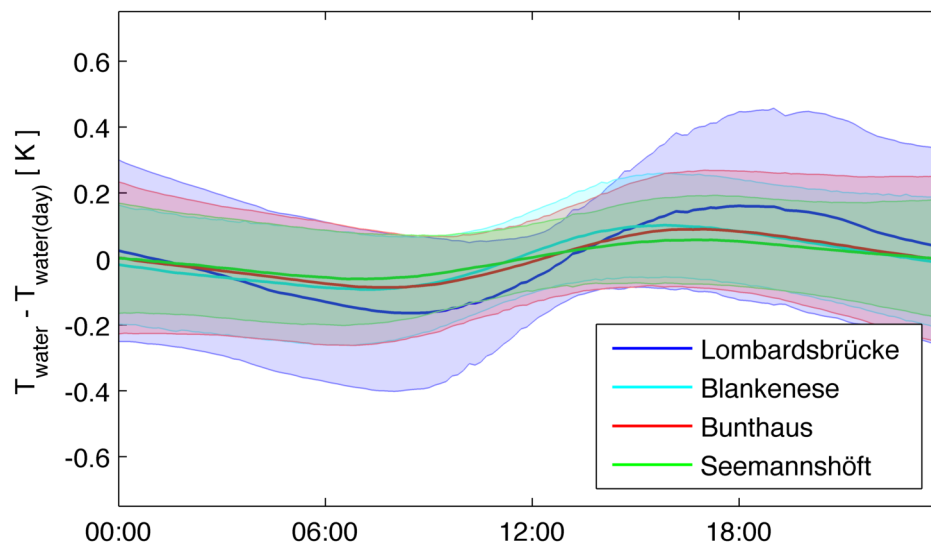
Figure C-2: Annual mean diurnal cycle of water temperature for the rivers Elbe and Alster measured by the WGMN. The shaded areas show the +/- standard deviation of difference to the mean temperature.

The assumption of constant water temperatures made in the simulations in Section 4 and 5 is supported by the weak diurnal cycles, as the uncertainties made by the other model assumptions should have larger effects. Nevertheless, with the presented analysis it would be easy to implement an average diurnal cycle into the model.

Appendix D: Mapping tables for land use data

Land use / surface cover classes have been mapped from the original data sets to a set of surface classes used in the model. The mapping used in Chapter 4 is given in Appendix D.1. The mapping used in Chapter 5 is given in Appendix D.2.

D.1 CORINE data for METRAS-LES - mapping table METRAS_URBAN

Due to the relative small amount of CORINE classes and the dominance of only few classes for the whole model domain (Figure 4-1) the mapping is straight forwards, under the constrain that 10 classes were needed as result. The mapping is only checked for inner city and harbor area of Hamburg. Other regions may need a modified mapping.

Further details about the data and a map can be found in Section 4.1.3.

Table D-1: Mapping of CORINE classes to the classes 0 – 6 in Figure 4 2 (METRAS_URBAN).

METRAS_URBAN		CORINE Land Cover	
#	Description	#	Description
0	Water	511	Water courses
		512	Water bodies
		521	Coastal lagoons
		522	Estuaries
		523	Sea and ocean
1	Mudflat	411	Inland marshes
		412	Peat bogs
		423	Intertidal flats
2	Harbor & industry	121	Industrial or commercial units
		123	Port areas
3	Mixed vegetation	142	Sport and leisure facilities
		211	Non-irrigated arable land
		212	Permanently irrigated land
		221	Vineyards
		241	Annual crops associated with permanent crops
		243	Land principally occupied by agriculture, with significant areas of natural vegetation
		333	Sparsely vegetated areas
		334	Burnt areas
		335	Glaciers and perpetual snow
4	Meadows	132	Dump sites
		231	Pastures
5	Traffic	122	Road and rail networks and associated land
		124	Airports
		131	Mineral extraction sites
		133	Construction sites
		142	Sport and leisure facilities
		222	Fruit trees and berry plantations
		223	Olive groves
		321	Natural grasslands
		331	Beaches, dunes, sands
		332	Bare rocks
6	Bushes	141	Green urban areas
		142	Sport and leisure facilities
		222	Fruit trees and berry plantations
		321	Natural grasslands
		324	Transitional woodland-shrub

Table D-2: Mapping of CORINE classes to the classes 7-9 in Figure 4-1 (METRAS_URBAN).

METRAS_URBAN		CORINE Land Cover	
#	Description	#	Description
7	Mixed forest	244	Agro-forestry areas
		311	Broad-leaved forest
		312	Coniferous forest
		313	Mixed forest
8	Inner city	111	Continuous urban fabric
9	Urban	112	Discontinuous urban fabric

D.2 ATKIS data for METRAS-LES - mapping table METRAS_URBAN_A

The details of the ATKIS data allows to draw a detailed map (Figure 5-1) of the innercity of Hamburg at the model resolution from 50 m, even after aggregation of land use / surface cover classes. The mapping METRAS_URBAN_A from ATKIS to model classes, includes subjective expert judgment of the predominant physical function of classes occurring in the ATKIS data set. This judgment is needed as the ATKIS data are classified according usage, which is not always a well suited classification for numerical modelling. A generalization of the METRAS_URBAN_A mapping to other regions might be possible for most classes. However, due to the subjective and tailored nature of the classification process, required for both the original ATKIS classification and for the remapping METRAS_URBAN_A, careful cross checks should be performed prior using the METRAS_URBAN_A mapping for other model domains.

Further details about the data and a map can be found in Section 5.1. Example locations are given in Table E-1 to E-3. Judgments have been done on more than one location. Some of the mapped ATKIS classes do not exist in the used model domain, Mapping for this classes are given without an example location.

Table D-3: Mapping of ATKIS classes to the classes 0 – 1 in Figure 5-1.

METRAS_URBAN_A		ATKIS®-Basis-DLM			Example	
#	Description	#	Description		Location	
			Translation	Orig. German	Longitude	Latitude
0	Water	2314	Sedimentation tank	Absetzbecken	9° 55' 6.643" E	53° 29' 0.157" N
		2345	Swimming pool	Schwimmbecken	10° 3' 56" E	53° 32' 55.708" N
		3402	Port basin	Hafenbecken	10° 0' 53.735" E	53° 31' 54,25" N
		5101	River	Strom, Fluss, Bach	9° 59' 30.2 "E	53° 32' 20.679" N
		5102	Canal	Kanal	10° 1' 56,976" E	53° 33' 3,753" N
		5103	Canal	Kanal (Wasser-wirtschaft)	10° 4' 34.267" E	53° 30' 3.744" N
		5104	Tidal creek	Priel	10° 6' 53" E	53° 28' 35.191" N
		5105	Spring	Quelle	10° 2' 37.703" E	53° 35'14.8" N
		5112	Inland lake	Binnensee	10° 0' 43.221" E	53° 34' 27.566" N
		5304	Lock chamber	Schleusenkammer	9° 59' 4.933" E	53° 28' 53.514" N
		5372	Tide lock	Kammerschleuse	9° 52' 5.967" E	53° 31' 44.896" N
1	Mudflat	4106	Swamp	Sumpf, Ried	10° 2' 10.524" E	53° 28' 38,991" N
		4111	Wet ground	Nasser Boden	10° 2' 45.797" E	53° 28' 21.509" N
		4181	Swamp: grass	Sumpf: Gras	10° 0' 16.295" E	3° 33' 30.599" N

Table D-4: Mapping of ATKIS classes to the classes 2 – 4 in Figure 5-1.

METRAS_URBAN_A		ATKIS®-Basis-DLM			Example	
#	Description	#	Description		Location	
			Translation	Orig. German	Longitude	Latitude
2	Harbor and Industry	2112	Industrial area	Industriefläche	10° 1' 10.758" E	53° 32' 40.802" N
		2123	Refinery	Raffinerie	9° 57'25.021"E	53° 30' 48.488" N
		2124	Dockyard	Werft	9° 57' 48.742" E	53° 32' 22.643" N
		2126	Power plant	Kraftwerk	9° 57' 0.743" E	53° 29' 28.273" N
		2127	Transformer station	Umspannstation	9° 58' 4.98" E	53° 30' 47.475" N
		2128	Headgear	Förderanlage	9° 58' 9.907" E	53° 30' 52.153" N
		2129	Clarification plant	Kläranlage	9° 56' 32.778" E	53° 32' 9.483" N
		2131	Exhibition area	Ausstellungs-gelände	9° 58' 42.818" E	53° 33' 44.22" N
		2133	Heating plant	Heizwerk	9° 46' 23.74" E	53° 35' 44.477" N
		2134	Water works	Wasserwerk	Not available in used data set.	
		2135	Waste treatment plant	Abfallbehand-lungsanlage	10° 7 '13.769" E	53° 35' 4.714" N
		3301	Airport	Flughafen	9° 59' 21.956" E	53° 31' 18.683" N
		3302	Airfield	Flugplatz	9° 56' 38.745" E	53° 31' 38.297" N
		2317	Chimney	Schornstein	9° 59' 59.647" E	53° 29' 9.542" N
		2323	Dock	Dock	9° 58' 31.506" E	53° 32' 12.34" N
		5373	Flood barrier	Sperrwerk	Not available in used data set.	
3	Mixed vegetation	2132	Market garden	Gärtnerei	10° 1' 32.274" E	53° 35 '31.128" N
		2202	Leisure facility	Freizeitanlage	10° 3' 54.692" E	53° 33' 17.463" N
		2211	Open-air theater	Freilichttheater	9° 58' 59.339" E	53° 31' 6.117" N
		2212	Outdoor museum	Freilichtmuseum	9° 59' 0.212" E	53° 31' 3.123" N
		2223	Shooting range	Schießstand	9° 59' 10.871" E	53° 31' 2.112" N
		2225	Zoo	Zoo	10° 3' 24.549" E	53° 30' 50.9" N
		2228	Camping ground	Campingplatz	9° 59' 24.428" E	53° 30' 36.89" N
		2302	Dump	Halde	10° 7' 25.557" E	3° 26' 18.517" N
		4101	Farmland	Ackerland	10° 2' 8.802" E	53° 28' 55.472" N
		4102	Grassland	Grünland	10° 2' 49.272" E	53° 29' 56.41" N
		4103	Garden	Gartenland	9° 57' 18.349" E	53° 36' 0.352" N
		4109	Special crops	Sonderkultur	9° 52' 20.344" E	53° 30' 16.809" N
		4150	Nursery garden	Baumschule	9° 57' 3.33" E	53° 33' 40.42" N
		5371	Pumping station	Schöpfwerk	9° 56' 30.454" E	53° 38' 19.762" N
4	Meadows	2122	Disposal site	Deponie	10° 1' 48.349" E	53° 30' 40.939" N
		2222	Sports ground	Sportplatz	9° 59' 58.707" E	53° 30' 50.858" N
		2230	Golf course	Golfplatz	10° 4' 32.461" E	53° 30' 28.316" N
		4105	Moor, bog	Moor, Moos	10° 10' 48.019" E	53° 43' 18.772" N
		5370	Sluice	Siel	10° 3' 0.99" E	53° 34' 25.706" N

Table D-5: Mapping of ATKIS classes to the classes 5 – 9 in Figure 5-1.

METRAS_URBAN_A		ATKIS®-Basis-DLM			Example	
#	Description	#	Description		Location	
			Translation	Orig. German	Longitude	Latitude
5	Traffic	2121	Mining industry	Bergbaubetrieb	10° 3' 44.14" E	53° 34' 12.776" N
		2301	Daylight mining	Tagebau	9° 59' 50.008" E	53° 34' 34.112" N
		3101	Street	Straße	10° 7' 46.09" E	53° 31' 43.219" N
		3103	Plaza	Platz	9° 59' 39.347" E	53° 33' 8.568" N
		3201	Railway track	Schienenbahn	10° 1' 46.229" E	53° 33' 39.832" N
		3303	Runway	Rollbahn	9° 59' 56.752" E	53° 37' 47.066" N
		3304	Airport ramp	Vorfeld	10° 0' 5.84" E	53° 38' 2.396" N
		3501	Railway station area	Bahnhofsanlage	9° 56' 18.154" E	53° 33' 42.226" N
		3503	Transport nodes	Verkehrsknoten	10° 1' 51.489" E	53° 31' 6.287" N
		3514	Bridge	Brücke	9° 58' 59.087" E	53° 32' 2.362" N
		4120	Vegetation-free areas	Vegetationslose Fläche	9° 55' 1.341" E	53° 30' 27.06" N
		4160	Vegetation-free: stones, gravel	vegetationslos: Steine, Schotter	9° 58' 0.747" E	53° 33' 49.526" N
		4161	Vegetation-free: sand	Vegetationslos: Sand	10° 15' 21.105" E	53° 25' 17.749" N
		4162	Vegetation-free: boulder	Vegetationslos: Geröll	9° 54' 16.635" E	53° 37' 16.846" N
		5303	Watergate	Schleuse	10° 3' 53.853" E	53° 31' 47.473" N
6	Bushes	2201	Sports grounds	Sportanlage	10° 5' 19.033" E	53° 33' 45.724" N
		2213	Cemetery	Friedhof	10° 3' 14.011" E	53° 37' 39.778" N
		2224	Bath	Schwimmbad	9° 57' 52.969" E	53° 34' 23.008" N
		2226	Recreation park	Freizeitpark	9° 56' 15.038" E	53° 36' 52.998" N
		2227	Green space	Grünanlage	9° 58' 16.039" E	53° 34' 2.606" N
		4104	Heathland	Heide	9° 51' 10.668" E	53° 27' 24.024" N
		4107	Forest	Wald, Forst	9° 53' 49.235" E	53° 34' 57.47" N
		4108	Wood	Gehölz	9° 59' 37.963" E	53° 31' 12.995" N
		4151	Fruit tree plantation	Obstbaum-plantage	Not available in used data set.	
		4177	Deciduous forest	Laubwald – Wald	Not available in used data set.	
		4178	Mixed forest	Mischwald – Wald	Not available in used data set.	
		4179	Coniferous forest	Nadelwald –Wald	Not available in used data set.	
		4180	Swamp: bushes, shrubbery	Sumpf: Büsche, Sträucher	Not available in used data set.	
		4182	Swamp: hardwood	Sumpf: Laubholz	Not available in used data set.	
		4187	Deciduous forest – grove	Laubwald – Gehölz	Not available in used data set.	
		4188	Mixed forest – grove	Mischwald – Gehölz	Not available in used data set.	
		4189	Coniferous forest – grove	Nadelwald – Gehölz	Not available in used data set.	
7	Suburban	2111	Open building development	Offene Bebauung	10° 0' 50.269" E	53° 34' 37.353" N
		3502	Motorway service area	Raststätte	10° 1' 39.773" E	53° 29' 6.65" N
8	Urban	2113	Area with mixed use	Fl. gemischter Nutzung	9° 59' 35.981" E	53° 33' 16.343" N
9	Urban compact	2114	Area with functional use	Fl. besond. funktionaler Prägung	9° 59' 10.359" E	53° 34' 6.193" N
		2221	Stadium	Stadion	9° 58' 8.147" E	53° 33' 22.106" N
		4199	Currently indefinable area	Fläche zz. Unbestimmbar	9° 59' 53.658" E	53° 32' 26.677" N
		2150	Industrial area: shopping mall	Industriefläche: Einkaufszentren	Not available in used data set.	

Appendix E: Moving average of characteristic heights

In order to demonstrate that the 2 hour windowing is appropriate for the moving averages used in Section 5.3.3, plots are reproduced here with inclusion of all instantaneous values for the characteristic heights. Moving averages are only shown for the four simulations including topography to avoid overloading the figures.
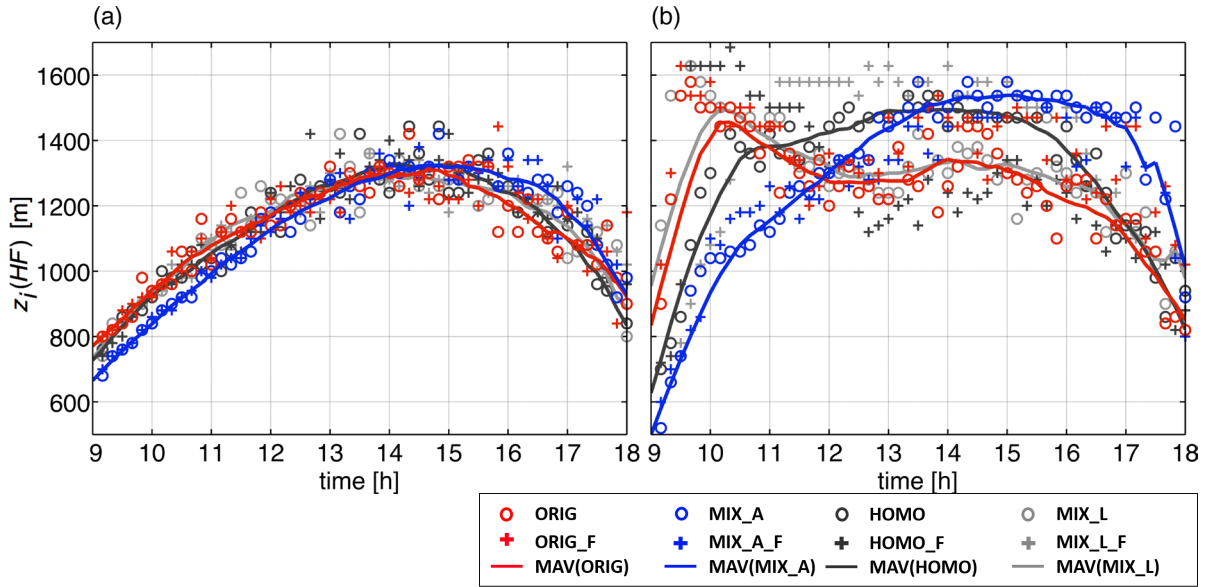
Figure E-1: Same as Figure 5-12 but showing the individual characteristic heights used to calculate the moving averages, leaving out the standard deviation and the moving averages for the experiments with flat terrain.
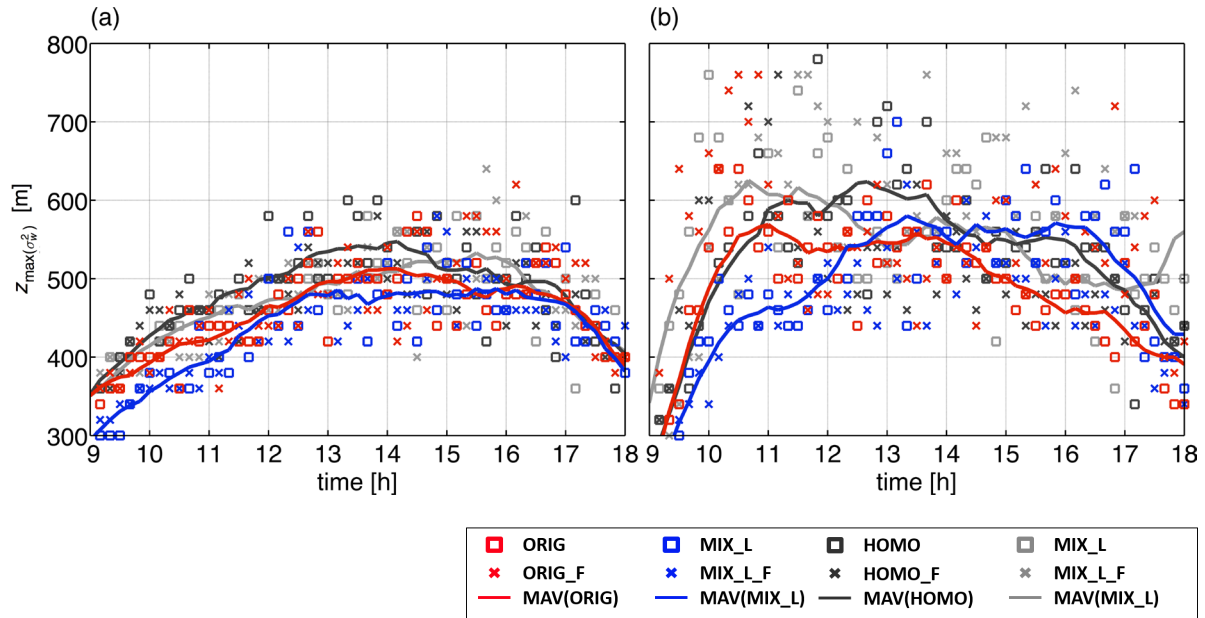
Figure E-2: Same as Figure 5-13 but showing the individual characteristic heights used to calculate the moving averages, leaving out the standard deviation and the moving averages for the experiments with flat terrain.

Appendix F: Scientific software development for M-SYS

Theoretical concepts for validation of regional atmospheric models exist and have been developed with and applied to the Multiscale Model System M-SYS (Schlünzen 1997; Panskus 2000; Dierer 1997; Fock et al. 2008). Additional to such domain/application specific quality assurance strategies generic procedures for sustainable scientific software development exits (e.g. Aruliah et al. 2012, Rouson et al. 2011). Both, specific and generic quality strategies, need to be combined to create a trustable code base for reproducible scientific investigations. One of the desired quality goals is usability of scientific software. Required efforts for developing research tools are always competing with the available time for deploying these tools to gain new knowledge. Both, scientific utilization of tools and their development are of equal importance for the overall research outcome. During the work on this thesis some contributions to the software toolkit of the Multiscale Model System M-SYS have been made, which are not obvious from presented content in the other parts of this thesis, and thus shortly summarized below.

Formerly, visualization of M-SYS results has been based either on a Fortran (Schlünzen et al. 1996b) or a GrADS (Schröder 2007b) based plotting program. Specialized Fortran programs were the main tool for further analyses. These tools have been served as standard model analysis in many studies, but lack of interactivity. Working on border cases of the model application range, i.e. exploring its behavior when switching from RANS to LES mode, suggested to make the simulation analysis more flexible.[13] Starting from 6 routines[14] from Fock (2007), a generic MATLAB toolbox for the Multiscale Model System M-SYS has been developed (Fock 2012) to enable more interactive exploration of model results. This M-SYS interface to a third generation programming became widely used in many newer M-SYS applications (e.g. Gierisch 2011, Linde 2011, Hoffmann 2012, Philipp 2013, Schultze 2013 and Salim et al. 2013). Examples for included functionality are import and visualization tools for all M-SYS output files, calculation of derived quantities, topography manipulation tools, organization of M-SYS data specific data structures and a model sensitivity test according Schlünzen and Reinhardt (2007). Examples and help text are available, as well as a style guide (Fock and Gierisch 2014). The code of this toolbox is of comparable size to the three-dimensional model METRAS, if the higher formal order of the used programming languages are taken into account (Table F-1 and Table F-2). The developed MATLAB toolbox aims to enrich and accelerate the workflow for analyzing simulation results.

---

[13] Similar to the demands for analysis tools suitable for LES model data, targeted here, there are special demands for analysis tools suitable to gather experimental validation data for LES model results (e.g. Fischer 2011).

[14] MemiWiki 2008-03-14: http://goo.gl/X2kePK available on request 2014-06-17.

Table F-1: Code size of memi-matlab-toolbox (trunk rev 686, 2012-12-10), analyzed
with cloc v1.56 (http://cloc.sourceforge.net). The 3rd generation scale factor was
used unmodified, e.g. has the values which come along with cloc v1.56.

Language	Files	Blank lines	Comment lines	Code lines	3rd gen. Scale	3rd gen. equivalent code lines
MATLAB	153	1997	4 246	10 028	4	40 112
HTML	91	755	447	2 684	1.9	5 100
XML	2	5	9	71	1.9	135
C	1	10	29	45	0.77	35
Sum	247	2 767	4 731	12 828	3.54	45 381

Table F-2: Code size of METRAS/MESIM (trunk rev 843, 2012-12-10), analyzed with
cloc v1.56 (http://cloc.sourceforge.net). The 3rd generation scale factor was used
unmodified, e.g. has the values which come along with cloc v1.5.6.

Language	Files	Blank lines	Comment lines	Code lines	3rd gen. scale	3rd gen. equivalent code lines
Fortran 90	489	517	53 012	55 242	1.00	55 242
bash	2	1	734	1 317	3.81	5 018
make	1	2	756	1 014	2.50	2 535
C	3	68	90	389	0.77	300
csh	1	2	81	190	3.81	724
sh	2	0	76	140	3.81	533
Sum	498	590	54 749	58 292	1.10	64 352

To ease the work with the model code customized a collection of text editor
extensions[15] has been created, which allows faster handling of model sources. One
example would be the search function memi_grep.el[16], which is widely used in M-SYS
development community and from associated ocean modelers. To improve the
reproducibility of results and to increase development speed more mainstream source
code management tools have been added to the M-SYS development process.

---

[15] https://bitbucket.org/bhf/bhf_dotemacs accessible 2014-05-01
[16] http://goo.gl/8uJZnY accessible 2014-05-01

List of Simulations

Name	Color	Position	Content
CBL_ND	—	Section 3.3.1, p. 30	Sensitivity SGS closure
CBL_DN	—		
CBL_104	—	Section 3.3.3, p. 37	Sensitivity vertical grid
CBL_052	—		
CBL_036	—		
CBL_M	—	Section 3.2.3, p. 25	Intercomparison, METRAS/PALM
CBL_P	—		
CBL_CDF	—	Section 3.3.2, p. 35	Sensitivity numerical methods
CBL_ENO	—		
HH_CORINE	—	Sections 4.2.2, 4.2.3, p. 51	LES above idealized city, overview and reference run
HH_NOISE	—	Section 4.3.1, p. 56	Sensitivity land use variation
HH_TKE_0.1	None	Section 4.3.2, p. 58	Sensitivity TKE in surface layer
HH_TKE_0.3			
HH_TKE_0.5			
HH_TKE_1.0			
HH_LES	—	Section 4.3.3, p. 62	Sensitivity on SGS model and on using LES or RANS approach
HH_RANS	—		
HH_PCL	—		
ORIG	--	Section 5.2.1, p. 69	Sensitivity on detailed surface classes, main water bodies and orography
ORIG_F	—		
MIX_L	—		
MIX_L_F	--		
HOMO	—		
HOMO_F	--		
MIX_A	—		
MIX_A_F	--		

List of Figures

List of Tables

List of relevant symbols and parameters

Latin symbols

c_ε [-]   Dissipation coefficient for SGS turbulent kinetic energy

c_s [J kg^{-1}K^{-1}]   Specific heat capacity of soil

$\overline{e}$ [m^2 s^{-2}]   SGS turbulent kinetic energy

$\overline{e}^{\,n+1}$ [m^2 s^{-2}]   SGS turbulent kinetic energy at end of spitted timestep

$\hat{\overline{e}}^{\,n+1}$ [m^2 s^{-2}]   Provisional SGS turbulent kinetic energy during
                                                    spitted time step

F_1 [m s^{-2}]   Divergence of SGS momentum flux

F_2 [m s^{-2}]   Divergence of SGS momentum flux

F_3 [m s^{-2}]   Divergence of SGS momentum flux

F_χ [? s^{-1}]   Divergence of SGS flux of scalar quantity, i.e. of heat
                                                    and moisture fluxes

E [W m^{-2}]   Latent heat flux

H [W m^{-2}]   Sensible heat flux

j [-]   Index for SGS surface class

K [m^2 s^{-1}]   Diffusion coefficient for SGS momentum flux

K_χ [m^2 s^{-1}]   Diffusion coefficient for SGS heat flux

k_s [m^2 s^{-1}]   Thermal diffusivity of soil

l [m]   Characteristic length scale

L [m]   Obukhov length

N_{BV} [s^{-1}]   Brunt-Väisälä frequency

P   [kg m^{-2} s^{-1}]   Precipitation rate

p_0 [Pa]   Height depending constant background pressure

p_1 [Pa]   Thermal pressure deviation

p_2 [Pa]   Dynamic pressure deviation

q_* [kg kg^{-1}]   Specific humidity scale for surface layer

$\overline{Q}_{\overline{\chi}}$ [? s^{-1}]   Sources and sinks of scalar quantity $\overline{\chi}$

Ri [-]   Richardson number

$\overline{u}$ [m s^{-1}]   West east component of wind vector

u_p [m s-1]   Wind speed at first atmospheric model level

u_* [m s^{-1}]   Friction velocity

$\overline{v}$ [m s^{-1}]   South north component of wind vector

$\vec{v}$ [m s^{-1}]   Wind vector

$\overline{w}$ [m s^{-1}]   Vertical wind component

$(\dot{x}^1, \dot{x}^2, \dot{x}^3)$ [m]   Model coordinates (terrain following and streched)

(x, y, z) [m]   Cartesian coordinates

z_a [m]   Height of lowest absorbing layer

z_p [m]   Height of first atmospheric grid level

z_0 [m]   Roughness length

z_i [m]   Boundary layer height

$z_i(\mathrm{HF})$ [m]   Height of minimum of resolved heat flux

$z_{\max(\sigma_\theta^2)}$ [m]   Height of second maximum of temperature variance

$z_{\max(\sigma_w^2)}$ [m]   Height of maximum of vertical wind variance

$z_i(\mathrm{Ri})$ [m]   Height of null of Richardson number

z_s [m]   Height of the surface

z_t [m]   Top height of the model domain

Greek symbols

$\alpha^* = \dfrac{\partial x}{\partial \dot{x}^1} \dfrac{\partial y}{\partial \dot{x}^2} \dfrac{\partial z}{\partial \dot{x}^3}$ [-]   Grid transformation coefficient

α	$[\ \mathrm{m\ m^{-1}}\ ]$	Bulk soil water availability
Γ	$[\ \mathrm{K\ m^{-1}}\ ]$	Vertical gradient of potential temperature
Δ	$[\ \mathrm{m}\ ]$	Characteristic grid length scale
Δt	$[\ \mathrm{s}\ ]$	Length of time step
Δx	$[\ \mathrm{m}\ ]$	Grid spacing in west-east direction
Δy	$[\ \mathrm{m}\ ]$	Grid spacing in south-north direction
Δz	$[\ \mathrm{m}\ ]$	Vertical grid spacing
ε	$[\ \mathrm{m^2\ s^{-3}}\ ]$	Dissipation rate of SGS turbulent kinetic energy
η	$[\ \mathrm{m}\ ]$	Vertical coordinate in terrain following system
θ	$[\ \mathrm{K}\ ]$	Potential temperature
θ_p	$[\ \mathrm{K}\ ]$	Potential temperature at first atmospheric model level
θ_{sfc}	$[\ \mathrm{K}\ ]$	Potential temperature at the surface
θ_*	$[\ \mathrm{K}\ ]$	Temperature scale for surface layer
ν	$[\ \mathrm{J\ (K\ s\ m)^{-1}}]$	Kinematic viscosity of air
χ	$[\ ?\ ]$	Generic substitute for scalar variable
ρ	$[\ \mathrm{kg\ m^{-3}}\ ]$	Density
ρ_0	$[\ \mathrm{kg\ m^{-3}}\ ]$	Large scale density
σ_w^2	$[\ \mathrm{m\ s^{-2}}\ ]$	Variance of vertical wind speed
σ_θ^2	$[\ \mathrm{K^2}\ ]$	Variance of potential temperature
φ	$[\ ^\circ\ ]$	Latitude
ϕ	$[\ -\ ]$	Profile function for momentum
ϕ_χ	$[\ -\ ]$	Profile function for scalar quantities
ψ	$[\ -\ ]$	Stability function for momentum
ψ_χ	$[\ -\ ]$	Stability function for scalar quantities

Parameters

$c_p = 1004.67$ J kg^{-1} K^{-1} Specific heat capacity of dry air at constant pressure

$c_k = 0.1$ Proportionality constant in Deardorff SGS model

$c_1 = 0.5$ Parameter for SGS TKE in surface layer [17]

$g = 9.81$ m s^{-2} Earth's gravitational acceleration

$l_v = 2.5 \cdot 10^6$ J kg^{-1} Latent heat of vaporization of water

$R = 287.04$ J kg^{-1} K^{-1} Specific gas constant of dry air

$R_v = 461.5$ J kg^{-1} K^{-1} Specific gas constant of water vapor

$\Omega = 7.292 \cdot 10^{-5}$ rad s^{-1} Earth's angular speed of rotation

$\kappa = 0.4$ Von Kármán constant [18]

$\rho_{water} = 1000$ kg m^{-3} Density of liquid water

---

[17] The value is uncertain and suitable for model tuning (Section 4.3.2).
[18] Baumert (2013) formulated a turbulence theory, which provides a theoretical value $\kappa = (2\pi)^{-1/2} = 0.399$ for the traditionally used $\kappa = 0.4$.

List of relevant abbreviations and names

ATKIS   Amtliches   Topographisch-Kartographische   Informationssystem
               (Official Topographical Cartographic Information System)

AROME   Applications de la Recherche à l'Opérationnel à Méso-Echelle
               (Applications of Research to Operations at Mesoscale)

BCCS   Bergen center for computational science

CBL   Convective boundary layer

CFD   Computational fluid dynamics

CLESM   Conventional large eddy simulation model

cloc   Count lines of code

CORINE   Coordination of information on the environment (programme of the
               Commission European)

DGM5   Digitales Geländemodell 5 m (digital elevation model)

DKRZ   Deutsches Klimarechenzentrum (German Climate Computing Center)

DLM   Digitales Landschaftsmodell (digital landscape model)

DNS   Direct numerical simulation

FAST3D-CT   LES model for contaminant transport

FITNAH   Flow over Irregular Terrain with Natural and Anthropogenic Heat
               Sources (mesoscale model)

FFT   Fast Fourier transform

GEM-LAM   Global Environmental Multiscale – Local Area Model

GIS   Geographic information system

GrADS   Grid Analysis and Display System

LES   Large eddy simulation

LST   Local solar time

SGS   Subgrid scale

SRTM   Shuttle Radar Topography Mission

TKE	Turbulent kinetic energy
RANS	Reynolds averaged Navier Stokes
PALM	Parallelized large-eddy simulation model
MATLAB	Matrix laboratory (commercial programming language)
MAV	Moving average
MECTM	Mesoscale Chemistry Model
METRAS	Mesoscale transport and stream model
METRAS-PCL	METRAS for personal computer operated under Linux
METRAS_URBAN	Surface class mapping (Section 4.1.3)
METRAS_URBAN_A	Surface class mapping (Section 5.1.1)
MeM	Mesoscale model
MESIM	Mesoscale sea ice model
MICTM	Microscale Chemistry Model
MiM	Microscale model
MITRAS	Microscale transport and stream model
M-SYS	Multiscale Model System
NORCOWE	Norwegian Center for Offshore Wind Energy
NetCDF	Network Common Data Form
UTC	Universal Time Coordinated
VDI	Verein Deutscher Ingenieure (association of German engineers)
WGMN	Wassergütemessnetz (water quality measurement network)

References

AdV – Arbeitsgemeinschaft der Vermessungsverwaltungen der Länder der Bundesrepublik Deutschland (2003): ATKIS – Objektartenkatalog Basis-DLM. Amtliches Topographisch – Kartographisches Informationssystem ATKIS. Stand 01.07.2003. Version 3.2.

AdV – Arbeitsgemeinschaft der Vermessungsverwaltungen der Länder der Bundesrepublik Deutschland (2009a): ATKIS® Digitales Basis-Landschafts-modell – Basis-DLM. Data acquired 2009-03-12 from "Landesbetrieb Geo-information und Vermessung, Freie und Hansestadt Hamburg".

AdV – Arbeitsgemeinschaft der Vermessungsverwaltungen der Länder der Bundesrepublik Deutschland (2009b): ATKIS® Digitales Geländemodell 5m. Data acquired 2009-03-12 from "Landesbetrieb Geoinformation und Vermessung, Freie und Hansestadt Hamburg".

AMS – American Meteorological Society (2000): Obukhov length. Glossary of meteorology. http://goo.gl/oYQGy0 accessible 2013-10-16.

Ansorge C (2009): Spectral properties of a free convection model experiment with METRAS-LES. Bachelorarbeit. Meteorologisches Institut Universität Hamburg. 37 pp. http://goo.gl/ZK2Xv accessible 2012-11-13.

Arakawa A (1972): Design of the UCLA general circulation model. Numerical simulation of weather and climate. Technical report no. 7124. 116 pp. http://goo.gl/4hZXs accessible 2012-12-04.

Arnfield AJ (2003): Two decades of urban climate research: a review of turbulence, exchanges of energy and water, and the urban heat island. International Journal of Climatology. 23: 1–26. http://doi.org/bcmxjg

Aruliah D, Brown CT, Chue Hong NP, Davis M, Guy RT, Haddock SHD, Huff K, Mitchell I, Plumbley M and Waugh B (2012): Best practices for scientific computing. arXiv:1210.0530 [cs.MS]. http://arxiv.org/abs/1210.0530

Arya SP (1995): Atmospheric boundary layer and its parameterization. In Cermak JE, Davenport AG, Plate EJ and Viegas DX (eds.): "Wind and Climate in Cities". Kluwer Academic Publishers. Dordrecht. 41–66. ISBN: 0-7923-3202-4

Augustin W, Heuveline V, Meschkat G, Schlünzen KH and Schroeder G (2008): OpenMP Parallelization of the METRAS Meteorology Model: Application to the America's Cup. In Nagel WE, Kröner D and Resch M (eds.): "High Performance Computing in Science and Engineering `07". Springer Berlin Heidelberg, 547–559. http://dx.doi.org/10.1007/978-3-540-74739-0_37

Bakan S (1994): Eine einfache Strahlungsparametrisierung für ein mesoskaliges Modell. Internal report. Max-Planck-Institut for Meteorology. 37 pp.

Basu S, Vinuesa J-F and Swift A (2008): Dynamic LES modeling of a diurnal cycle. Journal of Applied Meteorology. 47: 1156–1174. http://doi.org/dwgpbp

Baumert HZ (2013): Universal equations and constants of turbulent motion. Physica Scripta. 155: 14001–14012. http://doi.org/sm5

Bechtel B and Schmidt KJ (2011): Floristic mapping data as a proxy for the mean urban heat island. Climate Research. 49: 45–58 http://dx.doi.org/10.3354/cr01009

Berlin Senatsverwaltung für Stadtentwicklung (2011): Stadtentwicklungsplan Klima urbane Lebensqualität im Klimawandel sichern. 79 pp. http://goo.gl/Jg4t9 accessible 2012-12-09. ISBN: 978-3-88961-322-6

Bhumralkar CM (1975): Numerical experiments on the computation of ground surface temperature in an atmospheric general circulation model. Journal of Applied Meteorology. 14: 1246–1258. http://doi.org/ds4w7j

Bigalke K, Ahrens D and Rau M (2008): Synthetische Ausbreitungsklassenstatistiken zur Verwendung in Immissionsprognosen – Eine Alternative zu "klassischen" Übertragungsverfahren. Gefahrstoffe – Reinhaltung der Luft. 68: 326–333. ISSN: 0949-8036

Birnbaum G (1998): Numerische Modellierung der Wechselwirkung zwischen Atmosphäre und Meereis in der arktischen Eisrandzone. Berichte zur Polarforschung. Bremerhaven. Alfred Wegener Institute for Polar and Marine Research. 268. 160 pp. http://goo.gl/1PcWl accessible 2013-02-17.

Bock K-H, Brauner R, Dentler F-U, Erdmann H, Günther J, Kresling A and Seifert W (2002): Seewetter. Das Autorenteam des Seewetteramtes. DSV-Verlag. 388 pp. ISBN: 3-88412-367-X

Bohnenstengel SILD (2012): Can a simple locality index be used to improve mesoscale model forecasts? Dissertation. Universität Hamburg. 164 pp. http://goo.gl/kWh8o accessible 2012-09-19.

Bohren and Albrecht (1998): Atmospheric thermodynamics. Oxford university press. New York. 402 pp. ISBN: 0-19-509904-4

Boris JP, Grinstein FF, Oran ES and Kolbe RL (1992): New insights into large eddy simulation. Fluid Dynamics Research. 10: 199–228. http://doi.org/frw9nt

Botnick AM and Fedorovich E (2008): Large eddy simulation of atmospheric convective boundary layer with realistic environmental forcings. In Meyers J, Geurts BJ and Sagaut P (eds.): "Quality and reliability of large-eddy simulations". Springer Netherlands. 193–204. http://doi.org/c85vjp

Boysen LR (2011): Beurteilung numerisch simulierter Grenzschichtprofile im Vergleich zu Profilen nach TA Luft. Bachelorarbeit. Universität Hamburg. 41 pp. http://goo.gl/kdqQK accessible 2012-11-19.

Breuer M (2002): Direkte numerische Simulation und Large-Eddy Simulation auf Hochleistungsrechnern. Shaker. Aachen. 431 pp. ISBN: 3-8265-9958-6

Brümmer B, Lange I and Konow H (2012): Atmospheric boundary layer measurements at the 280 m high Hamburg weather mast 1995–2011: mean annual and diurnal cycles. Meteorologische Zeitschrift. 21: 319–335. http://doi.org/sk3

Buschbom J, Gimmerthal S, Kirschner P, Michalczyk IM, Sebbenn AM, Schüler S, Schlünzen KH and Degen B (2012): Spatial composition of pollen-mediated gene flow in sessile oak. Forstarchiv. 83: 12–18. http://doi.org/nnv

Chechin DG, Lüpkes C, Repina IA and Gryanik VM (2013): Idealized dry quasi 2-D mesoscale simulations of cold-air outbreaks over the marginal sea ice zone with fine and coarse resolution. Journal of Geophysical Research: Atmospheres. 118: 1–27. http://dx.doi.org/10.1002/jgrd.50679

Chlond A (1998): Grobstruktursimulation – eine Methode zur Berechnung turbulenter atmosphärischer Strömungen. Habilitation. Universität Hamburg. Hamburg. 181 pp. http://goo.gl/yuYvC accessible 2012-02-18.

Chow FK, Weigel AP, Street RL, Rotach MW and Xue M (2006): High-resolution large-eddy simulations of flow in a steep alpine valley. Part I: Methodology, verification, and sensitivity experiments. Journal of Applied Meteorology and Climatology. 45: 63–86. http://doi.org/d2zt4d

Clarke RH (1970): Recommended methods for the treatment of the boundary layer in numerical models. Australian Meteorological Magazine. 18: 51–73. http://goo.gl/HNPTTF accessible 2013-12-03.

Claussen M (1991): Estimation of areally-averaged surface fluxes. Boundary-Layer Meteorology. 54: 387–410. http://dx.doi.org/10.1007/BF00118868

Cuxart J, Bougeault P and Redelsperger JL (2000): A turbulence scheme allowing for mesoscale and large-eddy simulations. Quarterly Journal of the Royal Meteorological Society. 126: 1–30. http://doi.org/ddj3zd

Deardorff JW (1972): Numerical investigation of neutral and unstable planetary boundary layers. Journal Atmospheric Science. 29: 91–115. http://doi.org/dbxmvk

Deardorff JW (1978): Efficient prediction of ground surface temperature and moisture, with inclusion of a layer of vegetation. Journal of Geophysical Research 83: 1889–1903. http://dx.doi.org/10.1029/JC083iC04p01889

Deardorff JW (1980): Stratocumulus-capped mixed layers derived from a three-dimensional model. Boundary-Layer Meteorology. 18: 495–527. http://doi.org/dtgccs

D'Errico J (2014): Moving window standard deviation. MATLAB CENTRAL File Exchange. http://goo.gl/dkfdFC accessible 2014-08-07.

Detering HW (1985): Mischungsweg und turbulenter Diffusionskoeffizient in atmosphärischen Simulationsmodellen. Berichte des Instituts für Meteorologie und Klimatologie der Universität Hannover. 25: 211 pp. ISBN: 3-923624-03-4

Dierer S (1997): Evaluierung des mesoskaligen Transport- und Strömungsmodells METRAS. Diplomarbeit. Universität Hamburg. 120 pp.

Dierer S, Schlünzen KH, Birnbaum G, Brümmer B and Müller G (2005): Atmosphere-sea ice interactions during a cyclone passage investigated by using model simulations and measurements. Monthly Weather Review. 133: 3678–3692. http://dx.doi.org/10.1175%2FMWR3076.1

Dyer AJ (1974): A review of flux-profile relationships. Boundary-Layer Meteorology. 7: 363–372. http://dx.doi.org/10.1007/bf00240838

EEA – European Environment Agency (2000): Corine land cover 2000. http://goo.gl/QpX84 accessible 20012-02-18.

Eichhorn J (1989): Entwicklung und Anwendung eines dreidimensionalen mikroskaligen Stadtklima-Modells. Dissertation. Johannes Gutenberg-Universität Mainz. 145 pp. http://goo.gl/WCb6j accessible 2012-11-09.

ESRI – Environmental Systems Research Institute (1998): ESRI shapefile technical description. 28 pp. http://goo.gl/NpcXta accessible 2013-10-20.

Farr TG, Rosen PA, Caro E, Crippen R, Duren R, Hensley S, Kobrick M, Paller M, Rodriguez E, Roth L, Seal D, Shaffer S, Shimada J, Umland J, Werner M, Oskin M, Burbank D and Alsdorf D (2007): The shuttle radar topography mission. Reviews of Geophysics. 45. RG2004. 33 pp. http://doi.org/dct747

Fedorovich E and Conzemius R (2002): Effects of initial temperature and velocity perturbations on the development of convection in the atmospheric boundary layer. 15th AMS Symposium on Boundary Layer and Turbulence. Wageningen. 39–42. http://goo.gl/9s4lB accessible 2012-11-11.

Fedorovich E, Conzemius R, Esau I, Chow FK, Lewellen D, Moeng C-H, Sullivan P, Pino D and de Arellan JV-G (2004): Entrainment into sheared convective boundary layers as predicted by different large eddy simulation codes. 16th Symposium on Boundary Layers and Turbulence. American Meteorological Society. Portland, Maine, USA. http://goo.gl/b7VEm accessible 2012-11-19.

Fischer M (2014): Idealisierte Modelluntersuchungen zum Einfluss von Stadtgröße auf die Niederschlagsbildung über der Stadt. Masterarbeit. Universität Hamburg.

Fischer R (2011): Entwicklung eines problemorientierten Software-Pakets zur automatisierten Aufbereitung, Analyse und Dokumentation von im Windkanal produzierten Daten zur LES-Validierung. Dissertation. Universität Hamburg. 199 pp. http://goo.gl/rwm8rA accessible 2014-06-24.

Flagg DD, Grawe D and Schlünzen KH (2014a): Impact of a 2 K warming scenario on the urban heat island of Hamburg. In preparation for publication.

Flagg DD, Schoetter R, Fock BH, Grawe D and Schlünzen KH (2014b): From land-use to surface cover for mesoscale atmospheric models. In preparation for publication.

Fock BH (2007): METRAS als Grobstruktursimulationsmodell. Diplomarbeit. Universität Hamburg. 89 pp. http://goo.gl/jSDBW accessible 2012-02-18.

Fock BH (2008): Kurzeinführung in einfache Spektralanalyse mittels der Fouriertransformation. Teaching material. 6 pp. http://goo.gl/94CcOh available on request 2013-12-01.

Fock BH (2012): MeMi-Toolbox – MATLAB tools for the multiscale model System M-SYS. Software package. http://goo.gl/pzBLF available on request 2012-02-18.

Fock BH (2014): Hamburg system for mesoscale sea ice forecasting for ship routing. Technical documentation. CEN. University of Hamburg. 24 pp.

Fock BH and Gierisch AMU (2014): MeMi coding rules for MATLAB - Write clean M-SYS post/preprocessors and readable analysis scripts in MATLAB. MeMi-Technical Report 6. University of Hamburg. 16 pp. http://goo.gl/rsW8ZB accessible 2014-06-17.

Fock BH, Kalb-Rottmann P and Schlünzen KH (2008): Evaluation of the micro-scale model MITRAS. 8th Annual Meeting of the EMS / 7th ECAC. Amsterdam.

Fock BH and Schlünzen KH (2012): Characterization of typical coastal circulations with high-resolution measurements in the Gulf of Valencia. International Journal of Climatology. 32: 1392–1405. http://doi.org/dn6shp

Franke J, Sturm M and Kalmbach C (2012): Validation of OpenFOAM 1.6.x with the German VDI guideline for obstacle resolving micro-scale models. Journal of Wind Engineering and Industrial Aerodynamics. 104–106: 350–359. http://doi.org/smz

Fröhlich J (2006): Large Eddy Simulation turbulenter Strömungen. Teubner. Wiesbaden. 414 pp. ISBN: 978-3-8351-0104-3. http://doi.org/fb237p

Funk D, Groß G and Trute P (2012): Stadtklimatische Bestandsaufnahme und Bewertung für das Landschaftsprogramm Hamburg Klimaanalyse und Klimawandelszenario 2050. Expert report GEO-NET Umweltconsulting GmbH in behalf

of Behörde für Stadtentwicklung und Umwelt (Freie und Hansestadt Hamburg). 70 pp. http://goo.gl/OZxtT accessible 2012-08-20.

Gal-Chen T and Somerville RCJ (1975): On the use of a coordinate transformation for the solution of the Navier-Stokes equations. Journal of Computational Physics. 17: 209–228. http://dx.doi.org/10.1016/0021-9991(75)90037-6

Germano M, Piomelli U, Moin P and Cabot WH (1991): A dynamic subgrid-scale eddy viscosity model. Physics of Fluids A: Fluid Dynamics. 3: 1760–1765. http://dx.doi.org/10.1063/1.857955

Gierisch A (2011): Mikroskalige Modellierung meteorologischer und anthropogener Einflüsse auf die Wärmeabgabe eines Gebäudes. Diplomarbeit. Universität Hamburg. 82 pp. http://goo.gl/kHTwR accessible 2012-05-20.

Gierisch A (2014): Development and evaluation of a short-range sea ice forecast model. Dissertation. Universität Hamburg. In preparation.

Gierisch A, Fock BH, Beitsch A, Bröhan D, Dobrynin M, Kaleschke L, Pohlmann T and Schlünzen KH (2013): Time scale analysis of sea ice processes and its application to the shortrange sea ice forecasting model system HAMMER. IICWG 5th International Workshop on Sea Ice Modelling and Data Assimilation, Bremen, Germany. 2013-05-15/16.

Golaz J-C, Wang S, Doyle J and Schmidt J (2005): Coamps®-Les: Model evaluation and analysis of second-and third-moment vertical velocity budgets. Boundary-Layer Meteorology. 116(3): 487–517. http://doi.org/cttgj9

Golding BW, Ballard SP, Mylne K, Roberts N, Saulter A, Wilson C, Agnew P, Davis LS, Trice J, Jones C, Simonin D, Li Z, Pierce C, Bennett A, Weeks M and Moseley S (2014): Forecasting Capabilities for the London 2012 Olympics. Bulletin of the American Meteorological Society. 95: 883–896. http://doi.org/wzg

Grawe D, Thompson HL, Salmond JA, Cai X-M and Schlünzen KH (2013): Modelling the impact of urbanisation on regional climate in the greater London area. International Journal of Climatology. 33: 2388–2401. http://doi.org/jqq

Grimmond CSB, Roth M, Oke TR, Au YC, Best M, Betts R, Carmichael G, Cleugh H, Dabberdt W, Emanuel R, Freitas E, Fortuniak K, Hanna S, Klein P, Kalkstein LS, Liu CH, Nickson A, Pearlmutter D, Sailor D and Voogt J (2010): Climate and more sustainable cities: Climate information for improved planning and management of cities (producers/capabilities perspective). Procedia Environmental Sciences. 1: 247–274. http://doi.org/c3spj6

Gross G (2010): Numerical simulations to the diurnal variation of wakes behind wind turbines. Meteorologische Zeitschrift 19: 91–99. http://doi.org/fkpjs3

Gross G (2012): Effects of different vegetation on temperature in an urban building environment. Micro-scale numerical experiments. Meteorologische Zeitschrift. 21: 399–412. http://dx.doi.org/10.1127/0941-2948/2012/0363

Harten A, Engquist B, Osher S and Chakravarthy SR (1987): Uniformly high order accurate essentially non-oscillatory schemes, III. Journal of Computational Physics. 71: 231–303. http://dx.doi.org/10.1016/0021-9991(87)90031-3

Hattori Y, Tanaka N, Moeng C-H, Suto H, Ishihara S, Eguchi Y, Hirakuhi H and Sugimoto S (2011): Numerical Simulation of Atmospheric Turbulence for Assessment of Wind Turbine. Journal of Fluid Science and Technology. 6: 342–356. http://dx.doi.org/10.1299/jfst.6.342

Heinze R (2013): Large-Eddy Simulation von bewölkten Grenzschichten zur Untersuchung von Bilanzen der statistischen Momente zweiter Ordnung und zur Überprüfung von Turbulenzmodellen. Dissertation. Gottfried Wilhelm Leibniz Universität Hannover. 153 pp. http://goo.gl/xzoQTK accessible 2014-07-23.

Hertwig D (2013): On Aspects of Large-Eddy Simulation Validation for Near-Surface Atmospheric Flows. Dissertation. Universität Hamburg. 333 pp. http://goo.gl/iGqiIx accessible 2014-05-01.

Hess GD, Hicks BB and Yamada T (1981): The impact of the Wangara experiment. Boundary-Layer Meteorology. 20: 135–174. http://doi.org/dgpc8z

Heus T, van Heerwaarden CC, Jonker HJJ, Siebesma PA, Axelsen S, van den Dries K, Geoffroy O, Moene AF, Pino D, de Roode SR and Vilà-Guerau de Arellano J (2010): Formulation of the Dutch atmospheric large-eddy simulation (DALES) and overview of its applications. Geoscientific Model Development. 3: 415–444. http://dx.doi.org/10.5194/gmd-3-415-2010

Hoffmann P (2009): Modifikation von Starkniederschlägen durch urbane Gebiete. Diplomarbeit. Universität Hamburg. 111 pp. http://goo.gl/I1sxH accessible 2012-12-09.

Hoffmann P (2012): Quantifying the influence of climate change on the urban heat island of Hamburg using different downscaling methods. Dissertation. Universität Hamburg. 130 pp. http://goo.gl/Tp9Bc accessible 2012-11-19.

Jochmann P, Reimer N, Kaleschke L, Müller G, Fock BH, Kauker F, Asseng J and Holfort J (2014): Ice Routing Optimization IRO-2 Validation Trial. HSVANewswave 2014/1: 2–5. http://goo.gl/Tj1BeY accessible 2014-06-19.

Kessler E (1995): On the continuity and distribution of water substance in atmospheric circulations. Atmospheric Research. 38: 109–145. http://doi.org/fj6pqd

Kirschner P (2009): GIS land use data for the metropolitan region of Hamburg and corresponding meta data. Personal communication.

Kolmogorov AN (1941): The local structure of turbulence in incompressible viscous fluid for very large Reynolds numbers. Doklady Akademii Nauk SSSR. 30. 299-303. Reprint in Proceedings of the Royal Society of London (1991): Series A Mathematical and Physical Sciences. 434: 9–13. http://doi.org/cnwvwv

Kraus H (2008): Grundlagen der Grenzschicht-Meteorologie: Einführung in die Physik der Atmosphärischen Grenzschicht und in die Mikrometeorologie. Springer. Berlin. 211 pp. ISBN: 3-540-75980-8

Kristóf G, Rácz N and Balogh M (2009): Adaptation of pressure based CFD solvers for mesoscale atmospheric problems. Boundary-Layer Meteorology. 131: 85–103. http://dx.doi.org/10.1007/s10546-008-9325-7

Landsberg HE (1981): The urban climate. International Geophysics Series. (28). Academic Press. New York. 275 pp. ISBN: 978-0124359604

Lenderink G and Holtslag AAM (2004): An updated length-scale formulation for turbulent mixing in clear and cloudy boundary layers. Quarterly Journal of the Royal Meteorological. 130: 3405–3427. http://dx.doi.org/10.1256/qj.03.117

Lengfeld K (2012): Assessing Near Surface Variability with a Wireless Sensor Network on the Small Scale. Dissertation. Universität Hamburg. 131 pp. http://goo.gl/LBRcYe accessible 2014-05-11.

LeMone MA (2003): Convective boundary layer. In Holton JR, Curry JA and John A (eds.): "Encyclopedia of Atmospheric Sciences". Academic Press. Amsterdam. 244–253. Gale Virtual Reference Library. http://goo.gl/bSqHk accessible 2012-02-18.

Leonard A (1974): Energy cascade in large-eddy simulations of turbulent fluid flows. Advances in Geophysics. 18 (A): 237–248. http://doi.org/bd35pt

Letzel MO (2007): High resolution large-eddy simulation of turbulent flow around buildings. Dissertation. Gottfried Wilhelm Leibniz Universität Hannover. 108 pp. http://goo.gl/YcjYg6 accessible 2014-07-22.

Letzel MO, Helmke CM, Ng E, An X and Raasch S (2012): LES case study on pedestrian level ventilation in two neighbourhoods in Hong Kong. Meteorologische Zeitschrift. 21: 575–589. http://doi.org/nnt

Lilly D (1966): The representation of small-scale turbulence in numerical simulation experiments. http://goo.gl/7kBWt accessible 2012-11-23.

Lilly DK and Klemp JB (1979): The effects of terrain shape on nonlinear hydrostatic mountain waves. Journal of Fluid Mechanics. 95: 241–261. http://doi.org/b924tw

Linde M (2011): Modellierung des Einflusses von Windkraftanlagen auf das umgebende Windfeld. Diplomarbeit. Universität Hamburg. 93 pp. http://goo.gl/HE3Bb accessible 2012-02-18.

Linde M, Hoffmann P, Lenhart H-J, Schlünzen KH and Schoetter R (2014): Influence of large offshore wind farms on North German climate. In review at Meteorologische Zeitschrift.

Lopez SD (2002): Numerische Modellierung turbulenter Umströmungen von Gebäuden. Dissertation. Universität Bremen. 93 pp. http://goo.gl/dZtSyN accessible 2013-08-13.

Lüpkes C, Gryanik VM, Witha B, Gryschka M, Raasch S and Gollnik T (2008): Modeling convection over arctic leads with LES and a non-eddy-resolving microscale model. Journal of Geophysical Research. 113. http://doi.org/dmqg8g

Lüpkes C and Schlünzen KH (1996): Modelling the arctic convective boundary-layer with different turbulence parameterizations. Boundary-Layer Meteorology. 79: 107–130. http://dx.doi.org/10.1007/bf00120077

Mailhot J, Milbrandt J, Giguère A, McTaggart-Cowan R, Erfani A, Denis B, Glazer A and Vallée M (2012): An experimental high-resolution forecast system during the Vancouver 2010 winter Olympic and Paralympic games. Pure and Applied Geophysics. 1–21. http://dx.doi.org/10.1007/s00024-012-0520-6

Martilli A, Clappier A and Rotach MW (2002): An urban surface exchange parameterisation for mesoscale models. Boundary-Layer Meteorology. 104: 261–304. http://dx.doi.org/10.1023/A:1016099921195

MathWorks (2011): Fast Fourier transform (FFT). MATLAB R2011a Documentation. http://goo.gl/5b38h accessible 2012-02-18.

MathWorks (2013): Smooth response data. Curve Fitting Toolbox. MATLAB R2013a Documentation http://goo.gl/GX2HG4 accessible 2014-08-07.

Mesinger F and Arakawa A (1976): Numerical methods used in atmospheric models. GARP Publication Series No. 17. WMO/ICSU Joint Organizing Committee. 64 pp. http://goo.gl/FIS4g accessible 2012-12-04.

Meyer EMI and Schlünzen KH (2011): The influence of emission changes on ozone concentrations and nitrogen deposition into the southern North Sea. Meteorologische Zeitschrift 20: 75–84. http://doi.org/dsf3nx

Moeng C-H, Dudhia J, Klemp J and Sullivan P (2007): Examining two-way grid nesting for large eddy simulation of the PBL using the WRF model. Monthly Weather Review. 135: 2295–2311. http://dx.doi.org/10.1175/MWR3406.1

Monin AS and Obukhov AM (1954): Basic laws of turbulent mixing in the surface layer of the atmosphere. Tr. Akad. Nauk SSSR Geophiz. Inst. 24. (151). 163–187. In KG McNaughton (ed.) (2008). http://goo.gl/m10zJ accessible 2012-02-18.

Müller F, Schlünzen KH and Schatzmann M (2000): Test of two numerical solvers for chemical reaction mechanisms in a 3D-air quality model. Environmental Modelling & Software. 15: 639–646. http://doi.org/fwdzj4

Niemeier U and Schlünzen KH (1993): Modelling steep terrain influences on flow patterns at the Isle of Helgoland. Beiträge zur Physik der Atmosphäre. 66: 45–62. http://goo.gl/JXqKft accessible 2014-08-08.

Panskus H (2000): Konzept zur Evaluation hindernisauflösender mikroskaliger Modelle und seine Anwendung auf das Modell MITRAS. Dissertation. Universität Hamburg. 108 pp. ISBN: 3-18-338907-X

Patton GE, Sullivan PP and Moeng C-H (2005): The influence of idealized heterogeneity on wet and dry planetary boundary layers coupled to the land surface. Journal of the Atmospheric Sciences. 62. (7). 2078–2097. http://doi.org/crjv2b

Peters K (2005): Wie Krokodile Vertrauen schaffen. Die neue Selbständigkeit im Unternehmen: Arbeiten ohne Ende? In Lorenz F and Schneider G (eds): Vertrauensarbeitszeit – Arbeitszeitkonten – Flexi-Modelle. Konzepte und betriebliche Praxis. VSA. Hamburg. 63–76. ISBN 3-89965-108-1. http://goo.gl/DUXxaV accessible 2014-07-27.

Petrik R (2012): Physical validation and bracket-based dynamical cores for mesoscale NWP models. Dissertation. Universität Hamburg. 161 pp. http://goo.gl/TJsDzF accessible 2014-07-14

Petrik R, Grawe D, Bungert U and Schlünzen KH (2014): Quantifying the impact of anthropogenic heat on the urban climate of Hamburg in the summer season. Article in preparation.

Philipp A (2013): Erweiterung von METRAS-LES für Scherströmungen. Masterarbeit. Universität Hamburg. 107 pp.

Piacsek SA and Williams GP (1970): Conservation properties of convection difference schemes. Journal of Computational Physics. 6: 392–405. http://dx.doi.org/10.1016/0021-9991(70)90038-0

Pielke RA, Cotton WR, Walko RL, Tremback CJ, Lyons WA, Grasso LD, Nicholls ME, Moran MD, Wesley DA, Lee TJ and Copeland JH (1992): A comprehensive meteorological modeling system – RAMS. Meteorology and Atmospheric Physics. 49: 69–91. http://dx.doi.org/10.1007/BF01025401

Pielke RA (2003): Land–Sea Breeze. In Holton JR, Curry JA and John A (eds.): "Encyclopedia of Atmospheric Sciences". Academic Press. Amsterdam. 1136–1140. Gale Virtual Reference Library. http://goo.gl/XG0yDH accessible 2014-07-01.

Pielke RA (2013): Mesoscale meteorological modeling. Academic press. Amsterdam. 726 pp. ISBN: 978-0-12-385237-3

Porté-Agel F, Meneveau C and Parlange MB (2000): A scale-dependent dynamic model for large-eddy simulation: application to a neutral atmospheric boundary layer. Journal of Fluid Mechanics. 415: 261–284. http://doi.org/cjbgm5

Orlanski I (1975): A rational subdivision of scales for atmospheric processes. Bulletin of the American Meteorological Society. 56: 527–530. http://goo.gl/yqCmI accessible 2012-11-23

Quante M (2010): Spectral behaviour of modelled wind time series and a comparison to respective windprofiler observations. In Schlünzen KH and Fock BH (eds.): "Model applications and model evaluation. Results of COST 728 workshop at ZMAW". University of Hamburg. Germany. 2008-05-15/16.

Raasch S (1988): Numerische Simulation zur Entwicklung von Wirbelrollen und konvektiver Grenzschicht bei Kaltluftausbrüchen über dem Meer. Berichte des Instituts für Meteorologie und Klimatologie der Universität Hannover. 23: 157 pp. ISBN: 3-923624-10-7

Raasch S and Etling D (1991): Numerical simulation of rotating turbulent thermal convection. Beiträge zur Physik der Atmosphäre. 64: 185–199.

Raasch S and Schröter M (2001): PALM - A large-eddy simulation model performing on massively parallel computers. Meteorologische Zeitschrift. 10: 363–372. http://dx.doi.org/10.1127/0941-2948/2001/0010-0363

Raasch S (2010): An introduction to large eddy simulation and the parallelized LES model PALM. NORCOWE summer school. Hardingasete. Norway. 2010-08-22/27. personal comunication.

Rechid D, Petersen J, Schoetter R and Jacob D (2014): Klimaprojektionen für die Metropolregion Hamburg Berichte aus den KLIMZUG-NORD Modellgebieten, Band 1. 60 pp. http://goo.gl/UvHfD9 accessible 2014-05-12.

Roedel W (2000): Physik unserer Umwelt – Die Atmosphäre. Springer. Berlin. 498 pp. ISBN: 3-540-67180-3

Rosenhagen G, Schatzmann M and Schrön A (2011): Das Klima der Metropolregion auf Grundlage meteorologischer Messungen und Beobachtungen. Klimabericht für die Metropolregion Hamburg. 19–59. http://doi.org/c8x9m5

Rouson D, Xia J and Xu X (2011): Scientific software design. The object-oriented way. Cambridge University Press. New York. 382 pp. ISBN: 978-0521-88813-4

Ryu Y-H and Baik J-J (2013): Daytime local circulations and their interactions in the Seoul metropolitan area. Journal of Applied Meteorology and Climatology. 52: 784–801. http://dx.doi.org/10.1175/JAMC-D-12-0157.1

Saad Y (2003): Iterative methods for sparse linear systems. Second Edition. SIAM. 244–247. http://goo.gl/iJ5w3Z accessible 2014-07-28.

Salim M, Schlünzen KH and Grawe D (2013): Impacts of proposed buildings on the local wind environment. 13th Annual Meeting of the EMS. Reading. United Kingdom. 2013-09-13.

Salim M, Grawe D and Schlünzen KH (2014): The Microscale Obstacle Resolving Meteorological Model MITRAS: Model Theory. Article in preparation.

von Salzen K, Claussen M and Schlünzen KH (1996): Application of the concept of blending height to the calculation of surface fluxes in a mesoscale model. Meteorologische Zeitschrift. 5: 60–66. http://goo.gl/eX2zaW conditional accessible 2013-12-03.

Schlünzen KH (1988): Das mesoskalige Transport- und Strömungsmodell 'METRAS' - Grundlagen, Validierung, Anwendung. Hamburger Geophyikalische Einzelschriften. A88. 139 pp.

Schlünzen KH (1990): Numerical studies on the inland penetration of sea breeze fronts at a coastline with tidally flooded mudflats. Beiträge zur Physik der Atmosphäre. 63: 243–256. http://goo.gl/KErJpS accessible 2014-08-18.

Schlünzen KH (1996): Validierung hochauflösender Regionalmodelle. Berichte aus dem Zentrum für Meeres- und Klimaforschung Reihe A: Meteorologie 23. 177 pp. http://goo.gl/pZdJX accessible 2012-10-12.

Schlünzen KH (1997): On the validation of high-resolution atmospheric mesoscale models. Journal of Wind Engineering and Industrial Aerodynamics. 67–68: 479–492 http://dx.doi.org/10.1016/S0167-6105(97)00095-0

Schlünzen KH, Bigalke K, Lüpkes C, Niemeier U and von Salzen K (1996a): Concept and realization of the mesoscale transport and fluid model 'METRAS'. Universität Hamburg. 131 pp. http://goo.gl/G4yNRM accessible 2014-07-16.

Schlünzen KH, Bigalke K, Lüpkes C, Niemeier U and von Salzen K (1996b): Hints for using the mesoscale model 'METRAS'. Meteorologisches Institut der Universität Hamburg. METRAS Technical Report 6. 80 pp. http://goo.gl/udg4s accessible 2012-11-11.

Schlünzen KH and Katzfey JJ (2003): Relevance of sub-grid-scale land-use effects for mesoscale models. Tellus A. 55: 232–246. http://doi.org/c3knkp

Schlünzen KH, Hinneburg D, Knoth O, Lambrecht M, Leitl B, López S, Lüpkes C, Panskus H, Renner E, Schatzmann M, Schoenemeyer T, Trepte S und Wolke R (2003): Flow and transport in the obstacle layer: First results of the micro-scale model MITRAS. Atmospheric Chemistry and Physics. 7: 113–130. http://doi.org/ds96tp

Schlünzen KH and Reinhardt V (2007): Quality assurance for MeMi models. MEMI Technical Report 2. 14 pp.

Schlünzen KH, Schröder G, Fock BH, Meschkat G, Augustin W and Heuveline V (2008): High resolution forecasts for the 2007 America's Cup and evaluation with buoy measurements. 8th Annual Meeting of the EMS / 7th ECAC. Amsterdam.

Schlünzen KH and Bigalke K (2010): METRAS-PCL Version 4.0 Benutzerhandbuch Version 2.0. Meteorologisches Institut der Universität Hamburg. Editing: Linde M and Fock BH. 54 pp.

Schlünzen KH, Hoffmann P, Rosenhagen G and Riecke W (2010): Long-term changes and regional differences in temperature and precipitation in the metropolitan area of Hamburg. International Journal of Climatology. 30: 1121–1136. http://dx.doi.org/10.1002/joc.1968

Schlünzen KH, Grawe D, Bohnenstengel SI, Schlüter I and Koppmann R (2011): Joint modelling of obstacle induced and mesoscale changes - current limits and challenges. Journal of Wind Engineering and Industrial Aerodynamics. 99: 217–225. http://dx.doi.org/10.1016/j.jweia.2011.01.009

Schlünzen KH, Flagg DD, Fock BH, Gierisch A, Lüpkes C, Reinhardt V and Spensberger C (2012a): Scientific documentation of the multiscale model system M-SYS (METRAS, MITRAS, MECTM, MICTM, MESIM). MEMI Technical Report 4. Meteorologisches Institut KlimaCampus Universität Hamburg. 138 p. http://goo.gl/9WWFf accessible 2012-02-18.

Schlünzen KH, Bungert U, Flagg DD, Fock BH, Gierisch A, Grawe D, Kirschner P, Lüpkes C, Reinhardt V, Ries H, Schoetter R, Spensberger C and Uphoff M (2012b): Technical documentation of the multiscale model system M-SYS (METRAS, MITRAS, MECTM, MICTM, MESIM). MEMI Technical Report 3. Meteorologisches Institut KlimaCampus Universität Hamburg. 117 p. http://goo.gl/1gZUM accessible 2012-02-18.

Schlünzen KH, Schoetter R, Linde M, Hoffmann P (2014): Stadtklima. In KLIMZUG-NORD Verbund: Kursbuch Klimaanpassung. Handlungsoptionen für die Metropolregion Hamburg. 32–33. ISBN: 978-3-941492-66-0 http://goo.gl/y4z2lg accessible 2014-11-15.

Schmittner A (1996): Parametrisierung subskaliger Flüsse in einem mesoskaligen Modell der arktischen atmospärischen Grenzschicht. Diplomarbeit. Universität Bremen. 15–21/62–70.

Schoetter R (2010): Einflüsse von Quellkonfiguration und Modelleigenschaften auf simulierte Konzentrationsfelder. Diplomarbeit. Universität Hamburg. 116 pp. http://goo.gl/5g3zF accessible 2013-01-10.

Schoetter R (2013): Can local adaptation measures compensate for regional climate change in Hamburg Metropolitan Region. Dissertation. Universität Hamburg. 168 pp. http://goo.gl/8tiLvD accessible 2013-08-26.

Schoetter R, Grawe D, Hoffmann P, Kirschner P, Gratz A and Schlunzen KH (2013): Impact of local adaptation measures and regional climate change on perceived temperature. Meteorologische Zeitschrift. 22: 117–130. http://doi.org/smd

Schröder G (2007a): Development and test of a multiple grids option in a mesoscale model. Dissertation. Universität Hamburg. 166 pp. http://goo.gl/S4gRd accessible 2012-02-18.

Schröder G (2007b): GrADS for METRAS - a script based plotting system METRAS. Technical Report. 27 pp. http://goo.gl/MQgsQ4 available on request 2014-06-26.

Schroeder G, Schlünzen KH and Schimmel F (2006): Use of (weighted) essentially non-oscillatory advection schemes in a mesoscale model. Quarterly Journal of the Royal Meteorological Society. 132: 1509–1526. http://doi.org/d6gcqk

Schroeder G and Schlünzen HK (2009): Numerical dispersion of gravity waves. Monthly Weather Review. 137: 4344–4354. http://doi.org/ftvj3v

Schueler S and Schlünzen KH (2006): Modeling of oak pollen dispersal on the landscape level with a mesoscale atmospheric model. Environmental Modeling and Assessment. 11: 179–194. http://dx.doi.org/10.1007/s10666-006-9044-8

Schultze M (2013): Weiterentwicklung von MITRAS zu einem wirbelauflösenden Stadttausschnittsmodell. Masterarbeit. Universität Hamburg. 75 pp. http://goo.gl/1FZOuh accessible 2014-07-19.

Schumann U (1975): Subgrid scale model for finite difference simulations of turbulent flows in plane channels and annuli. Journal of Computational Physics. 18: 376–404. http://dx.doi.org/10.1016/0021-9991(75)90093-5

Schumann U and Sweet RA (1988): Fast Fourier transforms for direct solution of poisson's equation with staggered boundary conditions. Journal of Computational Physics. 75: 123–137. http://dx.doi.org/10.1016/0021-9991(88)90102-7

Seity Y, Brousseau P, Malardel S, Hello G, Bénard P, Bouttier F, Lac C and Masson V (2010): The AROME-France convective-scale operational model. Monthly Weather Review. 139: 976–991. http://doi.org/bqg6gg

Shapiro R (1971): The use of linear filtering as a parameterization of atmospheric diffusion. Journal of the Atmospheric Sciences. 28: 523–531. http://doi.org/dmqfsh

Siano S (1997): Numerische Simulation zur Ausbreitung von Flugzeugemissionen durch Wirbelschleppen in geschichteten Scherströmungen. Berichte des Instituts für Meteorologie und Klimatologie der Universität Hannover. 54: 71 pp. ISBN: 3-923624-35-2

Skamarock WC (2004): Evaluating mesoscale NWP models using kinetic energy spectra. Monthly Weather Review. 132: 3019–3032. http://doi.org/d8x39x

Smagorinsky J (1963): General circulation experiments with the primitive equations. Monthly Weather Review. 91: 99–164. http://doi.org/bhd6ks

Spensberger C (2010): Albedoänderungen in der Arktis durch Rußemissionen von Schiffen und Flugzeugen. Diplomarbeit. Universität Hamburg. 94 pp. http://goo.gl/OtPLO accessible 2012-02-18.

Stadt Stuttgart (2010): Der Klimawandel – Herausforderung für die Stadtklimatologie. Schriftenreihe des Amtes für Umweltschutz - Heft 3/2010. 86 pp. http://goo.gl/g9SdP accessible 2012-02-18.

Stull RB (1988): An introduction to boundary layer meteorology. Kluwer Academic Publishers. Dordrecht. 666 pp. ISBN: 978-90-277-2768-8

Stull RB (2000): Meteorology for Scientists and Engineers. Brooks/Cole. Pacific Grove. 502 pp. ISBN: 0-534-37214-7

Sullivan PP, Moeng C-H, Stevens B, Lenschow DH and Mayor SD (1998): Structure of the entrainment zone capping the convective atmospheric boundary layer. Journal of the Atmospheric Sciences. 55: 3042–3064. http://doi.org/dpf7fd

Teichert N (2013): Analyse von Oberflächeneinflüssen auf die sommerlichen Temperaturen in der Metropolregion Hamburg unter Anwendung eines GIS. Diplomarbeit. Universität Hamburg. 113 pp.

Therry G and Lacarrère P (1983): Improving the Eddy Kinetic Energy model for planetary boundary layer description. Boundary-Layer Meteorology. 25: 63–88. http://dx.doi.org/10.1007/BF00122098

Thompson HL (2008): Modelling the impact of urbanisation on the regional climate of the greater London area. Dissertation. University of Birmingham. 263 p. http://goo.gl/ZBlJy accessible 2012-02-18.

Trukenmüller A, Grawe D and Schlünzen KH (2004): A model system for the assessment of ambient air quality conforming to EC directives. Meteorologische Zeitschrift. 13: 387–394. http://doi.org/c7jmdn

UNFPA - United Nations Population Fund (2011): The state of world population 2011. New York. 124 pp. ISBN: 978-0-89714-990-7 http://goo.gl/I1uHNA accessible 2013-12-03.

Uphoff M (2015): Wolkeneffekte in den Photolyseraten und Auflösungseffekte in Chemietransportmodellen. Dissertation. Universität Hamburg. In preparation.

VDI - Verein Deutscher Ingenieure (1997): Umweltmeteorologie - Klima- und Lufthygienekarten für Städte und Regionen. VDI 3787 Part 1. VDI/DIN-Handbuch Reinhaltung der Luft, Band 1b.

Wang W (2009): The influence of thermally-induced mesoscale circulations on turbulence statistics over an idealized urban area under a zero background wind. Boundary-Layer Meteorology. 131: 403–423. http://doi.org/bzj87j

Weisstein EW (2014): Nyquist Frequency. From MathWorld - A Wolfram Web Resource. http://goo.gl/aWRaZk accessible 2014-09-06.

Wiesner S (2013): Observing the impact of soils on local urban climate. Dissertation. Universität Hamburg. 175 pp. http://goo.gl/IC2MSx accessible 2014-05-11.

Williamson JH (1980): Low-storage Runge-Kutta schemes. Journal of Computational Physics. 35: 48–56. http://dx.doi.org/10.1016/0021-9991(80)90033-9

Wolfram|Alpha (2010): Estimate indefinite integral: 1/(ax+bx^(3/2)). Wolfram Alpha LLC. http://goo.gl/YYygV accessible 2012-02-18.

Wolfram|Alpha (2014): Sunrise and sunset 15 july Hamburg Germany. Wolfram Alpha LLC. http://goo.gl/GAFo6b accessible 2014-09-07.

WSV - Wasser- und Schifffahrtsverwaltung des Bundes (2014): Pegelonline: Stammdaten Messstellenname Hamurg St. Pauli. http://goo.gl/E6JIMO accessible 2014-04-05.

Wyngaard JC and Brost RA (1984): Top-down and bottom-up diffusion of a scalar in the convective boundary layer. Journal of the Atmospheric Sciences. 41: 102–112. http://doi.org/dgtrck

Wyngaard JC (2010): Turbulence in the atmosphere. Cambridge University Press. Cambridge. 406 pp. ISBN: 978-0-521-88769-4

Yamada T and Koike K (2011): Downscaling mesoscale meteorological models for computational wind engineering applications. Journal of Wind Engineering and Industrial Aerodynamics. 99: 199–216. http://doi.org/bkkm7h

Acknowledgements

Eidesstattliche Versicherung

Hiermit erkläre ich an Eides statt, dass ich die vorliegende Dissertationsschrift selbst verfasst und keine anderen als die angegebenen Quellen und Hilfsmittel benutzt habe.

Hamburg, 2014-11-19   _____

(Björn Hendrik Fock)